



Annand, Kirsty June (2018) *The nanoscale mechanisms of zircaloy-4 corrosion in simulated nuclear reactor conditions*. PhD thesis.

<http://theses.gla.ac.uk/8781/>

Copyright and moral rights for this work are retained by the author

A copy can be downloaded for personal non-commercial research or study, without prior permission or charge

This work cannot be reproduced or quoted extensively from without first obtaining permission in writing from the author

The content must not be changed in any way or sold commercially in any format or medium without the formal permission of the author

When referring to this work, full bibliographic details including the author, title, awarding institution and date of the thesis must be given

Enlighten:Theses
<http://theses.gla.ac.uk/>
theses@gla.ac.uk

The Nanoscale Mechanisms of Zircaloy-4 Corrosion in Simulated Nuclear Reactor Conditions



University
of Glasgow

Kirsty June Annand BSc MSc

Submitted in fulfillment of the requirements for the Degree of
Doctor of Philosophy

School of Physics and Astronomy

College of Science and Engineering

University of Glasgow

© Kirsty June Annand, September 2017

A b s t r a c t

Worldwide, zirconium alloys have long been utilised for fuel cladding elements and other structural components within several commercial designs of nuclear reactor owing to their high creep resistance, superior corrosion resistance in highly aggressive environments, and low cross section for neutron absorption. The purpose of this cladding material is to separate the uranium dioxide (UO_2) fuel and the coolant water in order to prevent the escape of fission products, whilst also maintaining heat transfer to the coolant. Consequently, water corrosion of the fuel containments has become a key factor in the limitation of the lifetime of fuel rods within nuclear reactors, and maintaining containment integrity under corrosion is critical to ensuring safe operation and preventing accidental release of radionuclides into the cooling water. Therefore, developing an understanding of the mechanisms which govern the corrosion of zirconium-based alloys is vital, and is the motivation behind this study. The analysis of the corrosion of an unirradiated zirconium based alloy - Zircaloy-4 - is performed in a three-fold manner in this thesis. Firstly, an investigation of the metal:oxide interface is carried out, the results of which are set out in Chapter 4 of this thesis. Providing a clear understanding of the nanoscale structure and chemistry of this interface, alongside a thorough investigation of the morphology of any suboxide phases generated during the process of corrosion is fundamental to understanding the overall corrosion of this alloy. Secondly, systematic analysis of the corrosion and incorporation of SPPs into the oxide layer is performed in Chapter 5 of this thesis, in order to help inform the role of SPPs on the corrosion process for both autoclave, and more importantly, on irradiated oxides. In addition, spatially resolved chemical mapping, and correlation to the crystallographic structure provides an understanding not previously shown in the literature on the complex corrosion that takes place. Finally, Chapter 6 presents findings from studying oxygen content through the oxide scale, performed in order to quantitatively elucidate the details of the oxygen content from the outer porous oxide, through the stoichiometric ZrO_2 , and into any metastable suboxide layers present. This analysis highlights the significance of understanding such microstructural behaviour, in order to interpret the overall macro structural corrosion behaviour of zirconium alloys.

“THE ONE WITH THE END OF AN ERA”

Declaration

This thesis is a record of the work carried out by myself in the Materials and Condensed Matter group of the School of Physics and Astronomy at the University of Glasgow during the period 2013-2017, under the supervision of Dr. Ian MacLaren and Dr. Mhairi Gass. The work described herein is my own, except where explicit reference is made to the contribution of others.

Parts of this work have been published in peer-reviewed papers. These papers are:

- I. K. J. Annand, I. MacLaren, M. Gass, *Journal of Nuclear Materials*, 465 (2015) 390-399.
- II. Ian MacLaren, K. J. Annand, C. Black, A. J. Craven, *EELS at very high energy losses, Microscopy*, (2017) 1-8.
- III. K. J. Annand, M. Nord, I. MacLaren, M. Gass, *The Corrosion of Zr(Fe, Cr)₂ and Zr₂Fe Secondary Phase Particles in Zircaloy-4 under 350 °C pressurised water conditions, Corrosion Science*, 128 (2017) 213-223.

The University of Glasgow Thomson Experimental Prize for the best second year PhD report (March 2016) was won based on research presented in this thesis.

Oral and/or poster presentations have also been given at the following international conferences:

- I. Zirconium in the Nuclear Industry – South Carolina, USA - April 2016;
- II. Microscience Microscopy Congress – Manchester, UK – July 2015;
- III. International Microscopy Congress – Prague, CZ – September 2014;
- IV. Microscopy of Oxidation – Nottingham, UK – April 2014.

Kirsty June Annand
Glasgow, September 2017

Copyright © 2017.

“ The copyright of this thesis rests with the author. No quotations from it should be published without the author’s prior written consent and information derived from it should be acknowledged”.

Acknowledgements

I would like to extend my heartfelt thanks to those who so generously contributed to the work in this thesis; their steadfast support has propelled me through many challenging times, and without them I would not be writing this today.

First and foremost, thanks to my supervisor Dr Ian MacLaren; for having the faith in me to tackle this challenge, for imparting his knowledge on me so willingly and patiently, and for entrusting me to take hold of my own career and grow into an independent researcher. His belief in me has been unwavering throughout my time in academia, from my undergraduate degree to my position as a postdoctoral researcher, and for that I will be forever grateful.

Similar, profound gratitude goes to my second supervisor Dr Mhairi Gass, for her invaluable industrial advice, for providing me with an avenue to realise the real world importance of my research, and for making every microscope session a little easier with the provision of cake. Related thanks also to AMEC Foster Wheeler and the EPSRC for their financial support of this work.

I am also forever indebted to Dr Sam McFadzean, Colin How and Billy Smith, who helped me out of a sticky situation on many an occasion. The success of much of the incredible research produced by the MCMP group at Glasgow hinges on their invaluable advice, experience, and dedication to developing the next generation of microscopists. Their contribution to this work should not be underestimated, and working with them truly has been a pleasure.

A huge thank you also to Dr Donald MacLaren, for providing me with the most succinct, timely and ridiculously helpful feedback on the works contained in this thesis, as only he can. Thanks also to Dr Steven McVitie and Dr Damien McGrouther, for their support throughout the years, their words of reassurance, and making my viva not as utterly horrific as I had envisioned.

Also, thanks to Heather Lambie, for allowing me to continually explore my love of science communication. Throughout the years this has been crucial in getting me out of the office and keeping my research fresh and exciting. A similar appreciation goes to Prof. Susan Waldron for her kind words and support throughout my time at Glasgow.

To the rest of the MCMP group - thanks to all of you for keeping me sane throughout my time here, for your advice and conversations both technical and non-technical, and for letting me know what horrors I had in store for me.

Particular thanks go to Monifa. Your genuine happiness at any successes which have come my way goes to show what a kind hearted and generous friend you are. You have been the best office mate, roller buddy and pep talker anyone could ask for, and I hope our friendship extends beyond our time in 409.

Thank you to Rair, who (first impressions aside) has grown into a most cherished friend. Our mutual love of a good cuppa, Chinese food, and a Caipirinha or two over the years has given me some of my best memories (and I have the photos to prove it).

To Scott, thank you for showing me that it is possible to get to this point without losing sight of who you are. You are by far one of my closest confidants, my sassiest of dancing partners, and I am privileged to call you my friend.

Last, but by no means least, thank you to my family and friends outside of the office for your love and support. Thank you to my girls for the laughter and the tears over many cups of tea, and for being strong for me when I wasn't able to be for myself. Most importantly to Amy; our friendship has not only survived, but thrived, through one of the most difficult periods of our lives. I truly treasure our friendship, and I thank you for always being willing to drop anything to be by my side.

Thank you to my grandparents, who helped raise me, and made me the person I am today - Granny Margaret, Grandad William, Granny Chrissie and Grandad Eddie. You will always be precious to me and I hope I have made you proud.

A huge thank you also to Uncle Billy; for always appearing interested when I was babbling on about science, for our ridiculous chatter about whether rainbows really are there unless you look at them, and for joining me in my love of a good quiz.

To John, I find it difficult to put my gratitude for your undying love, support, and everlasting strength into words. Thank you for your listening ear, your ability to make the perfect cup of tea, and for always making me laugh. Without you, this would not have been possible, and I will be forever grateful for all that you have done for me.

Finally, to my Mum and Dad - June and George. With your steadfast belief that I would make it to this point, here we finally are. This achievement is a testament to your determination as much as it is to mine.

You are my whole world, my best friends, and I dedicate this thesis to you.

Abbreviations

ADF – Annular Dark Field

BF – Bright Field

Cold FEG – Cold Field Emission Gun

DF – Dark Field

DHC – Delayed Hydride Cracking

DualEELS – Dual Electron Energy Loss Spectroscopy

EDS – X-ray Spectroscopy

EELS – Electron Energy Loss spectroscopy

EFTEM SI - Energy Filtered Transmission Electron Microscope Spectrum Imaging

ELNES – Energy Loss Near Edge Structure

FIB – Focussed Ion Beam

HAADF – High Angle Annular Dark Field

LOCA - Loss of Coolant Accident

MLLS – Multiple Linear Least Squares

PCA Analysis – Principal Component Analysis

SADP – Selected Area Diffraction Pattern

SEM – Scanning Electron Microscopy

SPP – Secondary Phase Particle

STEM – Scanning Transmission Electron Microscopy

STEM SI – Scanning Transmission Electron Microscope Spectrum Imaging

TEM – Transmission Electron Microscopy

VLM – Visual Light Microscope

Contents

Abstract

Declaration

Abbreviations

1 Introduction

1.1 Thesis Structure	26
1.2 Literature Review: Oxidation of zirconium and its Alloys.....	28
1.2.2. Structure of the Literature Review	28
1.3 Zirconium for Nuclear Fuel Containment	30
1.4 Properties of Zirconium and its Alloys.....	33
1.5 Oxide Formation on zirconium	35
1.6 Oxide Microstructure	40
1.7 Suboxides.....	41
1.8 Secondary Phase Particles	45

2 Sample Preparation and Instrumentation

2.1 Oxidation Experiments by AMEC Foster Wheeler	50
2.2 Focussed Ion Beam (FIB).....	51
2.2.1 FIB Lift-Out Technique	53
2.2.2 Experimental FIB Conditions	53
2.3 Electrons for Imaging.....	56
2.3.1 Electron Matter Interactions	58
2.3.2 The Angle of Scattering	61
2.3.3 The Interaction Cross Section	62
2.3.4 The Error on the Cross Section	62
2.3.5 Mean Free Path for inelastic scattering	63
2.3.6 Plural and Multiple Scattering.....	64
2.4 The Transmission Electron Microscope (TEM)	65
2.4.1 The Emission Source	67
2.4.2 The Magnetic Lens	69
2.4.3 The Condenser System	70

2.4.4 Specimen	71
2.4.5 The Objective System	72
2.5 Imaging Methods in the TEM	74
2.5.1 Selected Area Diffraction (SAD)	74
2.5.2 Bright-Field Imaging.....	74
2.5.3 The Projector System	75
2.6 Imaging Solutions for Transmission Electron Microscopy	76
2.6.1 Charge-Coupled Device (CCD)	76
2.7 Improving the Transmission Electron Microscope	76
2.7.1 Spherical Aberration	78
2.7.2 Chromatic Aberration	78
2.7.3 Astigmatism	79
2.8 Scanning Transmission Electron Microscopy (STEM).....	80
2.8.1 STEM Bright Field.....	80
2.8.2 STEM Annular Dark Field and High Angle Annular Dark Field.....	80
2.9 The Energy Loss Spectrometer	81
2.10 Employing De-Scan in the STEM.....	82
3 Electron Energy Loss Spectroscopy (EELS)	
3.1 Why do EELS?	86
3.2 The Electron Energy Loss Spectrum	87
3.3 EEL Spectrometers.....	90
3.3.1 Gatan Imaging Filter (GIF) Layout	91
3.4 Dual Electron Energy Loss Spectroscopy (DualEELS)	92
3.5 Limits on EELS Spatial Resolution	94
3.6 EEL Data Processing	94
3.6.1 Basic Dual EELS Processing.....	95
3.6.2 Multiple Linear Least Squares (MLLS) Low Loss Fingerprinting	97
3.6.3 Core Loss Quantification.....	98
3.7 O:Zr Ratios.....	101
3.8 High Loss L2/L3 Investigations	102
4 The Metal:Oxide Interface	
4.1 Motivation	106

4.2 Experimental Detail.....	107
4.3 Post-Processing of Electron Energy Loss Spectroscopy Data	107
4.4 Results.....	108
4.4.1 Details of EELS spectra from the different phases.....	108
4.4.2 Low loss shapes.....	109
4.4.3 O Electron energy loss near edge structure (ELNES)	110
4.4.4 Zr L _{2,3} ELNES.....	111
4.4.5 Mapping of the interface through the corrosion process.....	112
4.5 Pre-Transition.....	113
4.6 At Transition.....	115
4.7 Post-Transition.....	117
4.8 Discussion.....	119
5 Secondary Phase Particles (SPPs)	
5.1 Motivation	128
5.2 Microscopy of SPPs	129
5.3 Results.....	130
5.3.1 Zr ₂ Fe SPP in metal	130
5.3.2 Zr ₂ Fe SPP in oxide.....	131
5.3.3 Zr(Fe, Cr) ₂ SPP in metal	134
5.3.4 Zr(Fe, Cr) ₂ SPP at metal-oxide interface (during oxidation)	135
5.3.5 Zr(Fe,Cr) ₂ SPP in oxide.....	141
5.4 Discussion	145
6 Oxygen Content through Oxide Thickness	
6.1 Microscopy of the Oxide Scale	150
6.2 Results.....	151
6.2.1 1.6 μm oxide layer specimen	152
6.2.2 4.7 μm oxide layer	155
6.2.3 2.78 μm specimen	157
6.3 Discussion.....	159
7 Conclusions and Outlook	
7.1 Conclusions.....	163
7.2 Outlook and Future Work	166

List of Tables

1.1:	<i>Standard chemical specifications for Zircaloy-4 and Zircaloy-2 in the nuclear industry [23]</i>	33
1.2:	<i>Common phases occurring in the zirconium alloys, amended from [7].....</i>	34
3.1:	<i>Details of elements and edges of interest, corresponding edge energy and details of the ideal signal extraction windows for three cases (metal:oxide interface, a Zr(Fe, Cr)₂ SPP and a Zr₂Fe SPP) where high loss quantification using the modelling approach was required</i>	100
4.1:	<i>Peak positions in the low loss for the Zr and the ZrO₂, compared with previous published values</i>	110
5.1:	<i>Chemical composition of a typical Zr₂Fe particle found in the metal as determined by EELS analysis.....</i>	130
5.2:	<i>Chemical composition of a typical oxidised Zr₂Fe particle as determined by EELS analysis.....</i>	133
5.3:	<i>Chemical composition of a typical unoxidised Zr(Fe, Cr)₂ particle as determined by EELS analysis</i>	135
5.4:	<i>Chemical composition of a typical oxidised Zr(Fe, Cr)₂ particle as determined by EELS analysis</i>	136

List of Figures

1.1:	<i>An illustration of the arrangement of a typical pressurised water reactor fuel assembly. Each fuel rod in the fuel assembly contains sintered pellets of low-enriched uranium within α-zirconium-lined cladding. They are brought together in fuel assemblies where arrays of control rods are held in place by tie plates and spacers. Adapted from [7].</i>	31
1.2:	<i>Pictorial explanation of power transfer in a pressurised water reactor. The primary coolant is in orange and the secondary coolant (steam and later feed water) is in blue (adapted from [22]).</i>	32
1.3:	<i>Ellingham diagram of Zr-O system, from [2].</i>	36
1.4:	<i>Typical oxidation kinetics of a generic zirconium-based alloy. After the pre-transition region where the oxidation kinetics follow a square/cubic relationship, depending upon the oxidising environment, the protective layer breaks down and cyclic oxidation proceeds with an overall linear rate. The critical thickness before transition occurs is usually of the order of $\sim 2 \mu\text{m}$.</i>	36
1.5:	<i>A low magnification dark field electron micrograph of a Zircaloy-4 sample with $\sim 6 \mu\text{m}$ oxide on the surface, showing a) oxide b) first transition cracking c) second transition cracking d) hydrides, e) a large scale undulating metal:oxide interface and f) the metal matrix. The bright region on the left is simply platinum deposited in order to attach the sample to the holder. This image also shows the bright layer of sputter coated gold at the surface used to protect the sample from ion beam damage. Curtaining caused by thinning during sample preparation can also be seen below cracks.</i>	38
1.6:	<i>Equilibrium phase diagram for the Zr-O system, after N. Selmi et al. [3]</i>	42
2.1:	<i>Processing history of the reference Zr-4 sheet material.</i>	51
2.2:	<i>A schematic of the FIB system showing the Ion and Electron columns and the specimen inside the vacuum chamber.</i>	52
2.3:	<i>Schematic of a typical section of a coupon showing from top down, the oxide layer built up on the surface of the metal, the suboxide or oxygen rich layers, and finally the base metal at the bottom.</i>	54
2.4:	<i>The TEM lift-out procedure where a) platinum is deposited over the region of interest, b) cuts are made to the front, back and one side of the section, c) the section is tilted and cuts made on all but part of one side, d) the final thinned specimen attached to a TEM Omniprobe™ lift-out grid, ready for S/TEM analysis</i>	55
2.5:	<i>Schematic of the interaction between a thin specimen and an incident electron beam.</i>	58

2.6:	<i>A particle view of electron scattering. a) Elastic scattering is caused by Coulomb attraction by the nucleus. Coulomb repulsion causes inelastic scattering in b) Inner- and c) Outer-shell electrons, which are excited to a higher energy level</i>	60
2.7:	<i>Schematic illustration of an energy-loss spectrum and examples of how main energy loss peaks are created.....</i>	61
2.8:	<i>Electron scattering from a single atom. Electrons are scattered through an angle of θ. The total solid angle of scattering is Ω. A small increase in scattering angle $d\theta$ results in a small increase in solid angle $d\Omega$. Adapted from [4]</i>	62
2.9:	<i>a) Top down schematic of a Transmission Electron Microscope (TEM) showing the condenser, objective and projector system, and the path in which electrons take from the gun to the viewing screen and b) Schematic of a scanning transmission electron microscope (STEM) indicating the path electrons take through the column, and into the magnetic prism for EELS analysis.</i>	66
2.10:	<i>Schematic of a thermionic electron emission gun [5].....</i>	67
2.11:	<i>Schematic of a cold FEG electron emission gun, where i_E is the incident electron beam.</i>	69
2.12:	<i>The condenser system in a Transmission Electron Microscope.....</i>	70
2.13:	<i>The two basic operations of the TEM imaging system where a) diffraction mode: the DP is projected onto the viewing screen and b) imaging mode: where the image is projected onto the screen.....</i>	73
2.14:	<i>Bright field (a) ray diagram, with (b) objective aperture accepting direct beam for bright field imaging. Adapted from [94].</i>	75
2.15:	<i>Spherical aberration in a lens showing how paraxial rays are refracted less than non-paraxial rays, resulting in multiple focal points.....</i>	78
2.16:	<i>Chromatic aberration resulting in electrons with a range of energies being focussed in different planes (adapted from [5]).....</i>	79
2.17:	<i>The EELS spectrometer, showing how the incoming electrons are deflected according to their energies, resulting in an Electron Energy Loss Spectrum. Adapted from [7].....</i>	82
2.18:	<i>De-scan compensates for the movement of the beam on the specimen during STEM mode, allowing the image of the beam to remain stationary below the image deflection coils and thus in the differential pumping aperture and on the EELS detector</i>	83
3.1:	<i>Definition of α and β in a (S)TEM showing α, the convergence semi-angle and β, the collection semi-angle.....</i>	86

3.2:	<i>Electron energy loss spectrum of a Zircaloy-4 specimen corroded under high pressure, at 350 °C, showing low-loss profiles of phases present in the specimen, alongside a scaled profile of the high-loss ionisation edges.....</i>	87
3.3:	<i>A spectrum image data cube. In STEM spectrum imaging, the STEM probe is systematically moved along the sample in x and y directions, and the resulting signals are collected. The entire spectrum is stored at each point allowing advanced spectral processing to be performed for every pixel in the spectrum image.....</i>	90
3.4:	<i>Schematic layout of the GIF Quantum ER spectrometer, which is ideally suited for STEM EELS acquisition and fast EFTEM mapping from a broad range of electron sources. The system has a standard 9 mm imaging aperture, a STEM detector, and an electrostatic shutter.....</i>	92
3.5:	<i>A background fitted before the O-K edge onset in order to achieve as sensible a fit as possible to both the O-K, and the Cr-L_{2,3} edges. The background fit was altered to include as little noise as possible, whilst encapsulating an accurate representation of each edge by selecting a sensible ELNES width, background window width and background model.....</i>	101
3.6:	<i>The deconvoluted and background-subtracted L_{2,3} energy loss spectra for the 4d transition metals [8].....</i>	102
4.1:	<i>Representative low loss spectra for each phase in the oxidised material, recorded for a Zircaloy-4 sample corroded in pressurised water reactor (PWR) conditions at 350 °C.....</i>	108
4.2:	<i>A plot of the Oxygen K edges for the zirconium Oxide (ZrO₂), oxygen saturated metal (Zr(O)) and the suboxide (ZrO) phases.....</i>	111
4.3:	<i>Zr-L_{2,3} ELNES for three phases: Zr metal, ZrO and ZrO₂.....</i>	112
4.4:	<i>EELS mapping of an oxide-metal interface in a pre-transition specimen. From top to bottom: Zr percentage composition map on a quantified colour scale; O percentage composition map on a quantified colour scale; multicolour composite image created from MLLS fitting of the low loss for each phase; line profile taken across the sample in the direction indicated by the arrow in the Zr percentage map, with an overlay box depicting the Zr(O) area.....</i>	114
4.5:	<i>EELS mapping of an oxide-metal interface in a specimen at transition. Along the top from left to right: Zr percentage composition map on a quantified colour scale; O percentage composition map on the same quantified colour scale; multicolour composite image created from MLLS fitting of the low loss for each phase. Bottom: line profile taken across the sample in the direction indicated by the arrow in the Zr percentage map, with overlay boxes depicting the Zr(O) and ZrO areas.....</i>	116

- 4.6:** *EELS mapping of an oxide-metal interface in a post-transition specimen. From top to bottom: Zr percentage composition map on a quantified colour scale; O percentage composition map on a quantified colour scale; multicolour composite image created from MLLS fitting of the low loss for each phase; line profile taken across the sample in the direction indicated by the arrow in the Zr percentage map, with an overlay box depicting the Zr(O) area..... 118*
- 5.1:** *EELS spectrum imaging of a Zr₂Fe SPP in the unoxidised metal: a) map of zirconium areal density; b) map of iron areal density; c) EEL spectrum showing iron-L_{2,3} edges at 721 and 708 eV respectively which depict a high Fe content within the SPP. The SPP contains no detectable Cr, as shown by the lack of the chromium-L_{2,3} edges at 584 and 575 eV respectively; d) a low magnification survey image of the specimen showing the SPP embedded in the metal ~ 3 μm from the interface..... 131*
- 5.2:** *EELS spectrum imaging of a Zr₂Fe SPP stranded in the oxide post corrosion: a) map of iron areal density; b) map of chromium areal density; c) a false coloured HAADF image of a different oxidised Zr₂Fe SPP showing the nanocrystalline nature of particle; d) a diffraction pattern from a scanned diffraction experiment on the SPP shown in a), a tentative indexing on the basis of a face centered cubic unit cell is included; e) an EEL spectrum showing the SPP body (red) and areas of Cr deposits (green); f) a low magnification survey image of the specimen showing the SPP encapsulated in oxide ~ 3 μm from the interface. The first transition region in the oxide can be seen to occur at ~ 2.5 μm from the metal:oxide interface. 132*
- 5.3:** *High-loss quantification of Zr(Fe, Cr)₂ SPP: a) map of zirconium areal density; b) map of oxygen areal density; c) map of iron areal density; d) map of chromium areal density; e) false colour RGB composite of SPP where green = Cr and red = Fe; f) a low magnification survey image showing the location of the SPP in the metal 135*
- 5.4:** *High-loss quantification of Zr(Fe, Cr)₂ precipitate at oxidation front showing: a) map of zirconium areal density; b) map of oxygen areal density; c) map of iron areal density; d) map of chromium areal density; e) RGB composite of all phases where pink = Zr, blue = O, red = Fe and green = Cr, with 3 areas highlighted and their corresponding; f) low-loss and; g) high-loss spectral signatures. 138*
- 5.5:** *High-loss quantification of Zr(Fe, Cr)₂ precipitate at oxidation front showing: a) map of zirconium areal density; b) map of oxygen areal density; c) map of iron areal density; d) map of chromium areal density; e) RGB composite of all phases where red = Fe and green = Cr, with 3 areas highlighted and their corresponding; f) low-loss and; g) high-loss spectral signature, and; h) low magnification survey image of SPP showing distance to metal:oxide interface..... 140*
- 5.6:** *High-loss quantification of Zr(Fe, Cr)₂ precipitate encapsulated by oxide showing: a) map of zirconium areal density; b) map of oxygen areal density; c) map of iron areal density; d) map of chromium areal density; e) scan diffraction image showing*

	<i>diffraction pattern of body of SPP; g) scan diffraction image showing diffraction pattern of Fe-rich veins of SPP and; f) RGB composite of all phases where pink = Zr, blue = O, red = Fe and green = Cr,] with 3 areas highlighted and their corresponding; h) low-loss and; i) high-loss spectral signatures; f) a low magnification survey image of the SPP in oxide, ~0.9 μm from metal:oxide interface.</i>	143
5.7:	<i>SPPs found in Zircaloy-2 material depicting all stages of oxidation, from still encapsulated by the metal matrix, right through to precipitates found at the farthest oxide (and therefore, subject to oxidation for the longest length of time). All initial mapping shows results which are consistent with findings from particles analysed within Zr-4 material.</i>	144
6.2:	<i>Spectrum imaging in a 1.6 μm oxide: a) A STEM survey image taken of a Zircaloy-4 specimen, where a spectrum image (SI) is acquired from the region inside the blue box. It can be clearly seen that the SI runs across a large crack; b) the oxygen content calculated from the SI running left to right.</i>	153
6.3:	<i>Three extracted EELS profiles from the initial, slow, and fast growth regions as shown in Fig. 6.2. The Zr M and O K edges can also be seen as insets to this figure.</i>	154
6.4:	<i>a) Spectrum imaging in a 4.7 μm oxide: a) A STEM survey image taken of a Zircaloy-4 specimen, where a spectrum image (SI) is acquired from the region inside the blue box. It can be clearly seen that the SI runs across a large crack; b) the oxygen content calculated from the SI running left to right.</i>	156
6.5:	<i>a) Spectrum imaging in a 2.78 μm oxide: a) A STEM survey image taken of a Zircaloy-4 specimen, where a spectrum image (SI) is acquired from the region inside the blue box. It can be clearly seen that the SI runs across the tip of a large lateral crack; b) the oxygen content calculated from the SI running left to right showing the 50 at. % O suboxide region and the 33.3 at. % oxygen saturated metal region; c) A further magnified section of the profile in the oxide, showing the O enriched outer oxide, the plateau region of ~ 65.5 at. % O in the region of uncracked oxide scale, and the oxygen elevated region surrounding the tip of the larger lateral crack.</i>	158

*“The good thing about science is that it's true
whether or not you believe in it.”*

— Neil deGrasse Tyson

chapter

1

Introduction

Zirconium alloys have been utilised as nuclear fuel cladding and other nuclear reactor components since as early as the 1950s [1, 2]. Initially used in a prototype nuclear reactor for submarines, they were subsequently utilised in the first commercial nuclear power reactors built in the 1960s [3]. Zirconium alloys are chosen for this application due to their low hydrogen pick-up from aqueous coolants, high corrosion resistance, good mechanical properties and favourable chemical stability in highly aggressive environments [4, 5]. As well as exhibiting both optimal mechanical properties and the best possible corrosion resistance under reactor conditions, zirconium is favourable as it has a desirably low neutron capture cross section (σ) of 0.18 barn [6]. This is much lower than that for other cladding materials such as stainless steel (3 barn) or aluminium (0.22 barn) [6, 7], giving zirconium a better

neutron efficiency in water reactors. Zr also has a considerably smaller σ than hafnium (105 barn) and tungsten (16 barn), which are chemically similar to, and very difficult to separate from, zirconium. Most common Zr ores contain between 1.5 and 2.5% Hf, and, due to its high thermal neutron capture cross section, hafnium must be removed from Zr for nuclear applications [5].

The high corrosion resistance of the material is due to the production of a protective, adherent oxide film formed due to the disassociation of water molecules on the outer surface of the oxide. This results in oxygen ions diffusing inwards towards the bulk metal, resulting in the creation of an oxide which grows into the metal. Thus, the metal-oxide interface is of particular interest as it is expected to play a key role in the overall corrosion of the material. Unfortunately, the protective nature of the oxide film is seen to break down once the oxide reaches a certain, critical thickness, which results in an abrupt increase in corrosion rate. This environmental degradation is life-limiting for these alloys.

As the primary motivation for this study is to more accurately predict the behaviour and lifespan of nuclear fuel rods, understanding how the metal-oxide interface develops during the corrosion process is vital. This has been achieved within this study by thorough analysis of the nanoscale structure and chemistry of the metal:scale interface, leading to a more accurate prediction of the performance of this existing alloy. Moreover, understanding how intermetallic precipitates oxidise as the oxide layer propagates through them is imperative, and connecting the oxidation of the particles to changes in the metal:oxide interface immediately surrounding the precipitate is vital, as has been shown in this thesis. Moreover, this work provides a realisation of oxygen content throughout the oxide scale in nanoscale detail, and gives an understanding not previously obtained on the complex corrosion process taking place, in order to gain an appreciation for this multi-faceted corrosion process.

1.1 Thesis Structure

This thesis will begin with a brief discussion of the history of zirconium for nuclear fuel containment in pressurised water reactors, including a discussion of the oxidation kinetics of the material, and comparisons with other material systems. Chapter 2 will provide a discussion of the sample preparation techniques used in this thesis, followed by a discussion of the instrumentation techniques, specifically focussing on the

Focussed Ion Beam (FIB) system, the Transmission Electron Microscope (TEM) and the Scanning Transmission Electron Microscope (STEM). In Chapter 3, the details of Electron Energy Loss Spectroscopy (EELS), and specifically the use of Dual Electron Energy Loss Spectroscopy (DualEELS) for characterisation of the alloy Zircaloy-4 will be discussed. The details of the post-processing techniques used to clean up the data will also be described. In order to study the nanoscale mechanisms of the corrosion of Zircaloy-4 in 350 °C pressurised water, mapping of the complex metal:oxide interface region pre-, at, and post-transition was performed using STEM and DualEELS, the results of which are provided in Chapter 4. Specifically, it has been found that under certain conditions, where the oxygen supply to the scale is plentiful, a metastable suboxide ZrO phase is seen to exist with an oxidation state of +2. Furthermore, in order to help inform the role of Secondary Phase Particles (SPPs) on the corrosion process, an analysis of the two varieties of SPP found in Zircaloy-4 is presented in Chapter 5. Spatially resolved quantitative mapping of elemental content depict how these precipitates oxidise in a notably different manner from each other, frequently containing metallic regions even when encapsulated by several microns of oxide. These precipitates have also been linked to cracking of the ZrO₂ scale. Chapter 6 then examines the connection between lateral cracking in the oxide scale, with oxygen content in the oxide. In particular, understanding the role cracks have in the migration of oxygen to the metal interface is discussed. Finally, Chapter 7 summarises all conclusions and outlines future work that should be implemented in the development of this research field.

1.2. Literature Review: Oxidation of zirconium and its Alloys

1.2.2. Structure of the literature review

The focus of this review is limited to characterising the oxidation behaviour of pre-irradiated Zircaloy-4 material, specifically focussing on the corrosion of the metal-oxide interface, and studying the alloying elements which are added to the matrix to improve its corrosion resistance. The effect of irradiation is not discussed here; however, there is a breadth of work available dedicated to the study of irradiated Zr alloys. The reader is directed to an older study by Gilbert *et al.* [8] who probed the damage structure in zirconium alloys in neutron irradiated, high temperature aqueous environments. They concluded that unfaulted dislocation loops were the principal form of damage in these alloys at temperatures of 300 - 650 °C, whereby the loops increased in size and decreased in density with increasing temperature. Newer works by Cox *et al.* [9] highlight that when reliable data from power reactor oxides became available, there was no evidence of irradiation enhancement of the diffusion controlled pre-transition corrosion rates on zirconium alloy oxide films. TEM studies showed little to no proof of displacement damage from fast neutrons, although fast neutron irradiation appears to affect the corrosion rate by redistributing alloying elements from secondary phase particles to a metastable solid solution in the zirconium matrix.

The effects of irradiation, specifically on precipitate stability in Zr alloys have also been studied in [10-12]. Motta *et al.* [10] concluded that the crystalline to amorphous transition of $Zr(Cr, Fe)_2$ precipitates in Zircaloy under neutron irradiation happened by a departure from stoichiometry due to ballistic interchange of iron and zirconium atoms across the precipitate-matrix interface. Moreover, they found that the amorphisation begins at the particle:matrix interface, and gradually moves into the precipitate.

One year later, a study by Pêcheur *et al.* [12] again focussed on studying the effect of irradiation on the precipitate stability in Zr alloys. They found that both $Zr_2(Ni, Fe)$ and $Zr(Fe, Cr)_2$ types of intermetallic precipitates found in Zircalloys were seen to amorphise under irradiation. Moreover, they conclude that the dose to amorphisation increases with increasing temperature, diverging when a critical temperature is reached. A later study by Jin *et al.* [11] corroborated the previous research, finding evidence of the crystalline to amorphous transformation when studying $Zr(Cr, Fe)_2$ and $Zr_2(Ni, Fe)$ precipitates in low irradiated Zircaloy 4 and 2, subject to relatively high neutron

fluencies consistent with research reactor operating conditions. This transformation was found to be highly dependent on the irradiation temperature and dose.

A second body of literature relates to hydrogen absorption and precipitation during corrosion in aqueous environments of the Zircaloy groups. Hydrogen absorption by the material was one of the earliest observations made and it has been shown that up to 120 wt ppm of hydrogen can typically be in solution in a zirconium alloy [13]. When this cladding is cooled, nearly all of the hydrogen precipitates to form 'in plane' brittle zirconium hydride platelets [13]. Hydride precipitation in Zr alloys is a complex process, and the effect that factors such as grain size, texture and applied or residual stresses have on the final morphology of the hydrides has been extensively reported in the literature [13-15]. The hydrogen production process has been seen to be life limiting due to hydrides mechanically weakening the fuel cladding as they have a much lower ductility and hardness than zirconium. Significant blistering and cracking of the alloy can result, leading to a scenario known as 'hydrogen embrittlement' [16, 17]. Coupled with this, it has been noted that a time-dependent mechanism of fracture that requires cracking of zirconium hydride has been responsible for several failures of zirconium alloy components in nuclear reactors – a process called Delayed Hydride Cracking (DHC) [18]. In this scenario, loading of cracking in a specimen induces hydride precipitation, and subsequent hydride growth. Thus, a vast array of research on the phenomenology and mechanisms of DHC in alloyed zirconium has been initiated. However, the relationship between the process of hydrogen uptake and precipitation and zirconium oxidation is a mutually dependent and complex one which must be dealt with separately, and therefore hydrogenation of Zircaloy-4 is beyond the scope of this thesis.

Whilst the regular corrosion of zirconium in high pressurised water occurs in a certain predictable fashion which will be examined further in this thesis, it is also recognised that under certain circumstances, nodular corrosion occurs. This rougher corrosion front develops under steam corrosion conditions (> 450 °C) such as are found in Boiling Water Reactors (BWRs). Readers may consult references [19-21] to gain a more detailed understanding of this process in the zirconium alloys.

This review will introduce the role of zirconium in the nuclear industry and draw comparisons between several zirconium-alloys which are/have been commercially used in reactor, detailing the motivation for the analysis of Zircaloy-4 in this work. The

creation and development of the oxide produced on the surface of the metal will then be discussed, with particular mention of the unusual corrosion kinetics zirconium undergoes. After the problem and materials have been fully described, a discussion will follow of the literature available which concerns any metastable suboxide phases which appear at the metal-oxide interface under certain conditions. Following this, the review will discuss the presence of secondary phase particles in the material, the purpose of their creation, and the state of knowledge of their oxidation behaviour. Finally, this thesis will conclude with a discussion on how additional new generation instruments such as Scanning Transmission Electron Microscopy (STEM) coupled with Dual Electron Energy Loss Spectroscopy (DualEELS) can aid to further elucidate the details of the life-limiting corrosion process taking place in Zircaloy-4.

1.3 Zirconium for Nuclear Fuel Containment

With the growing understanding of the link between carbon emissions and global warming, the topic of the environmental and safety viability of nuclear power generation has never been so urgent. It is known that one kilogram of ^{235}U yields approximately three million times more energy than one kilogram of conventionally burned coal [3], making nuclear power a major player in the effort to move towards cleaner energy production worldwide. In order however, to maximise the lifetime of a plant whilst minimising the likelihood of critical faults occurring, there is a huge push to understand how the microstructure of the cladding materials in Pressurised Water Reactors (PWRs) evolve over time. This involves a careful understanding of the fission reaction taking place in order to select the correct materials to contain (and maintain) this energy production, whilst ensuring that the integrity of the containment vessels is not compromised throughout the entirety of the plants' lifetime.

A nuclear fission reaction is based on the control of a nuclear reaction, where a large fissile nucleus absorbs a neutron through neutron bombardment. This process involves a heavy nucleus (for example ^{235}U) splitting into lighter nuclei and releasing a vast amount of energy in the process. This process results in the release of fast ($\sim 13800\text{km/s}$) [3] neutrons with an energy of 2 MeV each, which are ideally suited to go on and induce further fission reactions. In practice, this reaction can be controlled with a moderator such as D_2O . In order to minimise radiation exposure, the material for fuel cladding is chosen after other aspects of the reactor's core have been decided, such

as the coolant substance and the moderator material, ultimately constraining the options for viable fuel cladding materials. As alluded to in the introduction to this chapter, these constraints can be factors such as neutron cross section, mechanical strength, its chemical stability in highly aggressive environments, and corrosion resistance [5]. Having a good trade-off between a high temperature resistance and a low neutron absorption cross-section, zirconium based alloys have proven to be the optimal material for the containment of nuclear fuel [3].

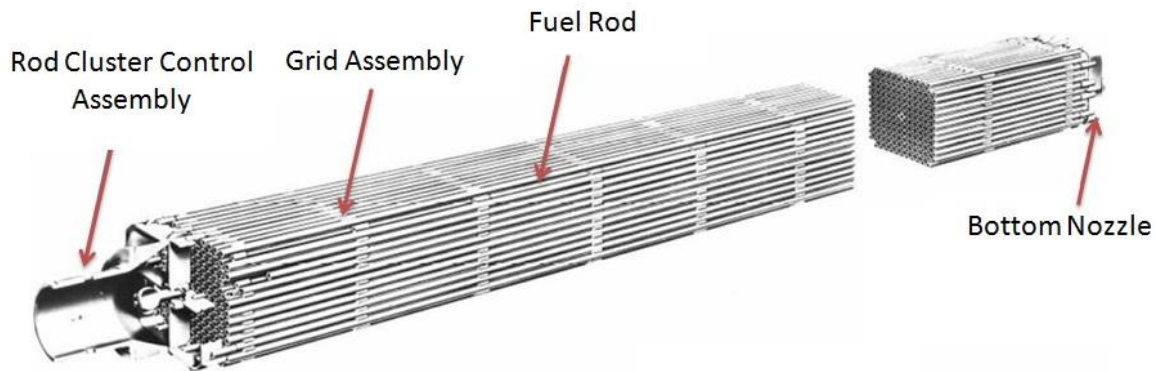


Figure 1.1: An illustration of the arrangement of a typical pressurised water reactor fuel assembly. Each fuel rod in the fuel assembly contains sintered pellets of low-enriched uranium within a zirconium-lined cladding. They are brought together in fuel assemblies where arrays of control rods are held in place by tie plates and spacers. Adapted from [7].

In water moderated reactors, arrays of zirconium alloy (Zircaloy) fuel rods, as shown in Fig. 1.1, enclose the UO_2 fuel. The fuel rod cladding is manufactured into long, thin tubes (average wall thickness ~ 0.6 mm and tube length ~ 4 metres) into which the UO_2 fuel pellets are fed. Pellets sit end-to-end inside the hollow cladding tubes of Zircaloy, which are around 1 cm across and are packed in square bundles, held together by spacer grids. This Zircaloy cladding is therefore the primary barrier between the nuclear fuel pellets and the reactor cooling water outside. Thus, any potential failure of the cladding tubes would result in the release of radioactive fission products into the cooling water.

Once the nuclear fuel in the reactor pressure vessel undergoes a fission chain reaction, a vast amount of heat is created, which is transferred to the water in the primary coolant loop by thermal conduction through the fuel cladding material. The hot primary coolant is then pumped into the steam generator, where several hundred small

tubes allow for heat transfer to the lower pressure secondary coolant. Here, the coolant converts to steam. A schematic of this process can be seen in in Fig. 1.2. It should be noted that the complete transfer of heat is achieved without mixing the two fluids, in order to prevent the secondary coolant from becoming radioactive. At this point the pressurised steam is directed through a steam turbine which drives an electrical generator connected to the electric grid for transmission. After passing through the turbine the secondary coolant is then cooled down and condensed in a condenser which converts the steam into a liquid. Before being fed into the steam generator, the condensed steam (referred to as feedwater) is sometimes preheated in order to minimise thermal shock.

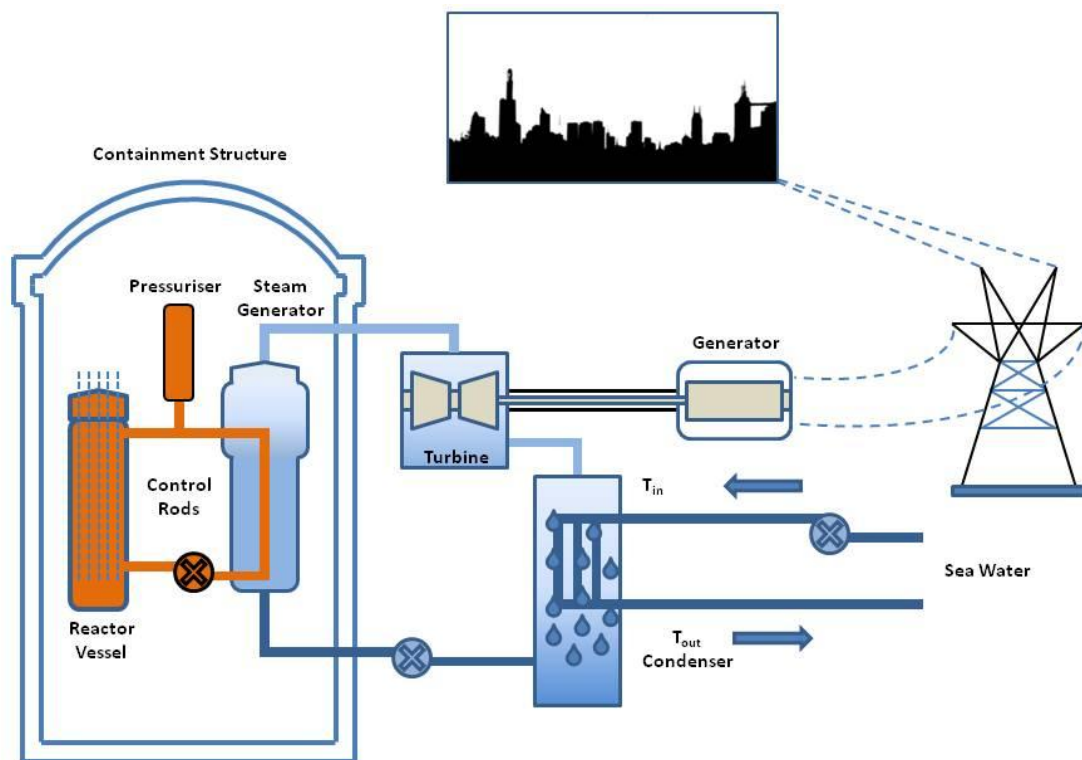


Figure 1.2: Pictorial explanation of power transfer in a pressurised water reactor. The primary coolant is in orange and the secondary coolant (steam and later feedwater) is in blue (adapted from [22]).

With increasing demand for high burn-up (i.e. lengthening the time the fuel remains in the reactor), in-service degradation of the cladding has now become the life-limiting factor for such fuel assemblies. Although the reactor core is designed to allow periodic inspection and removal of the rods, there are currently a significant number of rods which are removed from reactor unnecessarily, due to a lack of understanding of the corrosion of the fuel-clad assemblies.

1.4 Properties of Zirconium and its Alloys

The zirconium alloys in use today for nuclear applications are limited in number. In light water cooled nuclear reactors, Zircaloy-4 and Zircaloy-2 are the two most frequently used alloys: standard chemical specifications for these alloys are given in Table 1.1.

Table 1.1: Standard chemical specifications for Zircaloy-4 and Zircaloy-2 in the nuclear industry [23].

Alloying Elements Mass (%)	Zircaloy - 4	Zircaloy - 2
Sn	1.20 – 1.70	1.20 – 1.70
Fe	0.18 – 0.24	0.07 – 0.2
Cr	0.07 – 0.13	0.05 – 0.15
Ni	-	0.03 – 0.08

Zircaloy-2 is mainly used in fuel cladding in boiling water reactors (BWRs) and Zircaloy-4 is used in fuel cladding and for fuel components in pressurised water reactors (PWRs). This is due to the fact that in the late 1970's, nodular corrosion in BWRs and accelerated uniform corrosion in PWRs became an issue with the Zircaloy materials. Thus, differing ways to optimise the Zircaloy-2 and -4 for use in BWR and PWR applications was developed [24]. The main difference in the two alloys is that Zircaloy-4 contains slightly higher levels of iron and no nickel.

Zirconium has two crystallographic structures; an α -phase which is hexagonal close packed (HCP), and is stable at room temperature; and a high-temperature β -phase which is body centred cubic (BCC). The allotropic transformation of pure zirconium from the low temperature hcp α -phase to the bcc β -phase occurs at 863 ± 5 °C [6] at atmospheric pressure. The β to α phase transformation in Zircaloy commonly yields a Widmanstätten microstructure. The majority of alloying additions tend to be more soluble in the β -phase, whereas transition metals have a low solubility in α -phase zirconium [24]. By also having a high affinity for transition metals, the formation of SPPs is favoured in α -phase zirconium. All experiments within this PhD have been conducted at a temperature lower than that required to transform the α -zirconium into its β -phase. The common phases found in the major alloys are listed in Table 1.2. Pure

α -zirconium has lattice parameters with $a = 3.23 \text{ \AA}$ and $c = 5.15 \text{ \AA}$, which gives a c/a ratio of 1.593 [5], which is less than the ideal value of 1.63 (based on the hard sphere model). The presence of alloying elements and/or increased temperature is also known to increase the c/a ratio [22].

Table 1.2: Common phases occurring in the zirconium alloys, amended from [7].

Phase	Space Group	Symmetry	Atoms Per Unit Cell	a (nm)	c (nm)	Unit cell volume (nm ³)	Density (g.cm ⁻³)
α -Zr	-	Hexagonal	1.6	0.3231	0.5148	0.14	6.51
β -Nb	-	Cubic	1.2	0.33	-	0.036	8.59
Zr(Nb,Fe) ₂	P63/mmc	Hexagonal	3.12	0.5366	0.8792	0.658	7.5
(Zr,Nb) ₃ Fe	-	Orthorhombic	-	0.88	0.33	1.10	-
(Zr,Nb) ₄ Fe ₂	Fm-3m or F-43m	Cubic	6.16	1.215	1.794	-	7.1
Zr(Fe,Cr) ₂	Fd-3m	Hexagonal (T < 994 °C)	3.12	0.505	0.825	0.558	7.12
Zr ₂ (Fe,Ni)	I4/mcm	(T > 994 °C) Tetragonal	4.3	0.6385	0.5596	0.228	6.94

As is commonly the case in a metal that can undergo crystallographic phase transitions, different alloying elements can act to stabilise the two different phases. To improve the corrosion resistance of the zirconium metal, it can be alloyed with differing configurations of elements listed below, in varying concentrations:

- α -phase stabiliser: Sn, O, N, Be, Pb, Hf, Cd
- β -phase stabiliser: Fe, Cr, Ni, Nb, Mo, Cu, Ta, W, Ti, Mn, Co, Ag

Specifically, in the case of Zr-4, with the addition of alloying elements such as Sn, Fe and Cr to the Zr base metal, up to a value of about 2 wt. %, the corrosion behaviour of the material becomes more predictable and less prone to catastrophic breakaway corrosion.

Although alloying elements aid to stabilise the matrix, the corrosion process can never be halted entirely. It is therefore paramount that any corrosion processes taking place are well understood, so that one can accurately predict the behaviour of the corrosion and ultimately determine a more accurate lifespan of nuclear fuel rods. Increasing the lifespan of a reactor's core components whilst still maintaining an unaffected operational behaviour is of paramount importance to the nuclear industry

for many reasons including minimising waste production and the need for reprocessing and ensuring safe operation and prevention of accidental release of radionuclides into the cooling water. Thus, there has been a huge focus over many years on trying to understand the corrosion and hydride formation of several zirconium alloys. The requirements for improved performance of nuclear fuel assemblies and structural parts, predominantly in relation to corrosion resistance, has resulted in fuel designers and metallurgists undertaking intensive research in order to improve the properties of Zr alloys by advanced compositions and thermo-mechanical processing, and to optimise the microstructure. Although there is a broad range of research dedicated to trying to bring about a greater understanding of the corrosion mechanisms of Zircaloy, existing techniques and previous studies have not been able to elucidate the details of the corrosion process.

1.5 Oxide formation on zirconium

By placing a zirconium alloy in contact with hot water (as for instance happens in pressurised water reactor or boiling water reactor designs) it reacts with the water resulting in oxidation of the surface and the liberation of hydrogen. Oxygen dissolution into the Zr matrix during oxidation can take place due to the fact that it is thermodynamically more favourable for oxygen to be dissolved in the metal ($ZrO_{0.05}$ and $ZrO_{0.1}$) than to form the oxide layer, as can be seen in Fig. 1.3.

The viability of the reaction between zirconium and oxygen depends on the Gibbs free energy change, which must be negative for this reaction to occur spontaneously at constant temperature and pressure. This is only satisfied if the dissociation pressure of the oxide is less than the partial pressure of oxygen, at which point, the zirconium will begin to form an oxide layer on the surface of the metal, which will reach a thickness of a few nanometres [25].

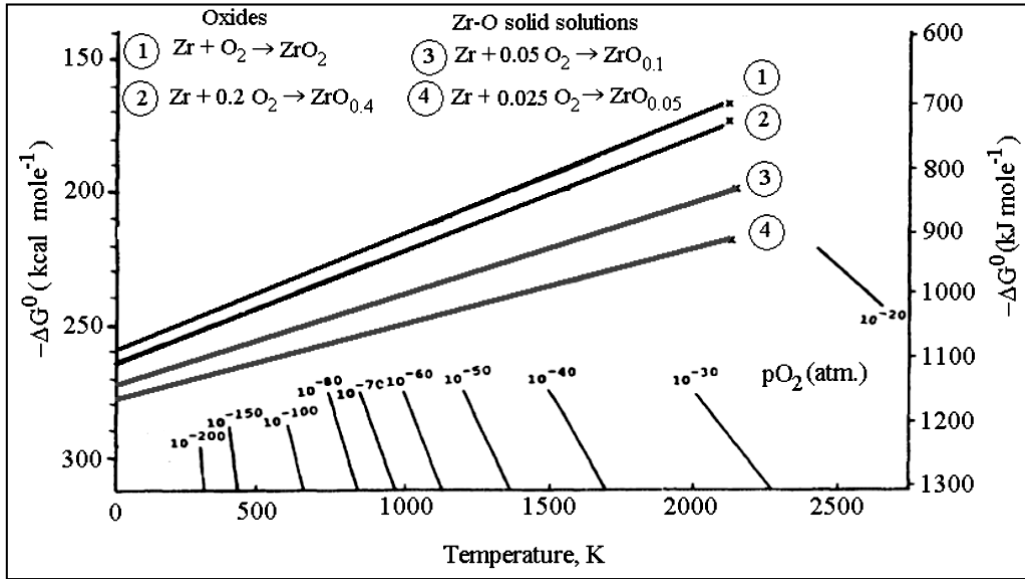


Figure 1.3: Ellingham diagram of Zr-O system, from [25].

The general corrosion kinetics of a zirconium alloy in pressurised water (as seen in Fig. 1.4) begins with the rapid growth of a thin oxide layer on the clean zirconium surface, which quickly decreases to follow a square or cube root of time [2, 26, 27].

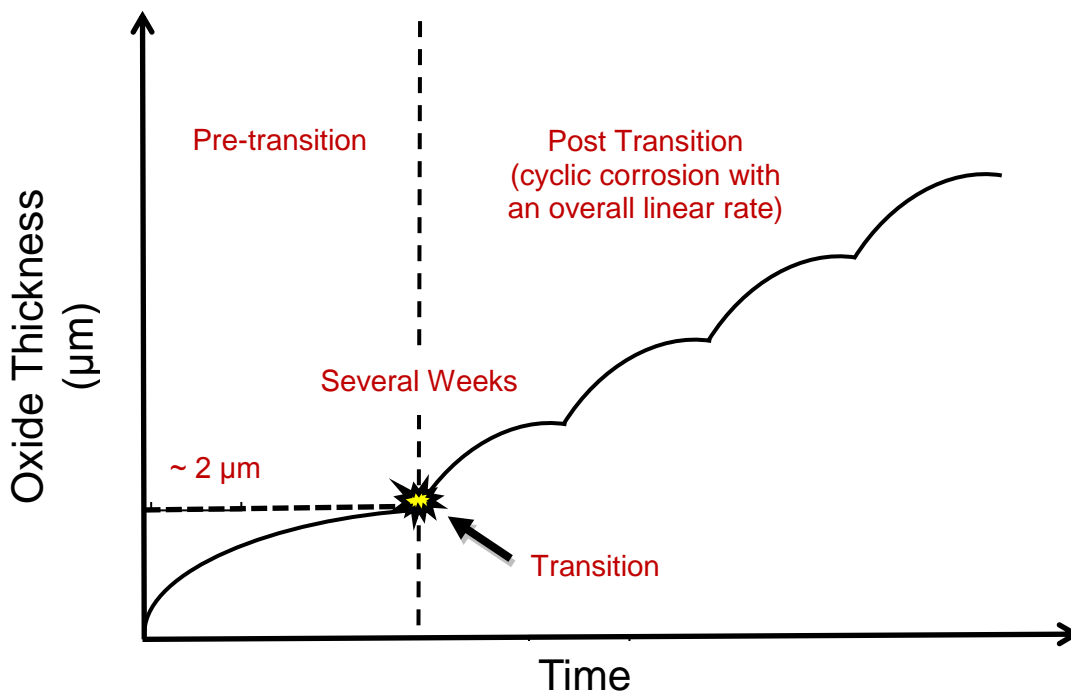


Figure 1.4: Typical oxidation kinetics of a generic zirconium-based alloy. After the pre-transition region where the oxidation kinetics follow a square/cubic relationship, depending upon the oxidising environment, the protective layer breaks down and cyclic oxidation proceeds with an overall linear rate. The critical thickness before transition occurs is usually of the order of $\sim 2 \mu\text{m}$.

This period is termed *pre-transition* and can be fitted using the power law equation;

$$\Delta W = Kt^n . \quad (1.1)$$

(where W is the weight gain in mg/dm^2 , K depends on both the alloying elements and the reactor temperature, the exponent n is determined experimentally and t is the oxidation time in days). This occurs up until an oxide layer of roughly $2 \mu\text{m}$ has formed on the surface of the metal. At this critical thickness (indicated by an arrow in Fig. 1.4), the previously protective oxide begins to break down and the corrosion rate proceeds more rapidly again. This is often termed the *transition*. This process may be repeated cyclically several times, until the oxide thickness grows almost linearly with time [9]. Post-transition corrosion generally follows an expression of the form;

$$\Delta W = Kt + C . \quad (1.2)$$

(where C is the initial weight gain). It should be noted that this movement from a slow, to a more rapid corrosion rate, is entirely separate from the phenomenon known as 'breakaway' oxidation. 'Breakaway' oxidation occurs during a design-based accident such as loss-of-coolant accident (LOCA), whereby the integrity of the fuel cladding is lost, and its ductility greatly reduced. The effect known as 'breakaway' will not be covered in detail in this thesis, but may be read about in more depth in [2, 28, 29].

A low magnification dark field electron micrograph can be seen in Fig. 1.5, with all noteworthy regions of interest noted on the figure. This is provided as a reference to the reader, in order to visualise the regions noted in this thesis and gain an appreciation for the complexity of the corrosion of zirconium alloys.

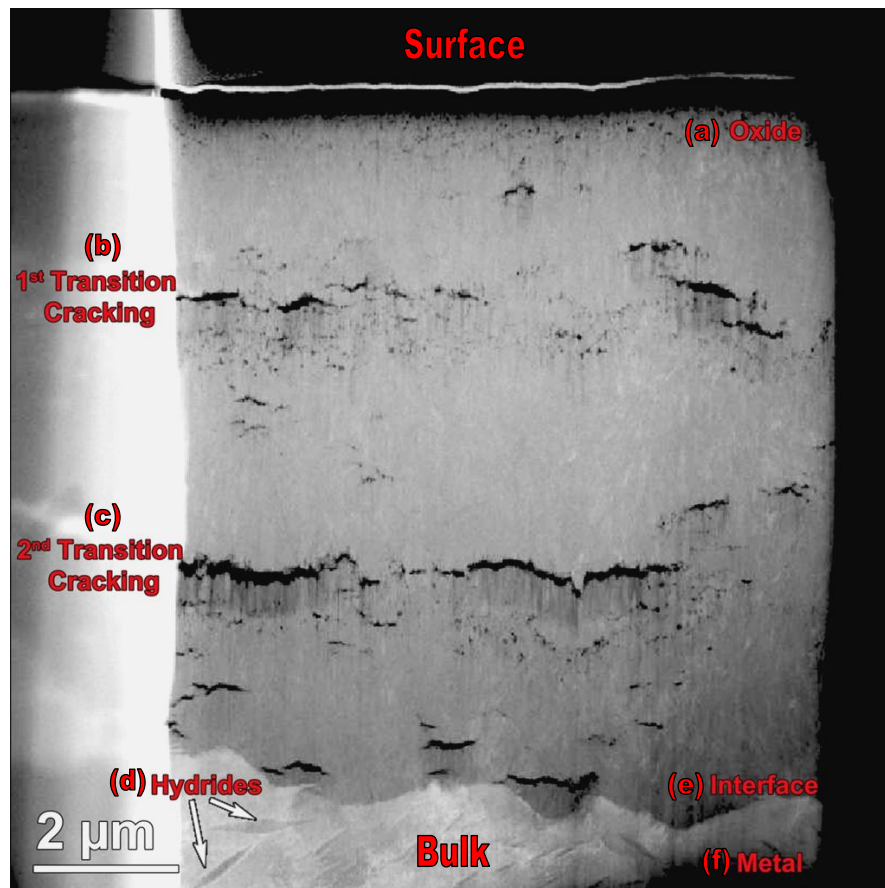


Figure 1.5: A low magnification dark field electron micrograph of a Zircaloy-4 sample with $\sim 6 \mu\text{m}$ oxide on the surface, showing a) oxide b) first transition cracking c) second transition cracking d) hydrides, e) a large scale undulating metal:oxide interface and f) the metal matrix. The bright region on the left is simply platinum deposited in order to attach the sample to the holder. This image also shows the bright layer of sputter coated gold at the surface used to protect the sample from ion beam damage. Curtaining caused by thinning during sample preparation can also be seen below cracks.

Although the oxidation kinetics of zirconium have been extensively documented by a variety of methods, the cause of the rate change from pre-transition, to post-transition, has not yet been fully realised. Transmission electron microscopy (TEM) [30-34], scanning electron microscopy (SEM) [30, 35-38], microbeam synchrotron diffraction [39, 40], x-ray diffraction [41], x-ray spectroscopy (EDS) [42], scanning transmission electron microscopy [43], and electron energy loss spectroscopy (EELS) [34, 44] investigations have all been undertaken in order to study the micro- and nano-structure of the oxide, as well as the oxidation behaviour of these alloys.

Resultantly, the corrosion of zirconium is still currently the focus of intense research in all countries using commercial nuclear power. One model is that faster routes for oxygen transport to the interface are created through pores and cracks perpendicular to the interface, which allows for the transport of oxygen to the metal-oxide interface [45].

In order to study long term corrosion of Zircaloy, before and after irradiation, Hillner *et al.* [46] gathered approximately 14500 data points over a maximum of 10507 days. It was found that where the maximum corrosion scale thickness did not exceed 30 μm , there was a single linear post-transition rate constant, whereas, at the highest temperatures where oxide film thicknesses exceeded 30 μm , two successive linear equations could be used to describe the data. The discrepancies in these findings were undoubtedly down to the fact that the corrosion thicknesses found at low temperatures were too thin to have reached the second transition point, and progress into the stage two kinetic region.

Motta *et al.* [40] studied oxides formed on three different alloys (Zircaloy-4, ZIRLO and Zr2.5Nb) in both regular and lithiated water in order to model the growth of oxide layers formed on Zr alloys, and found that a regular periodicity in the corrosion process took place. This was repeatedly found using several different techniques (transmitted light optical microscopy, synchrotron radiation and TEM) which all corresponded well to the oxide transition thickness. They proposed a mechanism for oxide growth, which resulted in accumulation of stresses in the bulk oxide, and cracking to occur which resulted in the sample undergoing global transition.

Bouineau *et al.* [47] both described and modelled the effect of different environmental parameters on the corrosion of Zircaloy-4. Their model predicted the oxidation kinetics of zirconium alloys in pressurised water reactors, which considered variables such as temperature, irradiation, heat flux and hydriding and was based on a phenomenological approach where the oxidation kinetics were characterised by a cyclic repetition of a semi-parabolic law. It was found that the oxidation kinetics clearly showed a periodic behaviour, which was connected to the creation of periodic lateral cracks in the oxide layer and was observed both in out-of-pile loop and PWR tests. This strongly supports the theory that periodic corrosion kinetics occur both in and out of reactor. This is relevant to work within this thesis, as corrosion data acquired on non-irradiated samples will be directly relatable to in-reactor specimens. The corrosion kinetics of Zircaloy-4 could therefore be illustrated as a periodic repetition of a cubic law, more than likely due to the diffusion of oxygen into the zirconia layer, and the kinetic acceleration due to the transition. The authors explained the transition process as an accumulation of stresses in the oxide layer which ultimately reach a critical point,

resulting in the creation of lateral cracking, releasing stress, and initiating the acceleration of the growth of the oxide layer.

In all these studies, the association between the transition and lateral cracking in the oxide layer depicts some interaction between the mechanical behaviour of the system, and its corrosion kinetics, but does not provide a clear understanding of the morphology of the metal:oxide interface during the corrosion process, at the nanometre level. This work will develop a more refined understanding of this process by studying the oxide scale and the top layers of the metal at nanometre resolution to reveal the detailed structural and chemical changes associated with diffusion of oxygen and the resulting oxidation of the metal. Deciphering why this transition behaviour happens is critical when modelling the rate of growth of oxide, and therefore to the lifetime prediction of Zr clads, and ultimately to the safety of nuclear power reactors.

1.6 Oxide Microstructure

As the demand for zirconium based alloys to perform better in highly aggressive aqueous environments increases, understanding the microstructure of oxide layers grown on zirconium has become more prevalent. Furthermore, minimising hydrogen pickup is a huge driving factor in order to improve the corrosion resistance of the alloy by reducing hydride formation and embrittlement, and thus, decreasing the potential for cladding failure due to delayed hydride cracking (DHC). Specifically, the microstructure of the oxide has been found to have a significant effect on the corrosion performance of zirconium alloys [48]. Electron microscope studies by B. Cox [2] revealed that initially, the thin oxide film created on the surface of the Zircaloy contained many orientations of small equiaxed crystallites. As this oxide layer grew however, some of the orientations grew preferentially, producing a columnar oxide structure with a strong fibre texture at the metal:oxide interface.

It is also well known that alloys with large columnar grains tend to have lower corrosion rates than those which exhibit smaller grains [31]. This superior corrosion resistance is thought to arise due to the reduction in grain boundary area in oxides which have large grains, as the grain boundary diffusion coefficient is 10^8 times higher than the bulk diffusion coefficient of the oxide [32]. Moreover, M. Glavicic [49] revealed using X-ray diffraction (XRD) analysis, that reduced levels of hydrogen pickup, as well as a better corrosion resistance, is seen in oxides which exhibit a higher texture strength.

Recently, A. Garner *et al.* [32] used Transmission Electron Backscatter Diffraction (t-EBSD) to link the microtexture, and thus the grain boundary character distribution in the oxide, to the corrosion performance of zirconium alloys. They agreed with Cox, in that the oxide microstructure consists of an outer layer of equiaxed grains with a large range of orientations and an inner layer consisting of well-aligned columnar monoclinic grains, with a high fraction of transformation twin boundaries. This layer of equiaxed grains was observed to form again after the transition in corrosion kinetics. Thus, there is postulated to be a continuous process taking place when the oxide scale reaches its critical thickness, and a conversion from tetragonal to monoclinic ZrO_2 occurs, leaving behind repetitive layers within the oxide, as stress-stabilized tetragonal grains with (001) planes parallel to the metal-oxide interface transform into columnar grains.

1.7 Suboxides

Many sub-oxide phases have been reported in zirconium-related literature, using a variety of techniques and considering various sections of the oxide. These observations usually relate to regions adjacent to the metal-oxide interface of corroded material. A phase diagram of the Zr-O system can be seen in Fig. 1.6. Studies undertaken by Puchala *et al.* [50] confirm that as hexagonally close-packed Zr is able to dissolve unusually high amounts of oxygen into its interstitial octahedral sites, it has the ability to create a range of ordered suboxides up to a composition of ZrO . All of these contain oxygen in octahedral interstices. All were predicted to be metallic. Thus, the oxygen environments in ZrO and in the lower suboxides should be very similar.

Early experiments using an AEI EM7 electron microscope allowed Moseley *et al.* [51] to study the phases involved in the corrosion of Zircaloy-2 by hot water at 350 °C. By taking selected area diffraction patterns, it was deduced that a structure of Zr_3O was present within the sample. They also postulated that a sodium chloride type structure of ZrO was highly likely to exist in small quantities, the presence of which performed a transient role, rather than a final oxidation product. The presence of a metastable oxygen-enriched band-like region at the metal-oxide interface was also suggested by Bossis *et al.* [52] and determined to have an ω -Zr hexagonal structure by analysis with TEM and energy-dispersive x-ray spectroscopy (EDX), but the exact composition of the phase was not postulated. This ω -Zr phase was discovered by Frost [53] and the phase diagram documented by Hickman [54] in 1969. This phase is seen to occur during

quenching of Zr where the high-temperature BCC structure can be retained as a metastable state and transformation to the usual low-temperature HCP structure is suppressed. This phase is not detailed in Fig. 1.6, but can be read about in more detail in references [53, 54].

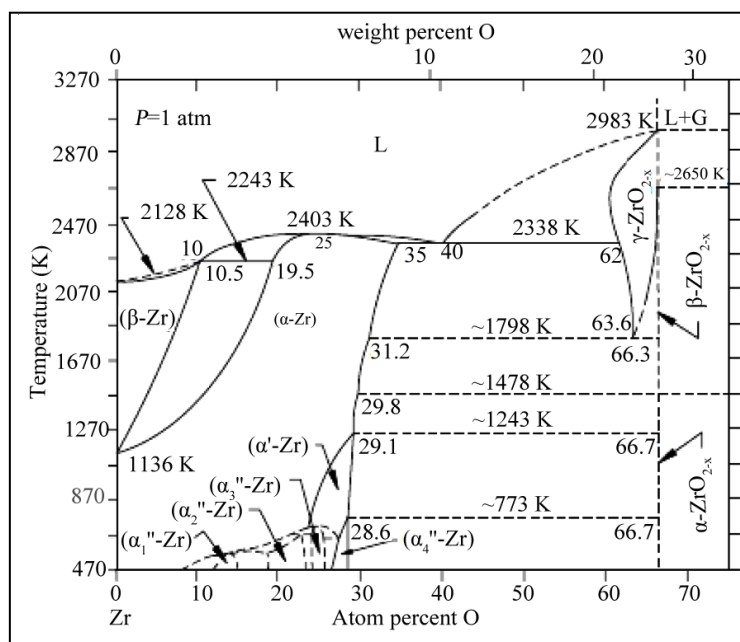


Figure 1.6: Equilibrium phase diagram for the Zr-O system, after N. Selmi *et al.* [55].

In order to determine a more detailed understanding of the morphology of any suboxide layers present, Yoshitaka *et al.* [56] used Auger Electron and X-ray photoelectron spectroscopy on samples of zirconium and Zircaloy-2. The comparison between corrosion in oxygen and water vapour at room temperature was made and three suboxides of Zr_2O , ZrO and Zr_2O_3 were found to occur on surfaces in both the oxygen and water vapour atmospheres. Early in the oxygen exposure ($<5L$ where $1L \equiv 10^{-6}$ Torr s)), and water vapour period (up to $30L$), the primary suboxide found was Zr_2O . This suboxide was then found to undergo transformation from a +1 (Zr_2O) state, to a +4 (ZrO_2) state successively. Formation of a +2 state (ZrO) occurred after an exposure of $30L$ or higher in both environments.

Following this, Yilmazbayhan *et al.* [31] carried out cross sectional TEM investigations. They postulated from Energy Dispersive X-ray (EDX) spectroscopy that there may be evidence of a Zr_3O suboxide phase due to a gradual decrease in oxygen content from ~ 67 at.% in the bulk oxide to a level of ~ 29 at.% of oxygen solid solution in Zr. This was seen over a considerable distance from ~ 160 nm to ~ 560 nm in oxides

formed on three different alloys: Zircaloy-4, Zr-2.5Nb and ZIRLO. More recently, Ni *et al.* [57] used electron energy loss spectroscopy (EELS) in order to quantify the oxygen content at the metal - oxide interface in a pre-transition ZIRLO sample after a range of pressurised water treatments. After calibration against a ZrO_2 powder standard, they were able to determine zirconium:oxygen ratios with good accuracy using a *k*-factor approach, at least for sample thicknesses less than 75 nm. Systematic differences in the local oxygen profile across the interface in different zirconium alloys were found. They concluded that in their pre-transition sample, a plateau region of around 130 nm wide in the oxygen concentration with a constant value of 50 ± 2 at.% between the ZrO_2 at 65 ± 1 at.% oxygen, and the metal, 31 ± 2 at.% oxygen was apparent, consistent with the presence of a suboxide phase above the Zr metal saturated with oxygen, and as consistent with findings in this thesis. They also noted that the interface region of a post-transition oxide showed no evidence of any intermediate suboxide, consistent with findings in this work, as shown in Fig. 4.6.

By studying the microstructure of the metal-oxide interface region of Zircaloy-2 after autoclave corrosion testing, Tejland *et al.* [58] confirmed the presence of a substoichiometric oxide layer, formed at the metal-oxide interface, which was found by EDX line scans across the metal:oxide interface to have an oxygen content of approximately 50 at. %. This suboxide was consistently found to have a thickness of around 200 nm. As expected, the oxygen concentration was found to be around 67 at.% in the outermost part of the oxide, giving confidence in the EDX quantification. There was also found to be an oxygen concentration gradient into the metal in the region of 200 nm, from a level similar to the suboxide of about 30 at.%, down to a few atomic percent. All tin from the metal matrix was found to be incorporated into the suboxide layer, and there was no evidence of any segregation to the metal:suboxide interface.

Subsequently, Ni *et al.* [33] performed TEM high angle annular dark field (HAADF) imaging of Zircaloy-4 samples and found no evidence of a suboxide after 7 days of aqueous corrosion (15.3 mg dm^{-2}). After 114 days of corrosion, the same material produced a weight gain of 23.4 mg dm^{-2} . Atom probe tomography (APT) analysis highlighted an extremely well defined suboxide phase of a composition not dissimilar to ZrO occurring between the metal and the ZrO_2 oxide. TEM analysis of these pre-transition samples depicted a well defined intermediate phase after 34, 54 and 90 days of corrosion. In addition to the suboxide layers, oxygen-saturated (30 at.% O) metal

regions were found by both TEM and APT analysis beneath the interface in most of the samples studied. These were found to be thickest in the very late pre-transition samples and were significantly thinner in the post-transition samples.

Dong *et al.* [59] also studied the oxide scale morphology and oxide phases within three samples - pure Zr (crystal bar), Zircaloy-4, and Zr-0.4Fe-0.2Cr using atom probe tomography. Specimens were prepared from the oxide and oxide-metal interface regions from the three materials. A series of oxygen containing phases were found for all three alloys - a stable oxide ZrO_2 (in contact with water), the suboxide ZrO , a saturated solution of constant oxygen content at about 30% O - $Zr(O)_{sat}$ - and an undersaturated solid solution of O in Zr, denoted $Zr(O)$, which had a decreasing oxygen content with distance from the oxide-metal interface. For Zircaloy-4 in particular, it was found that it follows a similar oxide sequence as that seen in crystal bar Zr, but with thicker intermediate layers of ZrO and $Zr(O)_{sat}$. They also observed the same effect as Ni *et al.* [33] whereby at low corrosion rates, the width of oxygen saturated zirconium was larger. Moreover, they noted that whilst the morphology of the oxide-suboxide interface was relatively uniform, the interface between the suboxide and the oxygen saturated metal exhibits 'semi-elliptical regions' of suboxide advancing into the oxygen saturated metal region.

Later studies by Tejlund *et al.* [60] used TEM and HAADF contrast to confirm the existence of a wavy metal:oxide interface which undulates on a micrometer scale, but also has irregularities on a finer scale resulting in the formation of metal islands at wave crests. A suboxide layer was found to occur adjacent to the metal oxide interface, with a 45-55 at.% oxygen composition. Again, the metal matrix was found to saturate with up to 32 at.% oxygen, and the oxygen concentration profile into the metal matrix was found to be consistent with diffusion data for pure zirconium, although the oxygen diffusion profile was found to be wider under a metal hill, rather than at valleys.

All this presents strong experimental evidence that the ZrO phase is definitely seen in oxidation under conditions of slow oxide growth and thus restricted oxygen supply. There was however, until recently, little definite evidence about the structure of the phase since it is only ever metastable and is not easily formed in bulk. Early investigations by Schönberg [61] suggested a rock salt structure akin to α -TiO [62]. Puchala and Van der Ven [50] considered a number of possible structures using Density

Functional Theory (DFT) modelling including the δ -ZrO phase mentioned above and a δ -ZrO phase analogous to δ -TiO [63]. It was shown by atomistic modelling that the stable structure for ZrO is a modified form of the δ -TiO phase [50, 64], which has been denoted δ' -ZrO. It was then confirmed by Nicholls *et al.* [64] using convergent beam electron diffraction that ZrO suboxides in both corroded Zircaloy-4 and ZIRLO samples do indeed exhibit the theoretically predicted hexagonal δ' -ZrO structure. Subsequently, Hu *et al.* [43] were able to consistently map the presence of δ' -ZrO at a metal-oxide interface using transmission electron backscatter diffraction (t-EBSD) and to correlate this to compositional measurements by EELS of a ZrO composition in corroded Zr-0.1%Nb alloys.

This thesis applies DualEELS (discussed in full detail in Chapter 3) on a modern aberration-corrected STEM to the study of the evolution of the ZrO suboxide phase throughout the corrosion process, as well as revealing further details of its chemistry by analysis of the details of the EEL spectra. Although there is solid evidence in the literature that the ZrO suboxide phase presents itself under certain specific conditions, a study is lacking which correlates morphology of the interface at several points in the corrosion process with spatially resolved, quantitative mapping. The work presented in this thesis aims to directly address this issue, results of which are highlighted in Chapter 4 of this thesis. State-of-the-art instrumentation used in this work, allows for mapping of large areas of the oxide and metal, harnessing data in a detail which has not previously been applied to this materials system. Moreover, detailed correlated mapping between the electronic structure in the low loss and the chemical information from the high loss datasets is attainable, results of which are presented in Chapters 4, 5 and 6 of this thesis.

1.8 Secondary Phase Particles

With the addition of alloying elements such as Sn, Fe and Cr to the Zr base metal, up to a value of about 2 wt.%, the corrosion behaviour of the material becomes more predictable and less prone to catastrophic breakaway corrosion. The Fe and Cr alloying elements are shown to have a solubility of < 150 wt. ppm in Zr-1.4% Sn [65], and 290 wt. ppm [66] in Zircaloy-4. Therefore, much of the content of these elements precipitate during the alpha-phase annealing as intermetallic-Zr compounds, which sit as precipitates within the base metal [9]. It should be noted that improved corrosion

resistance with the addition of alloying elements is not always the case, such as is seen in some binary alloy systems. Although the addition of Cr to a Zr base alloy improves the alloy's resistance to oxidation [67], this improvement is offset by the fact that the introduction of $ZrCr_2$ Laves phase precipitates to the matrix can result in embrittlement of the material [67]. In the Zr-Fe alloy system, the Laves C15- Fe_2Zr phase is found to be the most stable phase [68], although others (such as c- $FeZr_2$), relatively less so [68]. Precipitates in the Zr1%Fe system have also been seen to show an increased oxidation rate when in contact with the gas:oxide surface [69].

There are two primary types of SPP which are found within Zircaloy series alloys, namely $Zr_2(Ni, Fe)$ and $Zr(Fe, Cr)_2$ type precipitates. The former is an intermetallic C16 phase (isostructural with $CuAl_2$), frequently seen in Zircaloy-2 [38, 70-72], whereas the latter mostly appears as a hexagonal intermetallic Laves phase with the C14 structure, and is seen frequently in both Zircaloy-2 and -4 [70-77]. Early work by Chemelle *et al.* [70] aimed to investigate the morphology and composition of SPPs in Zircaloy-2, using transmission electron microscopy (TEM). They found that all precipitates were either nickel-bearing with a tetragonal Zr_2Ni -type phase (where iron partially substitutes for Ni), or chromium-bearing with a hexagonal $ZrCr_2$ -type phase (where iron partially substitutes for Cr). No iron-zirconium particles were found. Later, Charquet [65] showed that an increase in the iron content has a beneficial effect on the resistance to corrosion in steam. However, the results reveal that, in a Zr-1.4% Sn matrix, the influence of iron alone, in an amount equivalent to the (Fe + Cr) content in Zircaloy-4, is less effective than the simultaneous addition of iron and chromium. Therefore, it was decided to study the influence of the Fe/Cr ratio in Zircaloy-4 type matrices. It was deduced that the optimum corrosion resistance is obtained for Fe/Cr ratios in the range from 1.5 to 5. They noted that, for ratios less than 4, the only intermetallic precipitates observed correspond to the classical $Zr(Fe, Cr)_2$ phase, in which the proportions of iron and chromium are similar to their nominal concentrations. On the other hand, it was found that for larger Fe/Cr ratios, there were further phases of the type Zr_2Fe and Zr_3Fe , highlighting that the substitution of Cr by Fe in $ZrCr_2$ is limited.

In order to better understand both types of SPPs, Meng *et al.* [71] performed an analysis of precipitates in Zircaloy-2 using TEM and energy dispersive X-ray spectroscopy (EDS). The most common precipitate found was the $Zr_2(Fe, Ni)$ -type with two size ranges, the larger ones being found at the α -Zr grain boundaries. They had a

composition of $Zr_2(Fe_{0.4-0.5}Ni_{0.6-0.5})$, and a body-centred tetragonal structure. The smaller of these particles were found to be generally smaller than $1\ \mu m$ and had an elliptical shape. The second SPP type found was the hexagonal $Zr(Fe, Cr)_2$ Laves phase with a composition of $Zr(Cr_{0.55-0.57}Fe_{0.45-0.43})_2$. These particles had a size similar to the smaller ($<1\ \mu m$) $Zr_2(Fe, Ni)$ precipitates and were also found to contain frequent parallel stacking-faults and the expected hexagonal C14 structure. It should be noted however, that an SPP size of $1\ \mu m$ is around 5 times larger than what would be expected in the largest SPPs in industrial alloys (of the order to $100 - 200\ nm$). As Zircaloy-2 has a different composition to Zircaloy-4, the corrosion resistance will differ between alloys, and thus, this reference may not be entirely adequate for comparison between SPP size in work by Meng *et al.* [71], and the current study.

Literature suggests that the size, chemical composition and distribution of the intermetallic precipitates $Zr(Fe, Cr)_2$, in Zircaloy-2 and -4 and $Zr_2(Fe, Ni)$ in Zircaloy-2 is significantly altered during the oxidation process by retarding or anticipating the transition of the oxidation process or by enhancing pre- and post-transition oxidation rates [74]. However, there are still many outstanding questions about the exact mechanisms. It is understood that the corrosion resistance is microstructure-dependent, with the size, distribution and amount of second phase particles being of particular importance [78]. In particular, it has been noted that favourable nodular corrosion resistance requires fine precipitates [79], whereas a certain minimum particle size is necessary for satisfactory uniform corrosion behaviour [80].

The oxidation of the Laves phase precipitates has been studied previously using conventional TEM and spot analysis with EDS. Pêcheur *et al.* [74] showed after oxidation in steam at $400\ ^\circ C$ that such precipitates in Zircaloy 4 are often oxidised after the surrounding Zr matrix is oxidised to ZrO_2 , that some diffraction patterns from oxidised SPPs could be consistent with a tetragonal ZrO_2 phase, and that some iron was redistributed as bcc metallic iron within the oxidised particles. De Gabory *et al.* [77] also recently concluded that the oxidation of such C14 Laves phase precipitates results in nanocrystalline areas with a large phase content of tetragonal ZrO_2 . Pêcheur [81] studied the oxidation of similar precipitates in Zircaloy-4 in superheated lithiated water. They found that it is not until $\sim 300\ nm$ from the metal-oxide interface that SPPs begin to oxidise, and iron depletion is observed. It is suggested that due to the dissolution of iron from the precipitates to the surrounding zirconia matrix at this point,

the alloying elements can modify the inner oxide grain properties, such as stabilising the tetragonal ZrO_2 phase. There are also reports in Zr-1%Fe alloys of iron oxide precipitates in the oxide [69], although their structure was not determined, and there was no quantification of their exact composition. There are, however, very few observations of Zr_2Fe precipitates in Zircaloy-4 [82] and no known studies of the oxidation of such particles.

In summary, the key outstanding issues are that nowhere in the literature has a study been done which quantitatively maps the elemental composition of precipitates found in Zircaloy-4 pre-, at, and post-transition. Likewise, there is no known previous work which directly links internal structure of oxidised particles, with the morphology of, and their distance from, the metal:oxide interface. Similarly, a comparison has never been presented highlighting the contrast between the homogeneity in the oxidation of Zr_2Fe particles, and the huge segregation within the SPP into chromium and zirconium mixed oxide regions and metallic bcc iron regions seen in $Zr(Fe, Cr)_2$ particles. This current work addresses these issues by presenting a systematic study of the structure and chemistry of SPPs in Zircaloy-4 after corrosion in pressurised water at 360 °C covering both Zr_2Fe and $Zr(Fe, Cr)_2$ type precipitates. Specifically, mapping of the chemistry using electron energy loss spectroscopy (EELS) spectrum imaging using DualEELS has allowed for the acquisition of spatially resolved quantitative maps of elemental content with few nanometre resolution. This is in part, combined with scanned diffraction, specifically to make clear the crystallographic structure within the nanocrystalline oxidised SPPs, and elucidate in detail the oxidation process taking place.

“The World is full of wonders, but they become more wonderful, not less wonderful when Science looks at them”.

— David Attenborough

chapter

2

Sample Preparation and Instrumentation

In order to probe the nanoscale details of Zircaloy-4 material using Scanning Transmission Electron Microscopy (STEM), it is imperative that samples be uniformly thin (~ 100 nm) to enable the incident beam of electrons to be transmitted through the sample. Moreover, it is often required that samples be fabricated to span a large section of material, as the entirety of the oxide layer, the metal:oxide interface and a section of the bulk metal is of interest. Due to the nature of the corrosion of zirconium alloys, as has been discussed in Chapter 1, this regularly means that a sample is often required with cross sections several microns in depth: samples with oxide thicknesses of up to $13\ \mu\text{m}$ were prepared during this PhD. Producing a sample with these properties is crucial, and is best achieved using the FIB lift-out technique [83] which has

been employed to fabricate all samples during this PhD. Moreover, although there is a broad range of research dedicated to trying to bring about a greater understanding of the corrosion mechanisms of Zircaloy, there are many details of the corrosion process that have been insufficiently explained by previous studies using existing techniques. Recent progressions in the development and implementation of electron energy loss (EEL) spectroscopy however, have been great, and this method has been used extensively within this project. Coupled with this advancement, is the continuing improvement in the manufacturing of transmission electron microscopes (TEMs) and scanning transmission electron microscopes (STEMs) with correction of chromatic or spherical aberrations within electron lenses. Combining EEL spectroscopy with imaging on a modern aberration-corrected STEM has not only provided the required technology with which to produce detailed maps of the interface and SPPs, but has allowed professionals to take massive leaps in developing the understanding of materials at the sub angstrom level, so that we can probe into the mechanisms of corrosion of Zircaloy-4

2.1 Oxidation Experiments by AMEC Foster Wheeler

All bulk specimens analysed within this project were corroded by AMEC Clean Energy Europe. This is due to the specialised equipment needed to provide high pressures and temperatures which samples were required to be placed under, as well as the relatively long duration (up to several hundred days) in which the samples need to be subject to these conditions for.

In order to achieve an optimally ductile final product, with minimal deformation dislocations, the Zircaloy-4 material must undergo specific processing stages. Details of general industrial processing of Zr alloys can be read in [5]. The strict details of the processing stages of specimens analysed within this thesis are proprietary information, however the general details are as follows. After initial casting, the material is solution heat treated to a temperature in excess of 1000 °C in order to dissolve dendrite structures before being quenched to a Widmanstätten structure [84]. Deformations within the material are then greatly increased upon cold rolling, before the material is annealed in order to reorganise dislocations which nucleate new grains, and result in an equiaxed α -phase structure which will bulge and deform as required. Full details of the temperatures and times for each of these stages can be seen in Fig. 2.1.

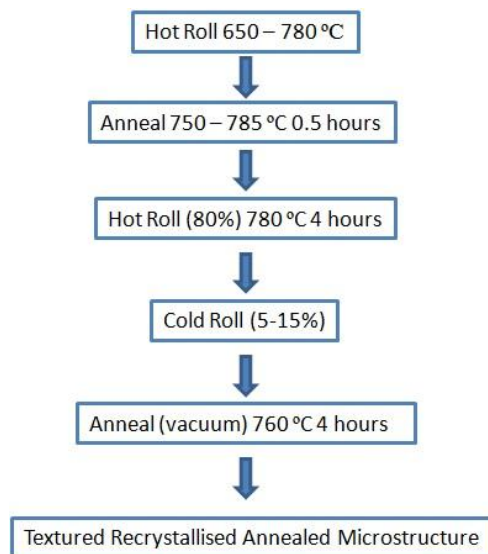


Figure 2.1: Processing history of the reference Zr-4 sheet material.

The recrystallised annealed (RXA) Zircaloy-4 (Zr-1.5%Sn-0.2%Fe-0.1%Cr) which begin as coupons, are then initially prepared by first mechanically polishing them to remove surface scratches before pickling them in an HF solution to remove 50 μm of material from all surfaces, followed by immediate rinsing in demineralised water. The coupons were then exposed to pressurised water at 180 bar and 350 $^{\circ}\text{C}$ with a room temperature pH of 10 in 316 stainless steel autoclaves with an internal volume of 8 L. Coupons were corroded in rig with a hydrogen overpressure of 1.2 bar (average dissolved hydrogen content was measured to be 3.65 ppm using a calibrated hydrogen orbisphere) for various durations to simulate PWR in-reactor conditions [85, 86]. Following each test, coupons were removed, washed with deionised water and dried in an oven at 40 $^{\circ}\text{C}$. Calculated oxide thicknesses were average thicknesses, as inferred from weight gain measurements using the relationship $15\text{mg}/\text{dm}^2 = 1\mu\text{m}$.

2.2 Focussed Ion Beam (FIB)

Offering both high-resolution imaging and flexible micro-fabrication in a single platform, the focused ion beam (FIB) system has gained widespread use in fundamental materials studies and technological applications over the last few decades.

All samples within this thesis were prepared using a Nova Nanolab 200 DualBeam FIB. This instrument consists of a vacuum system and chamber, a liquid metal ion source, an ion column, a sample stage and detectors, as can be seen in Fig. 2.2.

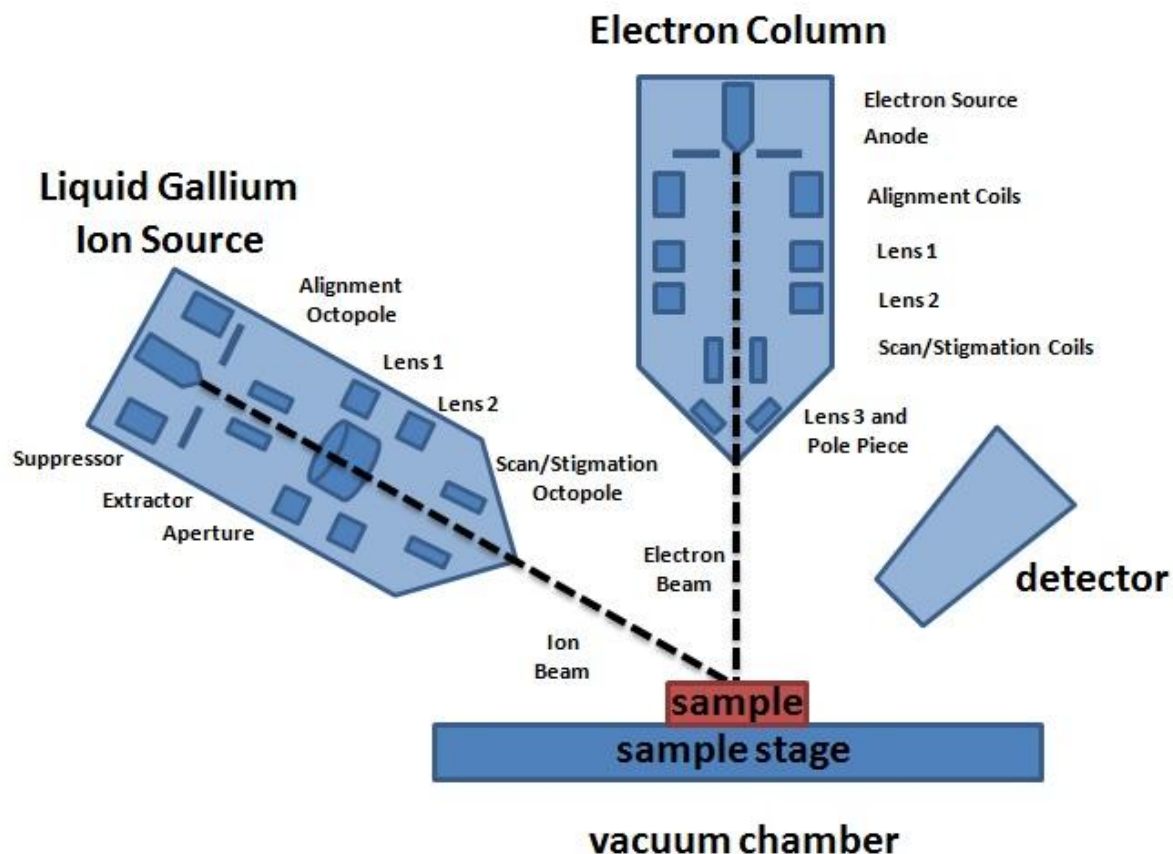


Figure 2.2: A schematic of the FIB system showing the Ion and Electron columns and the sample inside the vacuum chamber.

The ion column typically has two lenses: the condenser lens (lens 1 in Fig. 2.2 which is probe forming) and the objective lens (lens 2 in Fig. 2.2, used to focus). The typical ion beam accelerating voltage in FIB systems ranges from 1 to 30 keV, with the majority of sample fabrication done at 30 kV and the 5 keV beam used for final thinning, to minimise beam damage to the specimen. A set of apertures define the probe size and provides a range of ion currents (10 pA – 30 nA). Typically, currents any greater than 0.92 nA are not used as this level of current cuts through material much too fast, and fine control of the beam is lost. Octopole lenses perform multiple functions such as beam deflection, alignment, and stigmation correction.

In the FIB, secondary electrons may be detected and used to construct an image of the sample for both electron and ion beam imaging. The range of the magnification of the electron beam (30 x to 1.28 million x) is slightly less than that of the ion beam at 152 x to 1.28 million x.

The capabilities of the FIB for small probe (diameter ~ 5 nm) sputtering are made possible by the liquid metal ion source (LMIS). Gallium is currently the most commonly used LMIS for FIB instruments due to having a low melting point, low volatility, low vapour pressure and excellent mechanical, electrical, and vacuum properties. In conjunction with the gas-injection capabilities on these systems, which enable ion-beam-activated deposition and enhanced etching, a range of sample fabrication schemes are possible.

2.2.1 FIB Lift-Out Technique

Since the 1990s the focused ion beam (FIB) lift-out technique has been exploited for site-specific transmission electron microscopy (TEM) and other analytical usage [83]. This so-called lift out technique was first proposed by Overwijk *et al.* [83] and has since been developed into a routine technique for a broad range of materials. In theory, with an achievable probe diameter of 5 – 7 nm and the capability of precise sample positioning, an electron-transparent lamella can be extracted from virtually any region of interest in a bulk specimen without the need for mechanical polishing. Specifically, this technique involves extracting a site specific sample which causes minimal damage to the bulk material. By firstly delineating a region of interest and FIB-depositing a sacrificial layer of protective platinum, the sample surface can be protected from Ga implantation, before trenches are milled on either side of the area of interest. This allows for the extraction of a thin central section, which can be cut from the bulk, attached onto a grid and thinned to < 100 nm for analysis in an electron microscope.

2.2.2 Experimental FIB Conditions

After corrosion in a reactor, a segment of the coupon was cut by AMEC Foster Wheeler, and provided to Glasgow University for final sample preparation and analysis. A schematic of the layer structures found in a typical coupon is highlighted in Fig. 2.3.

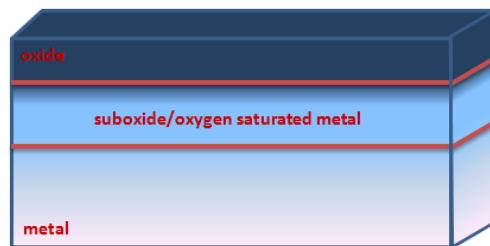


Figure 2.3: Schematic of a typical section of a coupon showing from top down, the oxide layer built up on the surface of the metal, the suboxide or oxygen rich layers, and finally the base metal at the bottom.

Initially, the sample is protected by the evaporation of about 30 nm of gold, performed by an Emitech (Quorum) sputter coater at 20 – 25 mA for a few minutes. Such sputtering is a physical vapour deposition (PVD) method, whereby atoms are removed from a user selectable conducting target and deposited onto the surface of a substrate. The sputtering source employs a DC magnetron which utilises strong electric and magnetic fields to confine charged plasma particles close to the surface of the sputter target. Using argon as a sputtering gas increases the number of ionising collisions taking place, resulting in an (almost) 360 ° coating range. Having the sample mounted on a rotating platform ensures for the creation of a highly insulating conducting film across the entirety of the specimen. This pre-fabrication step was employed as it was seen that thick insulating oxides on the surface of samples resulted in frequent and excessive charging of the sample under the focussed ion beam, which resulted in an unmanageable beam drift. The result was that precious areas of the sample may be subject to accidental milling. Now, although the application of this metallic coating mitigates charging, it should be noted that it can introduce additional complications with sample preparation. For example, one is not always able to see defining surface features when the specimen is coated, and to this effect, controlling coating thickness and noting the desired lift-out area pre-coating is imperative.

Following gold coating, a 10 μm x 2 μm rectangle of first electron (400-500 nm), and then ion beam platinum ($\sim 2 \mu\text{m}$) is deposited on the area to be extracted - the result of which can be seen in Fig. 2.4a. The layer of electron beam platinum is deposited at 5 keV, 1.6 nA, before a thicker region of ion beam platinum is deposited at 30 keV, 1nA. This is performed in order to reduce gallium implantation in the sample surface. By then tilting the stage to 52° on each side, trenches can be cut out in front and back of the deposited platinum using 30 kV gallium ions, as can be seen in Fig. 2.4b. It should be noted that the longer the sample required, the greater chance the sample has of

breaking or warping under the beam upon thinning, and the more difficult it is to attach to a grid for analysis in the electron microscope. Due to the nature of this project, analyses of all the layers present in the sample were required, including the entire oxide layer. In Fig. 2.4b, one can see that the trenches were made deep enough to take a sample which included the deposited platinum on the surface of the material, the oxide layer(s) beneath this, and several microns of the metal below the oxide. The specimen could then be tilted back to 7° and all of one side, the bottom, and a portion of the other side removed, the result of which can be seen in Fig. 2.4c. The specimen could then be attached to a probe tip using ion beam platinum deposition, before the sample was fully cut away from the bulk and manipulated to a TEM Omniprobe™ lift-out grid and micro-welded to the grid using FIB platinum metal deposition. The probe could then be cut away, and final thinning using 5 kV gallium ions performed until the sample thickness was ideally < 100 nm. A final thinned specimen ready for analysis in the STEM can be seen in Fig. 2.4d. This is an example of a specimen with a particularly large oxide layer, of around $13\ \mu\text{m}$.

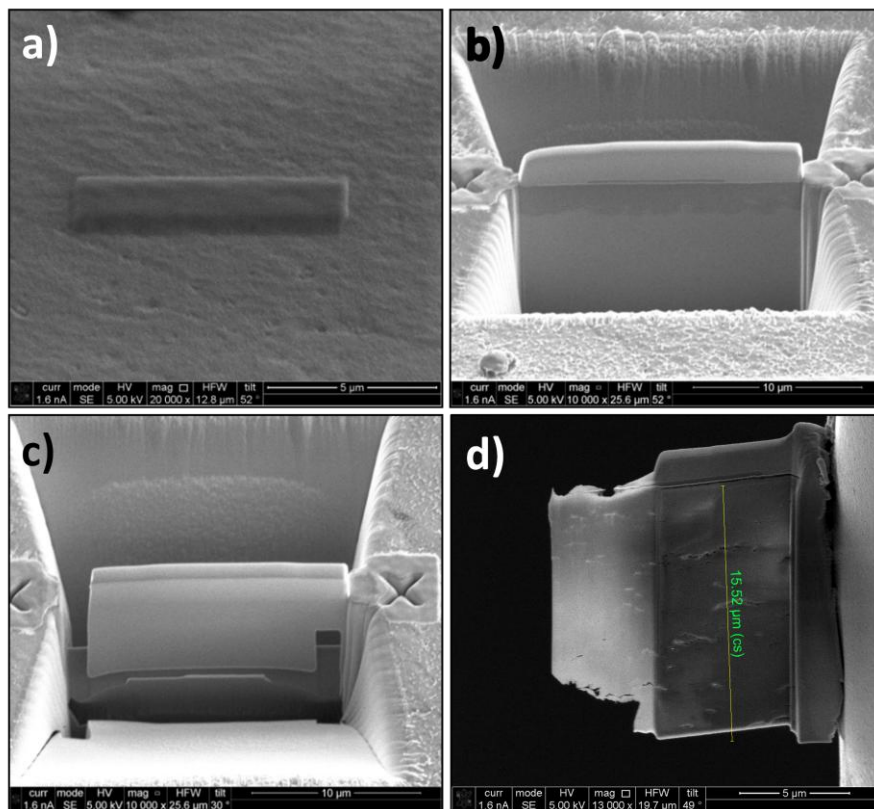


Figure 2.4: The TEM lift-out procedure where a) platinum is deposited over the region of interest, b) cuts are made to the front, back and one side of the section, c) the section is tilted and cuts made on all but part of one side, d) the final thinned specimen attached to a TEM Omniprobe™ lift-out grid, ready for S/TEM analysis.

This meant that during this technique, the *only* modification of the sample was a set of FIB cuts adjacent to the region of interest, as can be seen in Fig. 2.4b. In practice, samples were often somewhat difficult to prepare due to the large amount of oxide on the surface of the bulk metal, which had built up over weeks of corrosion in the rig. This resulted in attempting to fabricate a sample which needed to span several (sometimes almost tens of) microns, in order to encompass the outer oxide layer, any potential suboxide or oxygen saturated layers present, and several microns of metal. Fabricating a sample with this length, whilst ensuring it was less than 100 nm in thickness was extremely difficult and often was only possible with fully manual operation of the FIB. This meant that any automatic procedures for cutting the trenches either side of the section was not applicable, and repetitions of milling and tilting manually had to be implemented until the required depth was acquired. Often, this greatly increased the time which had to be dedicated just to lift-out one sample from a bulk specimen.

Once samples were successfully lifted, attached to a grid and thinned, they were ready to be thickness checked in a Tecnai T20 Transmission Electron Microscope, before being analysed in detail using a JEOL ARM 200F Scanning Transmission Microscope, details of which can be read about in section 2.4 and 2.8 of this thesis, respectively.

2.3 Electrons for Imaging

In 1873 Ernst Abbe [87] postulated that the resolution of a visible light microscope (VLM) was limited by the wavelength of the light used in imaging, and that the detail of an object could only be resolved to a few hundred nanometres. The optical resolution limit of the magnification system was determined by Abbe, using equation 2.1 (the Abbe diffraction limit), where λ is the wavelength of light and NA is the numerical aperture;

$$\rho = \frac{\lambda}{2NA} . \quad (2.1)$$

Actually, NA is equal to $n \sin \theta$ (where n is the refractive index of the medium multiplied by the sine of the aperture angle $\sin(\theta)$) which can reach around 1.4 - 1.6 in modern optics, resulting in an Abbe limit of $\rho = \frac{\lambda}{2.8}$. If we consider green light of 500 nm and a NA of 1, the Abbe limit is roughly $d = \frac{\lambda}{2} = 250$ nm. This restriction in the

resolution of imaging precipitated an intense period of development in microscopy techniques, which resulted in the invention of the electron microscope, thanks to the pioneering work of Louis-Victor de Broglie [88] and Max Knoll and Ernest Ruska [89]. Their work was based on Albert Einstein's early work on the photoelectric effect whereby he postulated that light energy is quantised into discrete elements, with particulate qualities, called photons. This allowed Louis-Victor de Broglie [88] to introduce the concept of wave particle duality. The suggestion that *all* matter, not just light, may be described in terms of not only particles, but also of waves, paved the way for the introduction of the de Broglie wavelength (equation 2.2), which defines the wavelength of light, λ , as Planck's constant, h , over its momentum, p .

$$\lambda = \frac{h}{p} \quad (2.2)$$

This formula was confirmed three years later for electrons with the observation of electron diffraction in two independent experiments, in the UK and in the US, in 1927. The first, by George Paget Thomson [90] at the University of Aberdeen, observed predicted interference patterns when passing a beam of electrons through a thin metal film. At Bell Labs in the US, it was Clinton Joseph Davisson and Lester Halbert Germer [91] who corroborated findings from Thomson when they passed their beam of electrons through a crystalline grid.

The invention of the electron microscope by Knoll and Ruska [89] at the Berlin Technische Hochschule in 1931 using lenses of the type pioneered by Busch led the way for other researchers to join the development effort to gradually improve the resolution of the conventional electron microscope.

Whereas early versions of the electron microscope simply sought out to prove that an electron beam could in fact be controlled to provide images of matter, by the late 1930s electron microscopes were being designed and manufactured by Siemens and Halske, with theoretical resolutions of 10 nm. By 1944, a resolution of 2 nm was achieved – an improvement of more than 100 times better than a visual light microscope (VLM) [92]. Since then, optimised lenses now allow users to achieve a resolution of less than 2 Å at 200 kV and 1 Å at energies > 1 MV. If aberration correction is also available (which can be read about in detail in section 2.7 of this thesis), it is now possible to achieve 0.5 Å at 200-300 kV beam energies.

The anatomy of a TEM from the top down includes: an emission source, a condenser system, a specimen, an objective system, a projector system and a detection system. All microscopy work undertaken within the scope of this thesis, has been completed using a FEI Tecnai 20 (T20) and a JEOL ARM 200F (STEM). These microscopes will be detailed in sections 2.4 and 2.8 of this thesis, in order to convey the significance of electron microscopy in the field of condensed matter physics.

2.3.1 Electron Matter Interactions

The basis of transmission electron microscopy is the interaction of a uniform, beam of energetic electrons with a thin material specimen. When electrons enter this solid, they interact with the constituent atoms within the sample through electrostatic (Coulomb) forces [93]. The result of which, is the scattering of some of the incident electrons. Electrons that are not transmitted directly will either be elastically (where there is a negligible amount of energy exchange), or inelastically (where a considerable amount of energy is transferred from electron to atom); in addition they will also experience a change in momenta.

In Fig. 2.5, one can see the interaction between the electron beam and the sample.

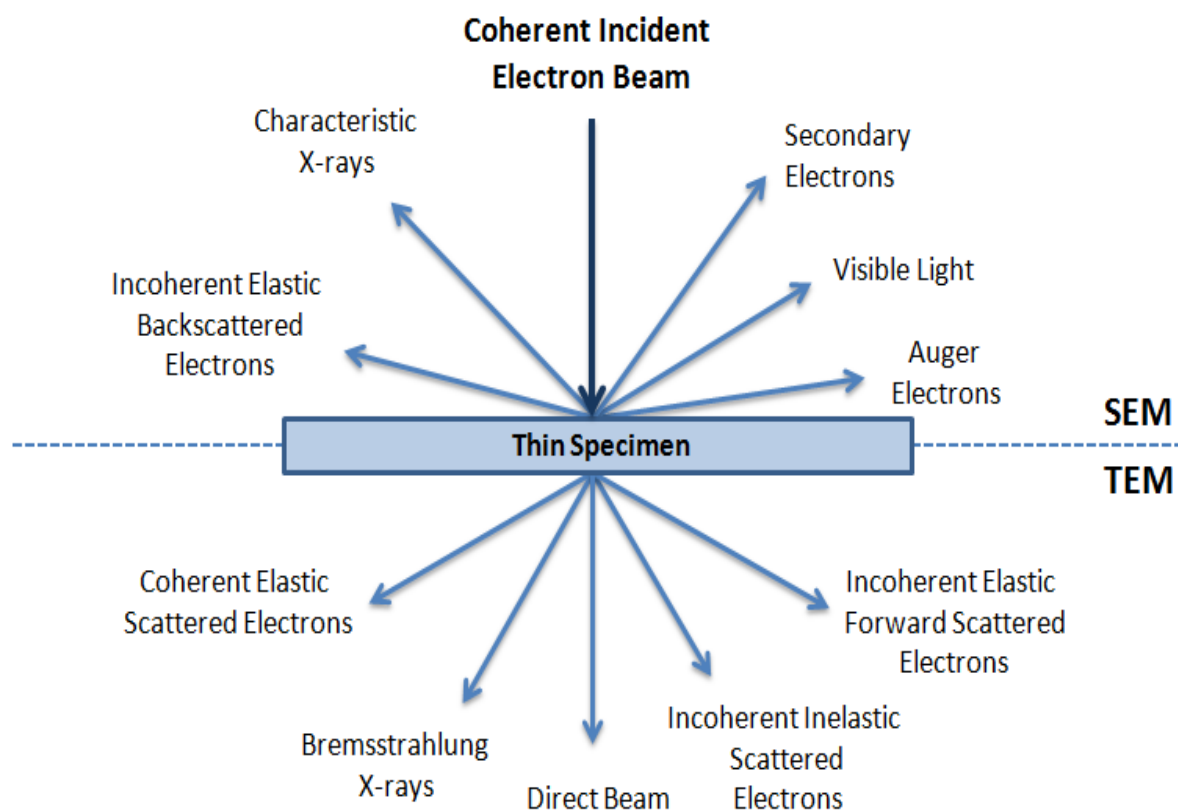


Figure 2.5: Schematic of the interaction between a thin specimen and an incident electron beam.

Elastically scattered incident electrons are deflected from their original path by atoms in the specimen and suffer no loss of energy whereas inelastically scattered electrons lose energy during their interaction with atoms in the specimen. Elastically scattered electrons follow Bragg's Law;

$$n\lambda = 2d\sin\theta . \quad (2.3)$$

where n is a positive integer, d is the interplanar distance, θ is the scattering angle and λ the wavelength of the incident wave. All incidents which are scattered by the same atomic spacing will therefore be scattered by the same angle. Elastic scattering is usually coherent provided that the specimen is thin and crystalline. As there is a significant concentration of charge within the small confines of an atomic nucleus, any incident electron beam which passes close to the nucleus [94] will be deflected through a large angle, referred to as Rutherford scattering, and as can be seen in Fig. 2.6a. This term was coined by Ernest Rutherford in 1911 [95] when studying the scattering of alpha particles, leading to the model of the atom, and resultantly, the Bohr model of the atom. His name is also utilised to describe any electron which is deflected by an angle $> 90^\circ$, emerging from the same surface of the material from which it entered – called Rutherford backscattering. Again, this event can be seen in Fig. 2.6a. However, this only represents a miniscule fraction of the elastically scattered electrons. In a material which has a reasonable concentration of conduction band electrons, dielectric screening will cause a reduction in the electrostatic field of the nucleus the further from the centre of the atom the electron travels. This results in the majority of electrons travelling further from the centre of the atom where the electrostatic field of the nucleus is weaker due to the inverse square law. Therefore, most electrons will be scattered through small angles of a few degrees ($0-10^\circ$) [94]. In a crystalline solid, interaction between the scattered electron waves alters the continuous distribution of the scattered intensity into one which is peaked at angles representative of the atomic spacing. This elastic scattering is then referred to as diffraction.

Inelastic scattering occurs through Coulomb interaction between an incident electron and the *atomic electrons* which surround the nucleus. First, we will consider the interaction of an incoming fast electron and an *inner shell electron*, as seen in Fig. 2.6b (where one electron is promoted into a Bohr orbital of higher quantum number) or, Fig. 2.7 (to a higher energy level). In this instance, the ground-state energy of the inner shell electron will lie hundreds of electron volts below the Fermi level of the solid.

For this electron to be removed from its ground state, it must absorb energy from an incoming electron which is greater than or equal to its binding energy, resulting in an upward trajectory towards an unoccupied state above this Fermi level. This will result in the incoming fast electron being scattered through an angle of several mrad, having lost an equal amount of energy as was required to promote the inner shell electron to a higher energy level. The inelastic loss of energy by the incident electrons is characteristic of the elements that were interacted with. These energies are unique to each bonding state of each element (as can be seen in Fig. 2.7) and thus can be used to extract both compositional and bonding (i.e. oxidation state) information on the specimen region being examined. Inelastically scattered electrons can thus be used for electron energy loss spectroscopy (EELS). The de-excitation process then involves an outer-shell electron transitioning down into the core hole left behind, resulting in the liberation of X-rays, or as kinetic energy of another atomic electron.

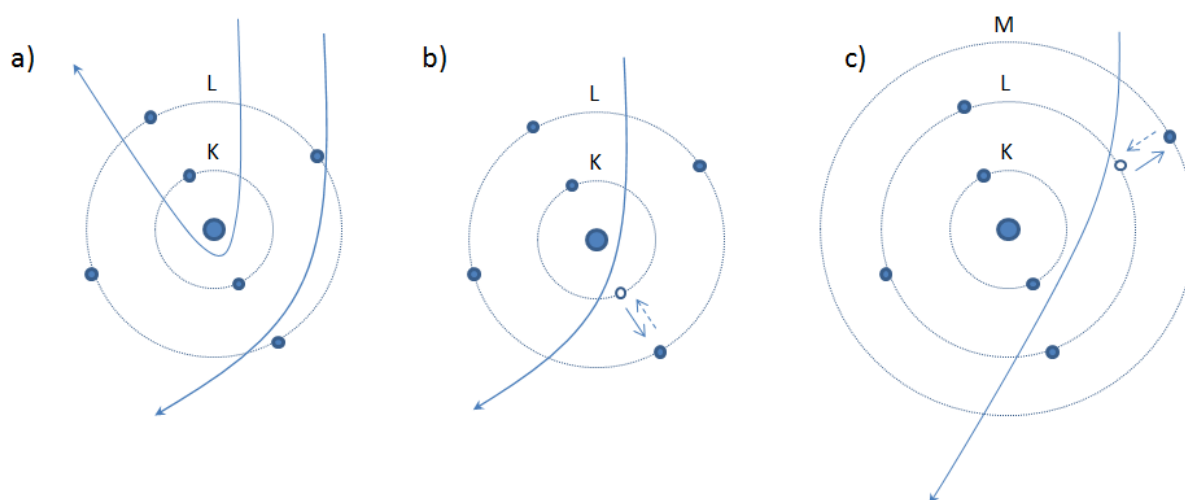


Figure 2.6: A particle view of electron scattering. a) Elastic scattering is caused by Coulomb attraction by the nucleus. Coulomb repulsion causes inelastic scattering in b) Inner- and c) Outer-shell electrons, which are excited to a higher energy level.

Now, if we consider the interaction of *outer-shell* electrons with not a single electron but as a collective effect involving many atoms of the solid, we can define a plasma resonance. This takes the form of a longitudinal wave, and involves sharing excess energy among many atoms when viewed over an extended time period. Normally, the plasmon energy lies in the region of 5-30 eV, where the essential requirement for plasmon excitation is that the participating electrons are able to share energy with each

other. This condition is achieved by a band of delocalised states, but does not hold for the atomic core levels.

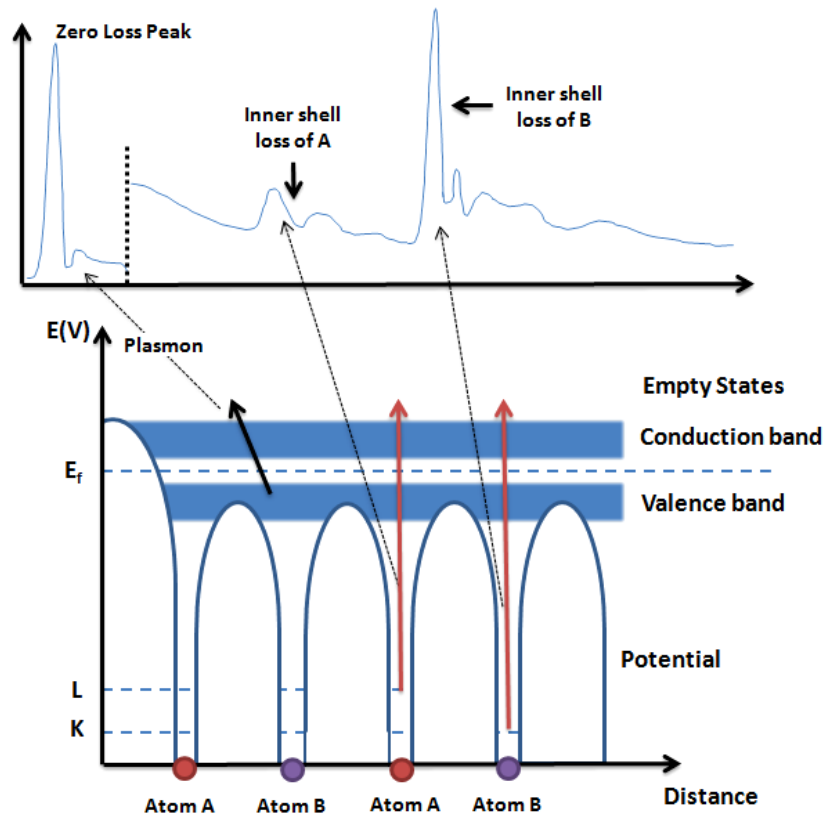


Figure 2.7: Schematic illustration of an energy-loss spectrum and examples of how main energy loss peaks are created.

As the primary focus of this thesis is on the analysis of the oxidation effects of Zircaloy-4, it is imperative that the interatomic transitions are well understood, so that the resultant energy spectra can be interpreted correctly. These chemical fingerprints provide a wealth of information about the sample, including low loss information regarding plasmonic interactions, and high loss information which relates to the movement of electrons between the inner shell electrons within the atoms of our samples.

2.3.2 The Angle of Scattering

As shown in Fig. 2.8, when an electron encounters a single atom, it is scattered through an angle θ , into some solid angle Ω . The characteristics of the scattering event are largely dependent on the incident electron energy and the atomic weight of the scattered atom. If we compound the problem by taking into account that our sample is

not only one atom thick, we must consider other factors such as thickness, density, crystallinity and how the specimen is oriented to the incident beam.

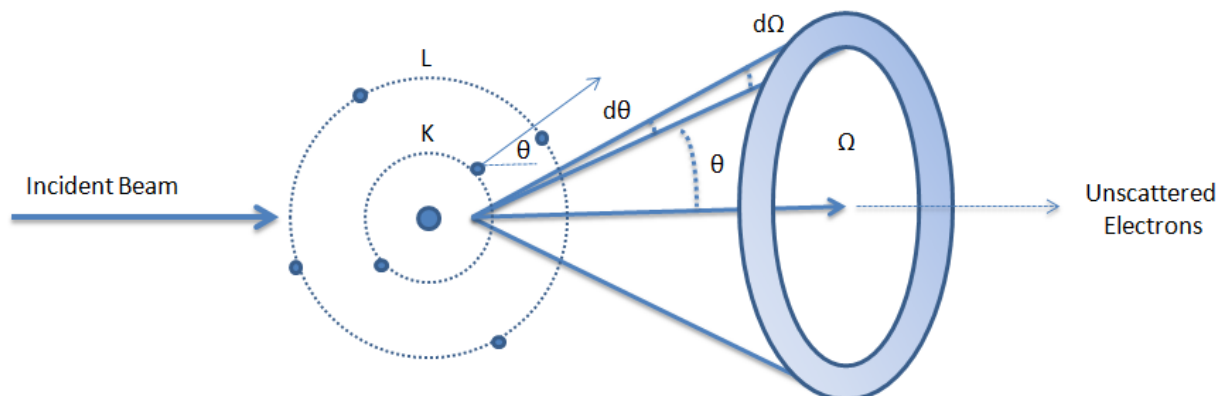


Figure 2.8: Electron scattering from a single atom. Electrons are scattered through an angle of θ . The total solid angle of scattering is Ω . A small increase in scattering angle $d\theta$ results in a small increase in solid angle $d\Omega$. Adapted from [96].

2.3.3 The Interaction Cross Section

The cross section (σ) quantifies the intrinsic likelihood of a scattering event occurring when an incident electron strikes an atom within our sample material. It has units of area. Each possible interaction has a different cross section, which is dependent on the energy of the electron beam. The cross section is proportional to the probability that an interaction will occur. Therefore, for EELS edges, the intensity of the edge I , is equal to the intensity of the zero loss peak I_0 , multiplied by the number of atoms per unit volume, and the scattering cross section, σ [97];

$$I = I_0 N \sigma . \quad (2.4)$$

2.3.4 The Error on the Cross Section

Digital Micrograph (DM) quotes a cross sectional error of 25% for an M edge, 10% for an L edge and 5% for a K edge. This is due to the fact that in general, the K edge cross section can be calculated accurately from hydrogenic calculations. The L shell

however, contains more quantum effects, and as there is more splitting of sub shells, this calculation is not so simple, and a 10% error is quoted. The M shell is more complicated again as the cross section error is calculated by the number of electrons involved, and so is quoted as 25%. These are most likely fixed systematic errors and the analysis of the accuracy of these calculations is included in Egerton [98]. Errors in this work were originally calculated on this basis, however, it should be noted that for two neighbouring elements with the same edge, the error in the absolute cross section will be similar in magnitude and direction in most cases [98], causing the systematic errors to mostly cancel each other out.

Random statistical errors were also analysed according to Poisson statistics. However, due to our setup, where hundreds or thousands of spectra are collected for every SPP, the statistics are so good that the fractional random error $1/\sqrt{N}$ is negligible. So, it is concluded that the primary component of the error arises from the uncertainty in stages performed during the data analysis which will be detailed fully in Chapter 3 of this thesis. In order to calculate this, the width, and onset energy of the background and signal windows were altered slightly several times, in order to determine the average difference in the cross sections due to several window alterations. An average error of better than 5 at. % was found in all cases, and is quoted as the general error of all elemental quantifications.

2.3.5 Mean Free Path for inelastic scattering

The mean free path (λ_{mfp}) is the average distance that the electron travels between scattering events [94]. This distance is significant as if it is known, one can deduce how thin their specimen needs to be in order to minimise the effects of plural scattering (described in section 2.3.6).

As an approximation to first order we regard molecules as hard spheres and can relate the mean free path, λ_{mfp} , to N , the number of atoms per unit volume and σ , the interaction cross section;

$$\frac{1}{\lambda_{mfp}} = N\sigma \quad (2.5)$$

2.3.6 Plural and Multiple Scattering

Plural or multiple scattering is when the electron is scattered more than once. Generally, the more scattering events, the greater the angle of scattering will be. Plural scattering becomes a problem when specimens are not sufficiently thin ($t/\lambda > 0.5$). This can cause individual peaks to not be visible or discernible in the spectrum due to multiple inner- and outer-shell processes combining to produce a Landau distribution [93]. This results in the creation of an energy loss peak which is a convolution of a single scattering distribution and the low loss spectrum. Being able to align the zero loss peak precisely to zero, one can perform a fourier-log, or fourier-ratio deconvolution of the data, to get out the single scattering distribution of interest [93]. In this work, quantitative mapping of the core-loss data was performed using a spectrum fitting approach, which explicitly accounts for multiple scattering [99], in a similar manner to earlier work [100-105]. Full details of the EELS quantification process is provided in Chapter 3, section 3.6 of this thesis. In practice, quantification of data concentrated on the relative concentrations of Zr and O across the interface and was performed using the Zr-M_{4,5} and O-K edges as described in Chapter 4. Calculated partial cross sections for these edges were used. It was unnecessary to correct the data in any way and the outer oxide was quantified as ZrO₂, as expected.

2.4 The Transmission Electron Microscope (TEM)

The push to achieve super-resolution microscopy has not in itself been a surprise, due to the fact that increasing the capability of observational instruments has, for many centuries, been one of the main drivers of science and technology. The invention of the compound optical microscope by Hans and Zacharias Janssen in 1590 and the resulting enhancements by Robert Hooke, Anthony van Leeuwenhoek and Ernst Karl Abbe revolutionised all aspects of science, especially biology, when it became possible to visualise microscopic single-celled organisms such as bacteria. These microscopes were composed of two lens systems, an objective and an ocular (eye piece) where the maximum useful magnification of the compound microscope was about 1000 x.

In comparison, a Transmission Electron Microscope allows one to image to the sub angstrom level. This milestone has been achieved by carefully balancing three basic defects inherent in electromagnetic lenses: Chromatic Aberration, Spherical Aberration and Astigmatism.

There are two imaging set ups used to perform nanoscale analysis of materials in this thesis: transmission electron microscopy (TEM) and scanning transmission electron microscopy (STEM), the schematic of both can be seen in Fig. 2.9. In this discussion, we will look at each of the key components of the transmission electron microscope (Fig. 2.9a) from the top down, beginning with the emission source, followed by the condenser system, the specimen chamber, the objective system, the projector system and concluding with a discussion of the recording devices utilised to record the data presented within this thesis. Later, the scanning transmission electron microscope will be discussed (Fig. 2.9b).

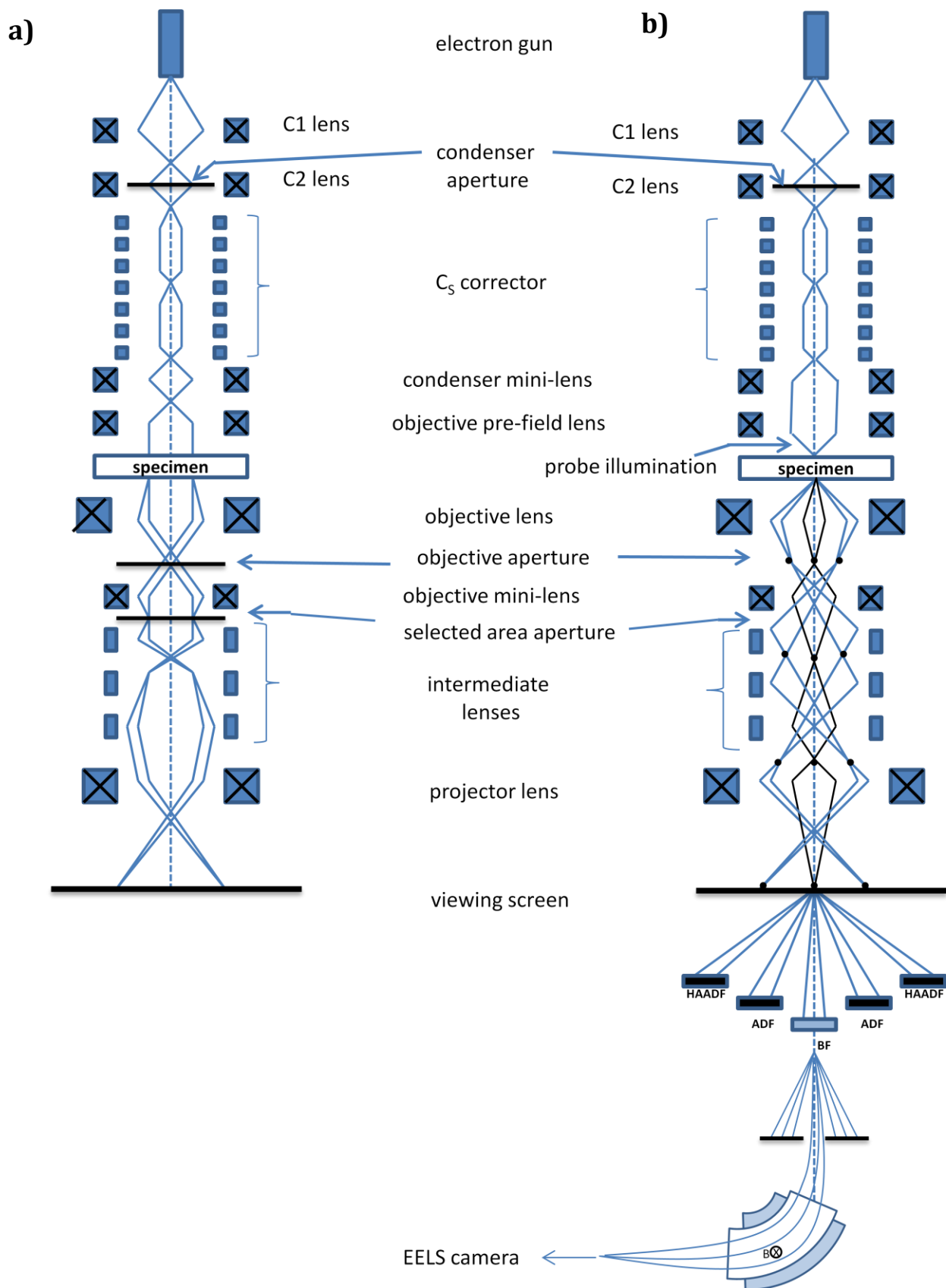


Figure 2.9: a) Top down schematic of a Transmission Electron Microscope (TEM) showing the condenser, objective and projector system, and the path in which electrons take from the gun to the viewing screen and b) Schematic of a scanning transmission electron microscope (STEM) indicating the path electrons take through the column, and into the magnetic prism for EELS analysis.

2.4.1 The Emission Source

There are two conventional methods used in order to achieve an intense beam of high energy electrons in a modern TEM: the thermionic emitter (Fig. 2.10) and the cold field emission gun (cold FEG) (Fig. 2.11).

a) Thermionic Emission

This type of gun, as the name suggests, produces electrons when heated and is used on our Tecnai T20 microscope. It operates by heating a tungsten hairpin filament or LaB₆ crystal to a temperature so that electrons are imparted with enough energy to overcome the work function of the material, ϕ (which has a value of a few eV). Thermionic currents can be increased by decreasing the work function which is often achieved by applying various oxide coatings to the wire. The process of thermionic emission can be described by Richardson's Law which relates the current density of the source, J , to the operating temperature T , in Kelvin;

$$J = AT^2 e^{\frac{-\phi}{kT}}, \quad (2.6)$$

where k is Boltzmann's constant and A is Richardson's constant.

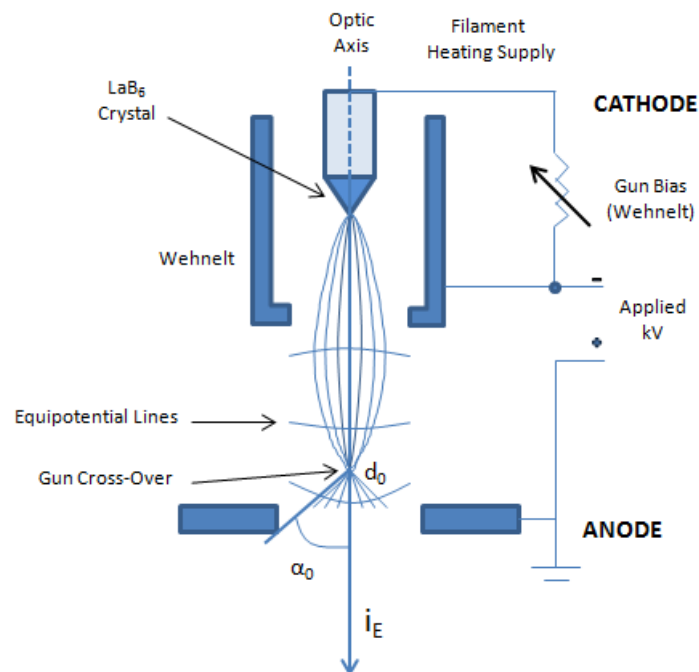


Figure 2.10: Schematic of a thermionic electron emission gun [92].

The electrons are extracted from the heated LaB₆ crystal by applying a voltage between the anode and the cathode, as can be seen in Fig. 2.10. The Wehnelt cup is held at a different potential of around 2-3 kV to focus the electrons to a crossover between the electrodes.

As the source has to be heated to a temperature $T >$ work function of the material, there is an innate problem in that when most materials are provided with a few eV of thermal energy, they either melt or vaporise. Thus, the only viable thermionic sources available are either refractory materials or those with an exceptionally low work function. LaB₆ sources have the advantage of the latter, which is why they are used commercially in modern TEMs today.

b) Cold Field Emission

A cold field emission gun (cold FEG) (as can be seen in Fig. 2.11) is operated by applying a high electric field between a sharp tip (made of tungsten) and another electrode. This tip locally enhances the electric field to the point at which electrons tunnel out. The strength of an electric field E is considerably increased at sharp points because, if we have a voltage, V , applied to a spherical point of radius r , then;

$$E = \frac{V}{r} . \quad (2.7)$$

Tungsten single crystals are used in this type of gun as they can easily be made to form a tip of $< 0.1 \mu\text{m}$. As in thermionic emission, where the source is degraded by high temperatures, applying such high fields to this sharp tip imposes a severe stress on the material, meaning that the material must be mechanically strong to remain intact.

This is of particular importance as it is a cold FEG which is the emission source on our ARM 200F STEM, which is used for analysis of all samples within this work. This gun provides a narrow beam with which to work, which is extremely useful for distinguishing features in energy loss near edge structures (ELNES) when studying electron energy loss spectroscopy (EELS).

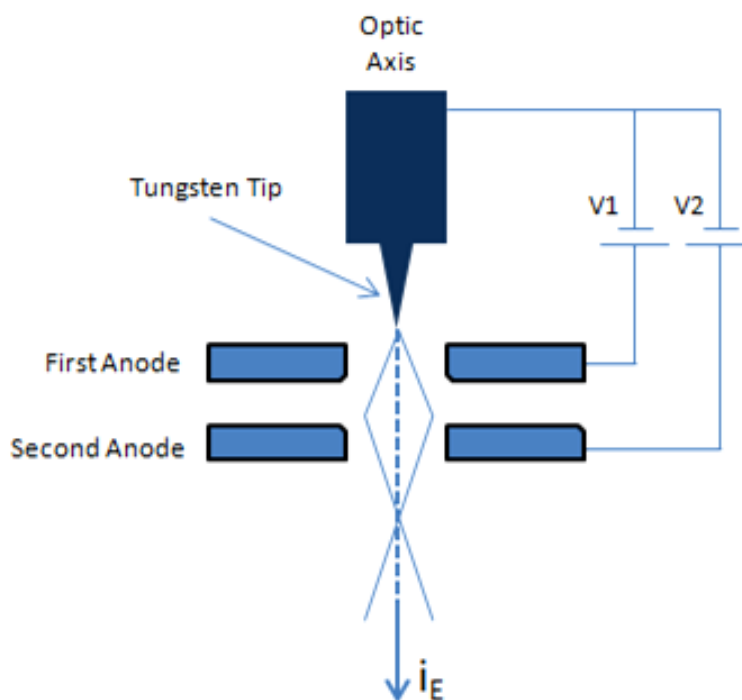


Figure 2.11: Schematic of a cold FEG electron emission gun, where i_E is the incident electron beam.

2.4.2 The Magnetic Lens

In a TEM, electron lenses are used to focus our electrons to a thin beam. Electron lenses are the magnetic equivalent of the glass lenses in an optical microscope and to a large extent, we can draw comparisons between the two. A strong magnetic field is generated by passing a current through a set of copper windings. Surrounding these coils is a shroud made of a metal. The electron moves through the centre hole in this solenoid. The electron path is further constricted by a brass lining inside this space known as the pole piece. The pole piece has a small gap within it at which point the beam is most influenced by the electromagnetic current. This is appropriately referred to as the pole piece gap. This field acts as a convex lens, bringing off axis rays back to focus. The focusing effect of a magnetic lens therefore increases with the magnetic field B , which can be controlled via the current flowing through the coils.

It should be noted that electron paths are usually (as in this thesis) represented by straight lines running through a convex lens. More accurately, however, the electron paths form a tight spiral as they are accelerated through the lenses. The path and trajectory taken by the electrons are influenced by the lens current as they pass through a small opening in the lens.

2.4.3 The Condenser System

The condenser system is used to control the illumination of the sample, where the gun crossover acts as an object for the illumination system. This system consists of two condenser lenses, C1 and C2. Specifically, the strength of the C1 lens controls the position of the C1 crossover, which directly affects the size of the probe that can be formed by the C2 lens. There are also two sets of shift-and-tilt coils aligned above the C1 lens and below the C2 lens (Fig. 2.12).

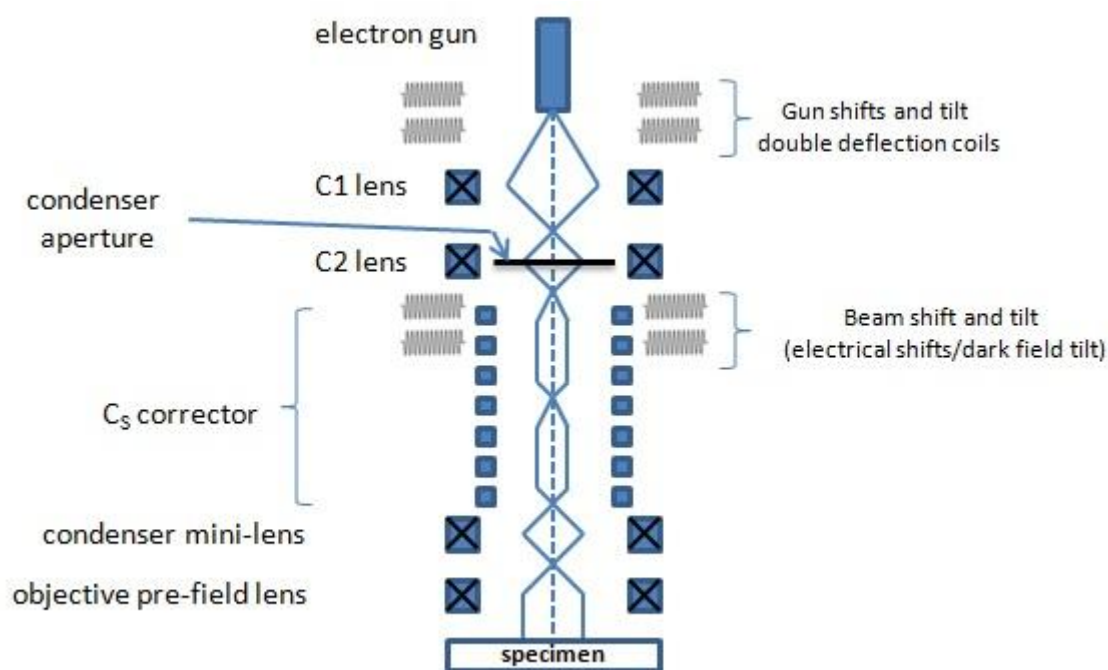


Figure 2.12: The condenser system in a Transmission Electron Microscope.

The topmost set of shift and tilt coils aligns the gun with the first condenser lens, C1. The bottom set of shift and tilt coils align whatever comes out C2 with specimen plane and the rest of the electron microscope. Specifically, the C1 lens demagnifies the crossover of the electron beam emitted from the electron gun to $\sim 1/10$ in size. In the case of a thermionic source, the original crossover may be several tens of μm across, whereas in a FEG, the source size may be less than the desired illumination area on the specimen, meaning that the crossover may need to be magnified. The C2 lens then transfers the demagnified beam onto the object plane of the objective lens.

Fig. 2.12 shows the microscope set up in traditional TEM mode. This parallel illumination is essential to get the sharpest selected-area diffraction patterns and, in principle, the optimal image contrast.

2.4.4 Specimen

A TEM stage is required to have the ability to hold a specimen and be manipulated to bring the region of interest into the path of the electron beam. As the TEM can operate over a wide range of magnifications, the stage must simultaneously be highly resistant to mechanical drift, with drift requirements as low as a few nm/minute while being able to move several $\mu\text{m}/\text{minute}$, with repositioning accuracy on the order of nanometres. Earlier designs of TEM accomplished this with a complex set of mechanical down gearing devices, allowing the operator to finely control the motion of the stage by several rotating rods. Modern devices may use electrical stage designs, using screw gearing in concert with stepper motors, providing the operator with a computer-based stage input, such as a joystick or trackball.

TEM specimen stage designs include airlocks to allow for insertion of the specimen holder into the vacuum with minimal increase in pressure in other areas of the microscope. The specimen holders are adapted to hold a standard size of grid upon which the sample is placed or a standard size of self-supporting specimen. Usual grid materials are copper, molybdenum, gold or platinum. This grid is placed into the sample holder, which is paired with the specimen stage. A wide variety of designs of stages and holders exist, depending upon the type of experiment being performed. Once inserted into a TEM, the sample often has to be manipulated to present the region of interest to the beam, such as in single grain diffraction, in a specific orientation. To accommodate this, the TEM stage includes mechanisms for the translation of the sample in the XY plane of the sample, for Z height adjustment of the sample holder, and usually for at least one rotation degree of freedom for the sample. Thus, a TEM stage may provide four degrees of freedom for the motion of the specimen. Most modern TEMs provide the ability for two orthogonal rotation angles of movement with specialized holder designs called double-tilt sample holders.

Two main designs for stages in a TEM exist: the side-entry and top entry version [22]. Each design must accommodate the matching holder to allow for specimen insertion without either damaging delicate TEM optics or allowing gas into TEM systems under vacuum.

2.4.5 The Objective System

The objective lens forms a magnified image of the specimen. Once electrons scatter through the sample, rays which have left the object in the same direction are brought to a focus in the back focal plane of the objective lens. This produces diffraction spots that have fixed phase relationships, as shown in Fig. 2.13a. If, instead, an image is required, the intermediate lenses must be adjusted in order that the object plane is the image plane of the objective lens. Then, an image is projected onto the viewing screen/CCD, as shown in Fig. 2.13b.

It should be noted that Fig. 2.13 is an over simplification of a very complex system. In reality, there are many more lenses in a TEM column utilised to operate in these two modes. This, in turn, gives more flexibility in terms of magnification and focussing range than what is demonstrated in Fig. 2.13.

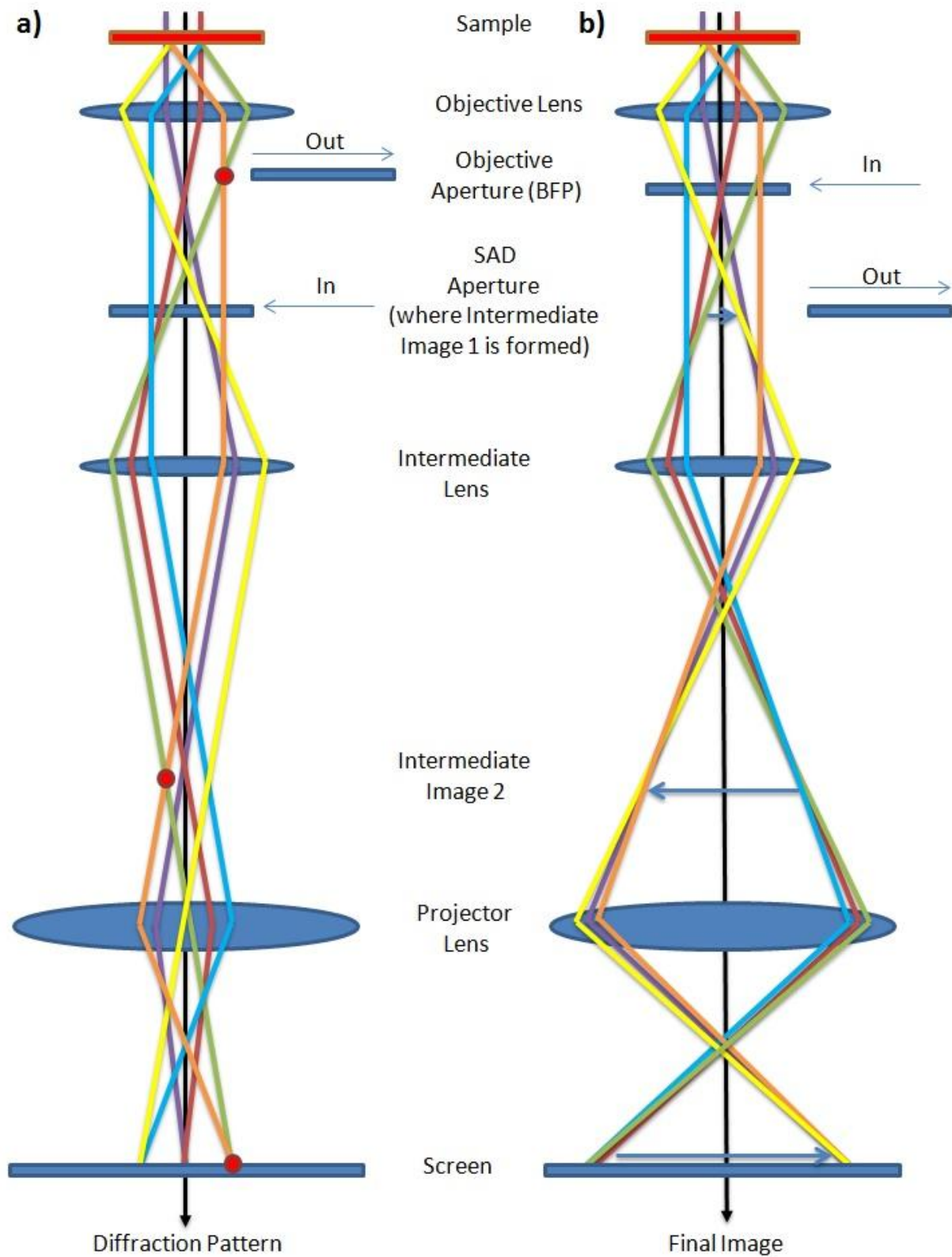


Figure 2.13: The two basic operations of the TEM imaging system where a) diffraction mode: the DP is projected onto the viewing screen and b) imaging mode: where the image is projected onto the screen.

2.5 Imaging Methods in the TEM

2.5.1 Selected Area Diffraction (SAD)

Selected area diffraction (SAD) is a TEM technique to obtain diffraction patterns that result from the electron beam being scattered by the specimen. Obeying Bragg's law, the electrons are scattered elastically by the atoms within the sample, and therefore, we can index the diffraction spots in the pattern, identify the phases in the sample and study their structures. Fig. 2.13a, shows how a selected area diffraction pattern (SADP) is achieved, where each diffraction spot will correspond to a satisfied diffraction condition of the sample's crystal structure. However, it should be noted that in the configuration shown in Fig. 2.13a, electrons from the whole area of the sections of the sample illuminated by the beam contribute to the diffraction pattern (DP). Experimentally, this is not ideal, as the high intensity of the beam can damage the viewing screen, or saturate the CCD camera. To overcome this problem, one can decrease the beam size, or insert an aperture above the specimen that only permits electrons that pass through it to hit the specimen.

In order to decrease the beam size, one can make use of the condenser lenses further up in the column, to converge the beam at the specimen: this is the basis behind convergent beam electron diffraction (CBED) imaging. Alternatively, one can put selected area aperture in a conjugate plane with the specimen (i.e. in one of the image planes of the objective lens as can be seen in Fig. 2.13), in order to create a virtual aperture at the plane of the specimen, and only allow selected electrons to contribute to the final diffraction pattern.

2.5.2 Bright-Field Imaging

In order to obtain contrast in an image in the TEM, there must be scattering that leads to an intensity variation. Diffraction contrast is the most common form and the objective aperture is used to restrict diffracted electrons from forming the image, as can be seen in Fig. 2.14. This aperture is placed in the back focal plane of the objective lens and only the transmitted beam is permitted to travel down the microscope column, with the diffracted beams being cut off by the objective aperture. The electron intensity present in the back focal plane of the objective lens goes on to form the image. This information can be used to discuss crystallographic information about the specimen.

For single crystal or amorphous materials spot patterns are formed. If the material is polycrystalline, ring patterns are obtained under Fraunhofer conditions i.e. parallel illumination of the sample.

The resulting diffraction pattern can then be used to perform bright field imaging of the specimen. This diffraction pattern comprises a bright central spot, which contains the direct beam of electrons, (alongside some scattered electrons). Specifically, in this imaging mode, the straight through beam of electrons is selected by the objective aperture to go on and create the final image, as seen in Fig. 2.14(b).

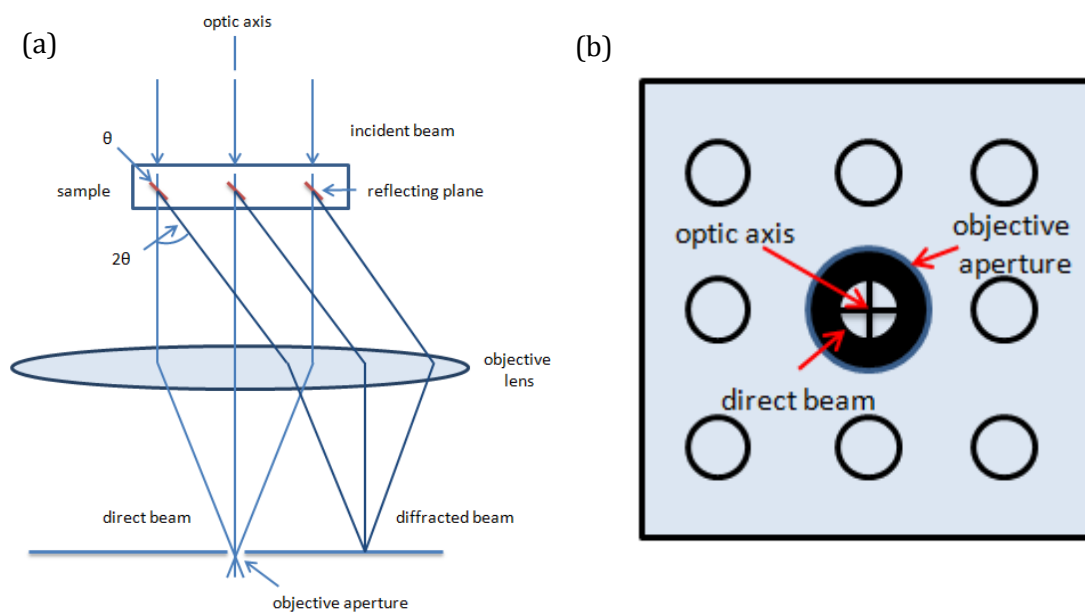


Figure 2.14: Bright field (a) ray diagram, with (b) objective aperture accepting direct beam for bright field imaging. Adapted from [94].

2.5.3 The Projector System

In order to switch between image and diffraction modes in the TEM, we can adjust the strength of the lower column lenses – the projector lenses. This projector lens system acts to project a further magnified image of that produced by the objective lens and altering the magnification of the TEM results in a change of strength of these lenses, as can be seen in Fig. 2.13.

2.6 Imaging Solutions for Transmission Electron Microscopy

2.6.1 Charge-Coupled Device (CCD)

Since the late 1980s, charge-coupled devices have been used to directly readout the wide range of signals accessible in transmission electron microscopes [106-109]. CCD systems have enabled the immediate access to images on a computer within seconds of recording, and have significantly increased efficiency and throughput in the electron microscopy field. CCD systems surpass previous conventional recording methods such as photographic film in many major aspects, including sensitivity, linearity and dynamic range [98]. They are able to indirectly detect electron images without degrading their resolution or adding a large amount of noise and have been one of the most prevalent improvements made in the past few decades, which has revolutionised electron microscopy.

In general, CCDs have the ability to accumulate charge, proportional to the number of incident quanta, during an integration period. The readout involves transfer of the accumulated charge packets in each cell first to a shielded storage region and then to a readout register. In depth details of the operation of a CCD system can be read in more detail in a study by Krivanek *et al.* [97]. Ultimately, this development now allows one to obtain gigabytes of data in a relatively short time frame. This has been particularly important for this project, as we wish to not only acquire BF and DF images of many samples in CTEM, but also to obtain high- and low-loss spectrum images in the STEM, in order to probe the nanoscale details of the samples.

2.7 Improving the Transmission Electron Microscope

In spite of the best efforts of lens designers, standard lenses in electron microscopes are far from perfect. Ever since the fundamental work of Scherzer [99], it has been known that the resolution of standard electron microscopes using only round lenses is limited by unavoidable spherical and chromatic aberration effects. Although proposals to correct these aberrations were made as early as 1947, the realisation of aberration correction was not achieved for another 50 years. Among the first people to show that spherical aberration could be overcome using an objective corrector was Maximilian Haider [100] and since then, extensive research on correcting spherical aberration in 200kV transmission electron microscopes has been performed by Haider and Harald

Rose [101], involving two electromagnetic hexapoles and four additional lenses. Later, Krivanek *et al.* [102] improved this further, with the addition of a condenser corrector. In the last few decades, the performance of the TEM has slowly but steadily improved, with the resolution limit decreasing from 1 nm to better than 0.2 nm – a length scale which is incredibly beneficial for microscopists, as many interatomic distances lie in the region of 0.2 nm. Specifically, the FEI Technai T20 and JEOL ARM 200F used in this work can achieve ~ 0.15 nm and sub 0.1 nm respectively. The principle by which aberration correction is achieved is based on the fact that the second order primary aberrations which are created from the first hexapole element are about to be mitigated due to the second hexapole element. However, the two hexapoles then also create a secondary third-order rotationally symmetric spherical aberration which is proportional to the hexapole strength squared [110].

2.7.1 Spherical Aberration

Spherical aberration occurs when the lens field behaves differently for off-axis rays than it does for those on axis (as seen in Fig. 2.15). Thus, the further off axis an electron is, the more strongly it is bent back towards the axis [92]. This results in being unable to form a sharp spot, where the best possible outcome is a disc of least confusion as shown in Fig. 2.15, where there is a compromise between the focal point for paraxial and non-paraxial rays. This in turn, limits the size of the focused spot that can be achieved. Compensating for spherical aberrations within the electron microscope is achievable as the coefficient of spherical aberration is of the opposite sign to that of the objective lens. This means that the spherical aberration of the complete system can be compensated for by exciting the hexapoles appropriately [111].

Spherical aberrations are most important in the objective lens as this degrades any detail that we can resolve in TEM images as all other lenses will further magnify any error introduced in the objective system.

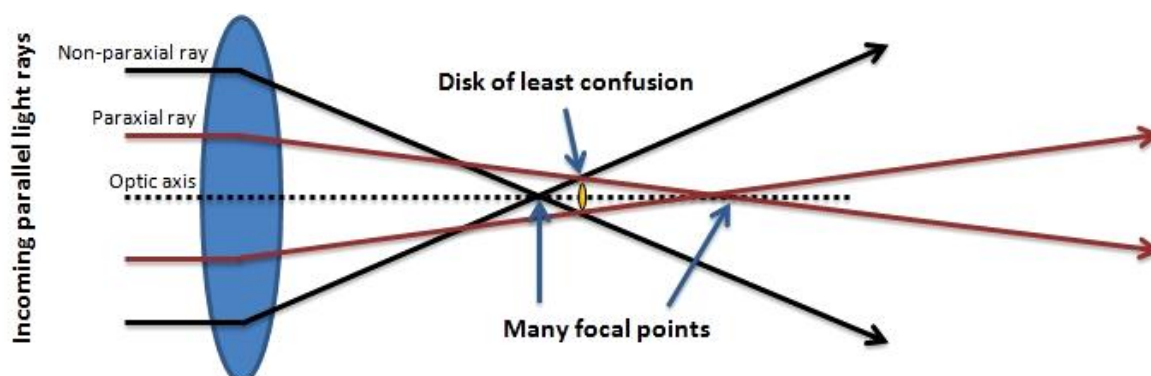


Figure 2.15: Spherical aberration in a lens showing how paraxial rays are refracted less than non-paraxial rays, resulting in multiple focal points.

2.7.2 Chromatic Aberration

Chromatic aberration is related to the energy of the electrons and describes the fact that electrons of different energies have different focal points in an electron lens. Specifically, electrons of lower energy are focussed more strongly than those of a higher energy. This has a large impact on the achievable resolution of the instrument and its effects are shown in Fig. 2.16

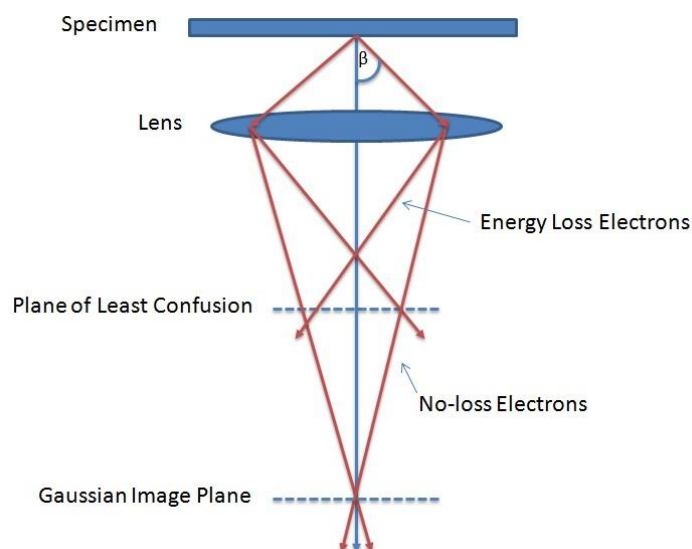


Figure 2.16: Chromatic aberration resulting in electrons with a range of energies being focussed in different planes (adapted from [92]).

Chromatic aberration can be reduced by using a source which has a low energy spread such as a cold FEG (~ 0.3 eV).

2.7.3 Astigmatism

Due to the imperfections in the symmetry in the polepieces, electrons travelling down the column sense a non-uniform magnetic field as they spiral round the optic axis. These local variations in the magnetic field strength result in image distortion. Furthermore, if the apertures are not clean, the contamination can deflect the beam. These effects contribute to astigmatism. Bad or "gross" astigmatism can be seen as "streaking" in the image in an X direction that changes to the Y direction as the image passes through focus from under focus to over focus. At exact focus the streaking vanishes and focus can be correctly achieved if the spot size is suitable.

2.8 Scanning Transmission Electron Microscopy (STEM)

The majority of materials characterisation within this project was done on a JEOL ARM200F STEM and so the detailed description of the microscope column will be limited to this model. One of the principal advantages of STEM over TEM is that STEM can make use of other signals which cannot be spatially correlated in the TEM such as secondary electrons, scattered beam electrons, characteristic x-rays and electron energy loss, which will be discussed in full detail in Chapter 3. A schematic of a scanning transmission electron microscope (STEM) set up can be viewed in Fig. 2.9b.

2.8.1 STEM Bright Field

STEM image formation in scanning mode is fundamentally different from static-beam TEM image formation. In TEM, we take a selected section of the electrons exiting the sample, and we project these onto a screen. However, STEM involves scanning a very finely focussed beam of electrons (as can be seen in Fig. 2.9b) across our thin sample in a raster pattern. This is done by adjusting the scan coils and results in images being acquired much slower than in TEM mode as STEM imaging involves serial recording as opposed to parallel recording as in a TEM.

In STEM, the transmitted electrons are collected using annular detectors. The detection system comprises three solid state detectors: the bright field (BF), annular dark field (ADF), and the high angle annular dark field detector (HAADF). In bright field mode, only electrons which we wish to contribute to our final image, hit our BF detector which is placed in the centre of the beam direction.

2.8.2 STEM annular dark field (ADF) and high angle annular dark field (HAADF)

The contrast mechanisms in STEM dark field imaging is different from conventional dark field imaging as STEM mode is configured so that the optics distinguishing between dark and bright field modes is positioned after the converged beam has interacted with the specimen.

As opposed to bright field imaging, electrons which have been scattered by small angles are collected by the ADF detector. Similarly, very high angle, incoherently scattered electrons (as opposed to Bragg scattered electrons) can be detected by the

HAADF detector. This detection is highly sensitive to variations in the number of atoms in the sample, and so, the main source of contrast in the STEM results from Z-contrast.

When performing electron energy loss spectroscopy (EELS) analysis, the BF detector is retracted in order to let the direct beam travel through the spectrometer, resulting in only the ADF or HAADF detectors being used to acquire EELS data.

Electron scattering, specifically the physics behind the angle of scattering and issues surrounding plural scattering were discussed previously in this Chapter. Now, a discussion is given on the instrumentation of a scanning transmission electron microscope which subtends a fraction of this scattering.

2.9 The Energy Loss Spectrometer

In order to analyse the energy loss due to interaction of electrons with atoms in the specimen, a spectrometer is required. Post sample interaction, the electrons which have lost energy pass through dozens of focussing lenses within the spectrometer, to a magnetic prism spectrometer. This is the key component within the spectrometer as it disperses electrons according to their energies. Electrons travelling at to speed v in the z -direction are directed in between poles of an electromagnet which has a magnetic field B pointing perpendicular to the direction of the beam, in the y -direction. This causes the electrons to travel in a circular orbit within this field, with a radius of curvature R given by;

$$R = \frac{(\gamma m_0)}{eB} v, \quad (2.8)$$

where $\gamma = 1 - (1 - v^2/c^2)^{1/2}$ and m_0 is the rest mass of the electron [93]. This deflects the electron beam by around 90° . As we can see from equation above, the velocity of each individual electron within the magnetic field will be deflected to slightly different paths, due to the dependence on the velocity v of each individual electron. A smaller velocity v , results in a smaller radius of curvature R , therefore, these electrons will depart from the magnet with a slightly larger deflection angle than those which have not lost as much energy during the interaction. This can be seen in Fig. 2.17.

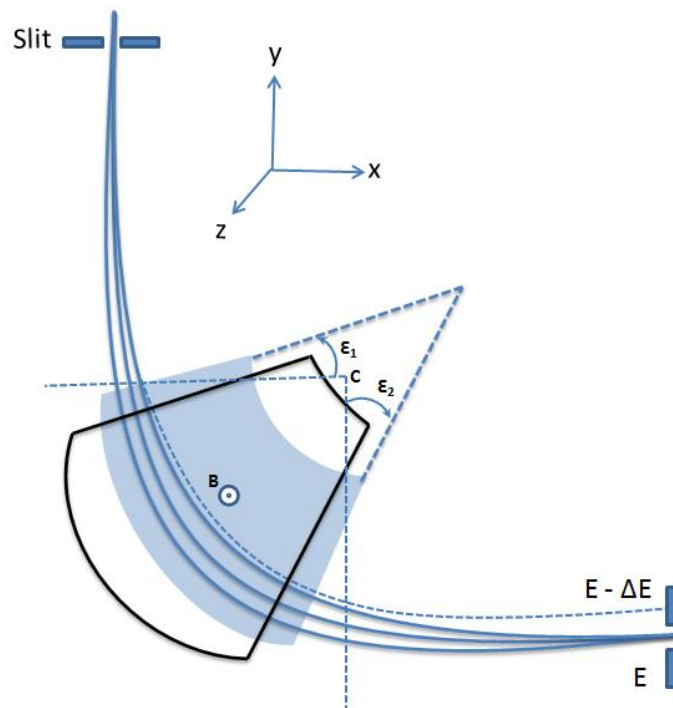


Figure 2.17: The EELS spectrometer, showing how the incoming electrons are deflected according to their energies, resulting in an Electron Energy Loss Spectrum. Adapted from [93].

A comprehensive description of how to acquire and interpret an optimally acquired electron energy loss spectrum is given in Chapter 3.

2.10 Employing De-Scan in the STEM

When employing EELS in STEM mode, the microscope is in image-coupling mode. This results (as usual) in the diffraction pattern and the image being located in two different locations: the diffraction pattern at the EELS entrance aperture, and the image located at the plane of the differential pumping aperture. Thus, any movement of the beam during scanning results in the EEL spectrum to drift across the EELS detector. As the absolute position of the spectrum is important, special measures must be taken in order to compensate from this shift both sideways and in energy. To avoid such an undesirable electron-beam position or angle to the STEM or EELS detector, a two-stage deflector coil in the image-forming lens system is operated synchronously with the beam scan to always bring back the electron beam to the centre of the detector and/or parallel to the optical axis, as seen in Fig. 2.18.

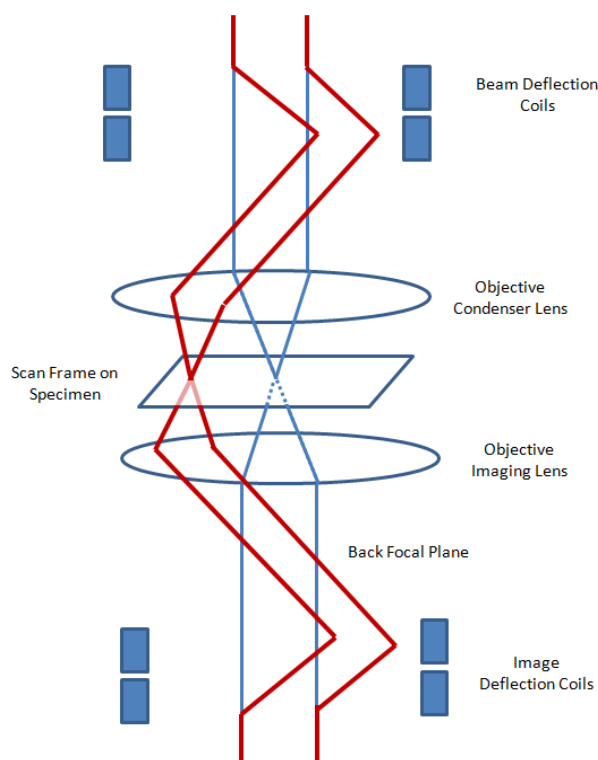


Figure 2.18: De-scan compensates for the movement of the beam on the specimen during STEM mode, allowing the image of the beam to remain stationary below the image deflection coils and thus in the differential pumping aperture and on the EELS detector.

In summary, coupled STEM imaging and EELS is an optimal set up for providing a comprehensive study of the oxidation of Zircaloy-4 during corrosion in superheated water. The superior resolution gained from using a cold FEG alongside the implementation of aberration correction in the lenses allows for detailed pixel by pixel mapping of the metal:oxide interface, precipitates and the oxide scale.

Simultaneously capturing multiple signals with high spatial resolution makes the STEM spectrum-imaging (STEM-SI) technique (discussed in detail in Chapter 3) an extremely powerful tool for the characterisation of material systems. Moreover, the acquisition of the EELS signal allows the user to probe in fine detail, the chemical, compositional, electronic and physical properties of such materials. As such, EELS is extremely well-suited to the analysis of the chemistry of Zr:ZrO₂ interfaces, for probing the morphology of secondary phase precipitates, and mapping oxygen content across specimens. Recent powerful improvements in the collection of the EELS spectrum, as detailed later in Chapter 3, have been great and such advancements have really been the

catalyst to allow for a detailed study of the nanoscale mechanisms of corrosion of Zircaloy, as is presented within this thesis.

“Give me a lever long enough and a fulcrum on which to place it and I shall move the world”.

— Archimedes

chapter

3

Electron Energy Loss Spectroscopy (EELS)

Electron energy loss spectroscopy (EELS) is the analysis of the distribution in energy of initially monoenergetic electrons which have travelled through a sufficiently thin (<100 nm) specimen. All interactions take place inside the specimen and information about its internal structure can be obtained by passing the transmitted beam into a spectrometer. These energy loss events can tell us a huge amount of detail about the sample, from something as straight forward as the thickness of the sample, down to details such as electronic structure, chemical bonding and valence state. Typically the electrons can be grouped into two upon exit of the specimen - those which have lost no energy in the event, and those which have undergone scattering and enter the spectrometer with energies less than that of the incident electron beam. Unscattered and elastically scattered electrons make up the zero loss peak in the

resulting spectrum, whereas the remaining electrons have lost energy in exciting a process in the sample.

In EELS experiments, it is not possible to collect all the electrons scattered by the sample. Those limitations are mainly due to geometrical factors. As shown on Fig. 3.1, there are two important angles to consider if one wants to understand which scattered electrons have been collected in the spectrometer. In all instances within this project, dual electron energy loss spectroscopy (DualEELS) datasets were collected using a GIF Quantum ER with a probe convergence angle 29 mrad and a spectrometer acceptance angle of 36 mrad. α is called the convergence semi-angle and is determined by the microscope's settings, especially the condenser lens and aperture and β is called the collection semi-angle and is determined by the objective aperture, the spectrometer entrance aperture, the camera length and the mechanical specification of the instrument.

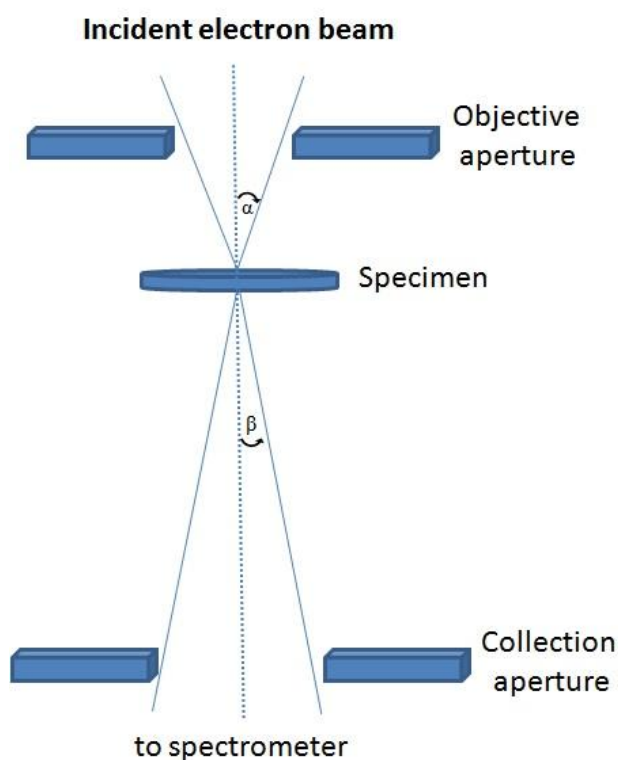


Figure 3.1: Definition of α and β in a (S)TEM showing α , the convergence semi-angle and β , the collection semi-angle.

3.1 Why do EELS?

Although EELS is a challenging technique, which requires very thin specimens and careful microscope and spectrometer alignment, it is the most sensitive technique at an

electron microscopist's disposal for the chemical analysis of specimens. With a spatial resolution of single atoms, EELS can allow for the detection of all elements within the periodic table, and is especially useful for those elements which are very light, and are often difficult to pick up using X-ray spectroscopy alone.

3.2 The Electron Energy Loss Spectrum

In a scanning transmission electron microscope (STEM), a high-energy beam of electrons is focussed on the sample, and it is this beam which stimulates the emission of characteristic x-rays from the specimen. This happens due to electron excitation and core-hole creation within the sample. When the incident beam excites an electron in an inner shell, it leaves behind an unstable core-level hole where the electron once was. An electron from an outer, higher energy shell can fill the hole with the difference in electron energy levels (i.e. $m=2$, $n=1$) being emitted as a photon in the x-ray region. The EEL spectrum which is produced due to the inelastically scattered electrons contains all the information on the electron distributions in the solid and, if the scattered electrons are dispersed according to their precise energy, they may be used to form an EEL spectrum as shown in Fig. 3.2.

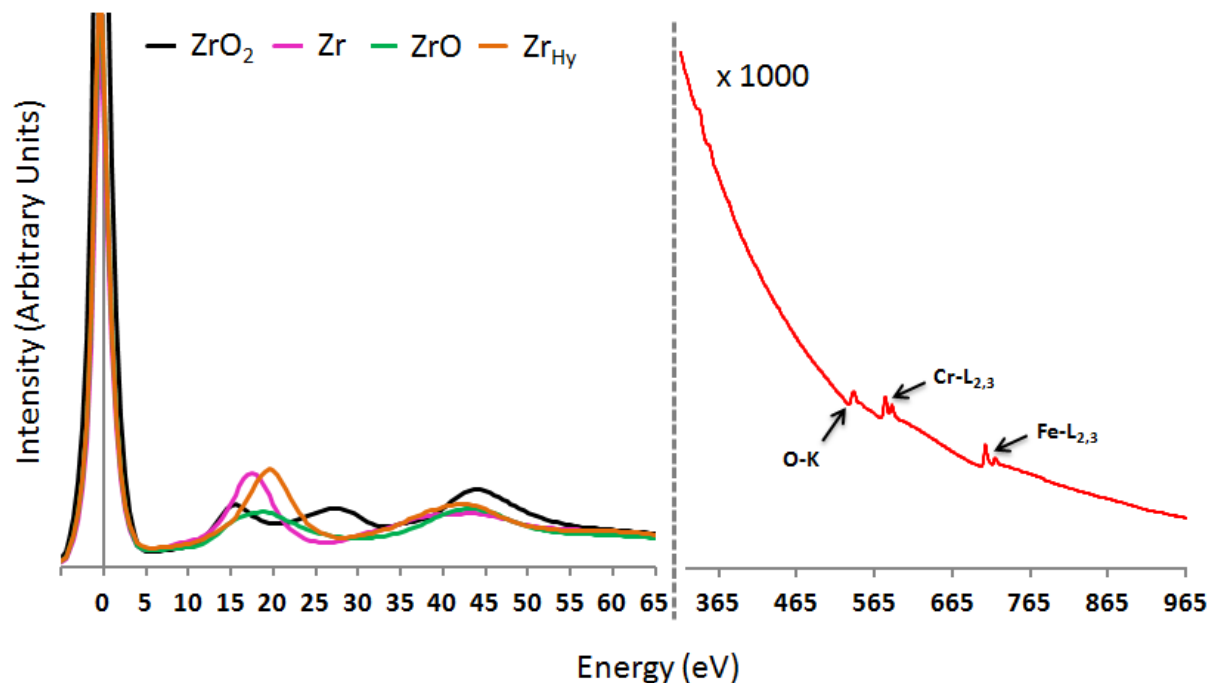


Figure 3.2: Electron energy loss spectrum of a Zircaloy-4 specimen corroded under high pressure, at 350 °C, showing low-loss profiles of phases present in the specimen, alongside a scaled profile of the high-loss ionisation edges.

In general, the low loss region depicts energies which are less than 50 eV where the dominant feature is the zero loss peak. The zero loss peak corresponds to electrons that underwent minimal, or no inelastic scattering (i.e. little to no energy loss). This can either be in the form of electrons which have been scattered elastically but which have an energy loss less than the experimental energy resolution, or as electrons which have not been scattered at all, and have passed through the material undeflected. The ZLP width mainly reflects the energy distribution of the electron source. It is typically 0.2 – 2.0 eV, but may be as narrow as 10 meV or lower in a monochromated electron source. As our Cold FEG does not suffer from thermal broadening, as in a thermally assisted Schottkey, we can achieve an energy of ~ 0.3 eV, which is typical of unmonochromated FEG sources.

The 5 - 50 eV region contains plasmon peaks, inelastic scattering events from outer-shell electrons and other minor features that are not relevant here. In the free electron gas model of a solid, plasmon excitations can be visualised as the harmonic oscillation of weakly bound conduction electrons amongst a background of fixed ionic cores. The oscillation energy can then be related to the electron gas density and effective mass of the charge carriers. This means that small alteration of the materials properties can affect these values, making the plasmon peak position a sensitive indicator of changes in a material. The plasmon energy is calculated as;

$$E_p \cong \sqrt{\frac{ne^2h^2}{\pi m}}. \quad (3.1)$$

where n = conduction/valence electron density, e = electron (hole) charge, m = electron (hole) effective mass and h = Plank's constant. The remainder of the spectrum is comprised of the core loss spectra superimposed upon a decaying background from continuum (Bremsstrahlung) scattering. Bremsstrahlung production (also known as 'breaking radiation') is caused when a transmitted electron undergoes centripetal acceleration in the nuclear field of an atom, and loses energy in the form of electromagnetic radiation. The energy spectrum of the emitted photons forms a continuous background to the characteristic peaks observed in the EELS spectrum.

The major features at energies of above 50 eV relate to characteristic core-loss absorption edges, which result from the permitted electronic excitations between the

atomic electron energy levels. At high energies, the electron intensity is seen to decrease rapidly, with these inner-shell excitation features superimposed on the smoothly decreasing background (as can be seen in Fig. 3.2).

The absorption edges will be slightly different for each and every element due to the fact that each element has a unique electron orbital configuration. Furthermore, the intensity of the absorption edge is proportional to the number of atoms present which absorb energy from the transmitted electrons. How intense these edges are, is directly proportional to the number of atoms and the scattering cross section of the considered element. Therefore, quantification of elemental abundances can be determined from the integration of the intensities under absorption edges [93]. The cross section is a function type of edge and depends strongly on the scattering angle. In EELS experiments, it is not possible to collect all the electrons scattered by the sample (due to geometrical limitations). During the quantification process, it is important to input the collection and convergence angles used during experimental proceedings as these two angles determine what scattered electrons have been collected in the spectrometer. It is crucial to have a collection angle large enough to collect a significant fraction of the scattered signal as β can have a strong influence on the quantification calculation.

Using a beam of electrons to probe a sample is advantageous over other imaging methods as not only are electron beams easy to produce, but the electrons within the beam will interact strongly with those within the sample, allowing for the production of images with strong contrast at the atomic scale.

With recorded edge data available to look to, such as the EELS edge identification slide-rule from Gatan, or the EELS Atlas [112], the energy threshold of an edge can easily be correlated with a particular element and electron shell, as the ionisation of this shell will produce the characteristic features observed in the spectrum. Furthermore, elemental maps can be acquired by forming images using only electrons that lost a narrow range of energies corresponding to characteristic absorption energies of a particular element. This ultimately allows the user to analyse materials right down to the atomic scale, and with improvements in spatial, spectral and temporal resolution continually on the increase, the opportunity for novel discoveries in materials science using (S)TEM imaging is becoming more and more possible.

3.3 EEL Spectrometers

As discussed in section 2.9, electrons lose energy due to inelastic scattering in the specimen and thus, a magnetic spectrometer can be utilised to deflect the electrons and disperse them onto a detector. By this method, modern analytical transmission electron microscopes are able to gather a large amount of information from the sample in the form of spectrum image (SI), as was first proposed by first proposed by Jeanguillaume and Colliex in 1989 [113]. Spectrum imaging is a method which generates a spatially resolved distribution of electron energy loss spectroscopy data. A typical case involves the creation of a data cube (as can be seen in Fig. 3.3) where two of the cube axes correspond to spatial information, while the third dimension is the energy loss spectrum. The resultant dataset is known as a spectrum image (or spectrum line scan for the 1D case), which you can acquire and visualise in a number of ways. This data set cube can be created either by acquiring a complete spectrum at each spatial pixel (scanning transmission electron microscope spectrum imaging (STEM SI)) or a complete 2D image collected over a narrow band of energies at a single energy slice of the data cube (energy filtered transmission electron microscope spectrum imaging (EFTEM SI)).

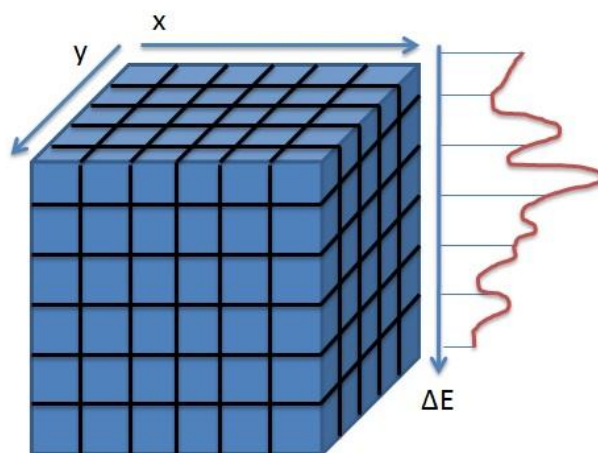


Figure 3.3: A spectrum image data cube. In STEM spectrum imaging, the STEM probe is systematically moved along the sample in x and y directions, and the resulting signals are collected. The entire spectrum is stored at each point allowing advanced spectral processing to be performed for every pixel in the spectrum image.

Having a complete spectrum at each data point allows the creation of quantitative compositional or chemical maps and profiles. The complete spectrum also enables one

to identify and correct data artifacts and understand image contrast and dataset limitations.

Since an energy resolution of better than 1 eV is required to, for example, probe slight changes in oxidation state and thus slight shifts in energy, the choice of spectrometer is limited to those types which offer high resolving power.

3.3.1 Gatan Imaging Filter (GIF) Layout

The 965 GIF Quantum ER imaging filter, as can be seen in Fig. 3.4, is coupled to our JEOL ARM 200F, and is utilised in this PhD to achieve high spatial resolution images. This imaging filter is ideally matched to our probe corrected Cold FEG STEM, as it is able to use a microsecond shutter and high-speed detector in order to take full advantage of the high beam current produced. The 2.5 mm and the 5 mm standard spectroscopy apertures of the GIF Quantum ER supports the high collection angles required for high resolution EELS analysis. Typically, in this project, EELS acquisition was done with a probe with a semiconvergence angle of 29 mrad and a post-specimen lens setup that gave a spectrometer acceptance angle of 36 ± 0.4 mrad for EELS-SI. Moreover, the 1000 spectra per second, high-speed EELS acquisition mode allowed for detail rich mapping of each EELS SI dataset.

The GIF Quantum ER has a 90° gradient sector magnet, sketched in Fig. 3.4, which bends the beam through a 7.5 cm bending radius, thereby dispersing the beam by energy. Moreover, the prism has inclined pole faces which give the prism additional first order focussing properties. The GIF Quantum also uses an electrically isolated drift tube through the magnetic prism whereby the voltage on the drift tube can be altered to produce rapid energy loss shifts of up to 1 keV. This filter combines advanced dodecapole-based electron optics and aberration correction up to the sixth order to acquire images and spectra with unprecedented exposure control and dynamic range. The poles of the dodecaipoles are individually excited in order to generate any combination of deflector, whether that is quadrupole, sextupole, octupole, decapole or dodecapole lenses, which enables extremely precise control of the optical properties of the system. Patented algorithms enable the electron optics of the system to be auto-tuned to ensure the system is running at peak performance.

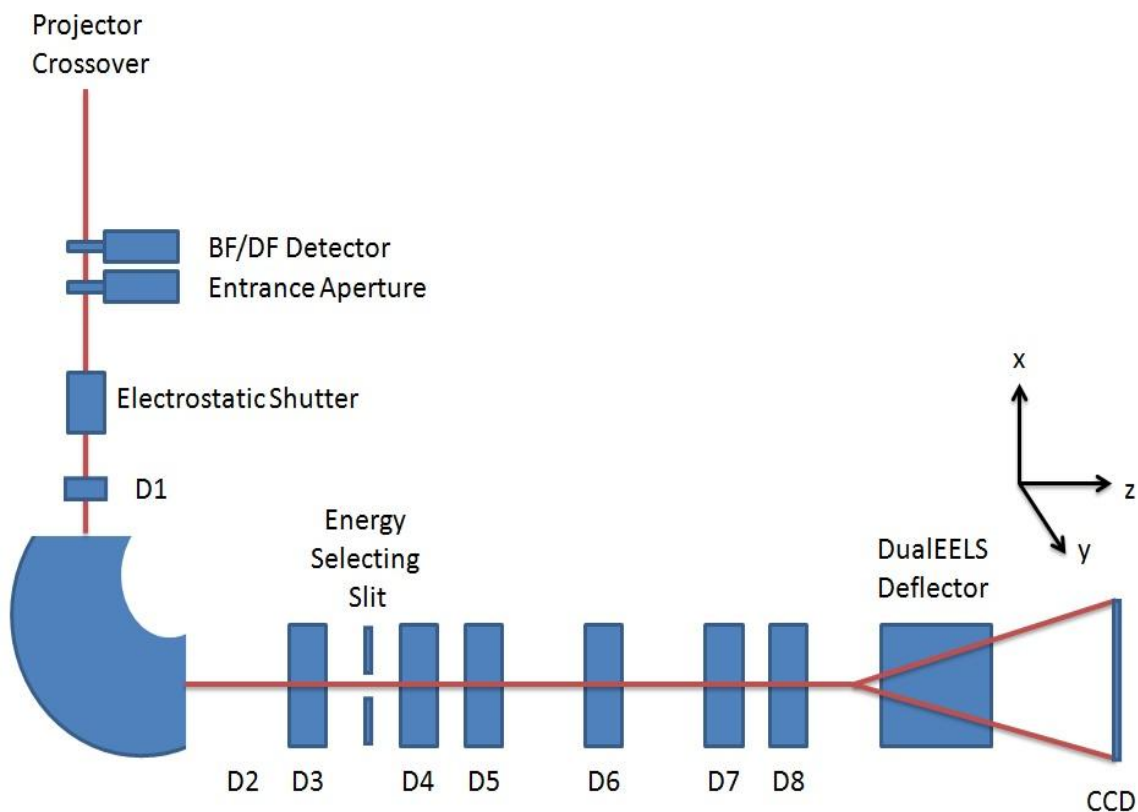


Figure 3.4: Schematic lay-out of the GIF Quantum ER spectrometer, which is ideally suited for STEM EELS acquisition and fast EFTEM mapping from a broad range of electron sources. The system has a standard 9 mm imaging aperture, a STEM detector, and an electrostatic shutter.

The GIF Quantum 965 also has an internal electrostatic shutter which provides fast beam blanking, enabling exposure times as low as 1 μ s. This allows acquisition of core-loss spectra with beam shuttering close to the frame time of the camera (e.g. 100ms), whilst the low-loss is captured using a fast beam exposure (e.g. 1ms). Since this shutter is electrostatic as opposed to magnetic, it allows for extremely fast hysteresis free beam blanking. STEM imaging allows one to perform parallel recording of EELS and ADF data, which ultimately allows for accurate correlation of spectral features with their precise location within the image.

3.4 Dual Electron Energy Loss Spectroscopy (DualEELS)

The EELS signal contains a wealth of information regarding the compositional, chemical, physical, and electronic properties of materials under analysis. This information spans both the low and core-loss regions of the EELS spectrum. Despite the relatively large dynamic range of modern electron detectors, it is still difficult to acquire

both the low and core-loss regions of the EELS spectrum under identical electron-optical conditions. This difficulty arises from the high intensity of the zero-loss, which is typically many orders of magnitude higher than that of the weak ionisation edges of interest.

The implementation of the DualEELS system allows users simultaneous high-speed acquisition of both core- and low-loss spectra. Concurrent recording of both the core- and low-loss spectra is particularly important as it allows the user to collect a complete view of the energy losses within the specimen. When both the core- and low-loss signals from an identical sample area can be acquired at the same time, additional processing methods become practical such as; the removal of energy shift to allow accurate chemical shift measurements, the ability to perform absolute quantification, capacity for accurate determination of sample thickness, the ability to deconvolve plural scattering and the advantage of being able to correlate low-loss signals with core-loss features (e.g., plasmonics and band gaps). This allows the user to effortlessly measure precise energy shifts and apply advanced quantification routines.

The DualEELS system was designed and implemented by J. Scott *et al.* [114], and uses a fast electrostatic shutter and appropriate hardware which is controlled by additional scripts in the spectrum imaging software. This allowed for the first time, the recording of the whole EELS spectrum at every pixel in a spectrum image along with the X-ray spectrum and the image detector signal. Fast mapping, up to 1000 spectra per second, has now been introduced in commercially available spectrometers [115] and allows the mapping of hundreds of nm of sample at few nm resolution in a matter of minutes. This spectral recording modality helps to overcome the large dynamic range encountered in electron energy loss spectroscopy (EELS) data.

Whilst previous studies have used EELS to analyse the chemistry of the oxidation process of zirconium alloys, the quantification has been limited to a semi-quantitative k -factor approach that does not take proper account of multiple scattering within the material [57]. Moreover, it has not previously been possible to map larger areas of the oxide and metal, or to provide detailed correlated mapping between the electronic structure in the low loss and the chemical information from the high loss datasets. In order to achieve these aims, it is necessary to use near-simultaneous recording of the low-loss and high-loss for all spectra, the so-called DualEELS approach [114]. Specifically, this work applies DualEELS on a modern aberration-corrected STEM to the study of the

evolution of the corrosion of Zircaloy-4, and uses this instrumentation setup which is ideally suited to probe details of the corrosion chemistry through the analysis of the EEL spectra.

3.5 Limits on EELS Spatial Resolution

In this work, all samples mapped were of the order of 100 nm thick, and multiple scattering was significant in all EELS data. Whilst this may have some impact on the spatial resolution of the EELS data, spreading of a beam not placed on a column of atoms along a low-index direction and subject to strong de-channelling is generally not that severe [94] and probably only limits the spatial resolution to a few nm at the worst (i.e. no worse than the chosen map step size).

There was little limitation to resolution arising from the fundamentals of EELS excitation. Core loss edges like Zr-M or L and O-K are from inner electrons on the individual atoms and are, as such only excited by electrons within about 1 atomic radius of the atom of interest (i.e. $\sim 2 \text{ \AA}$). The low loss plasmon region can be excited by Coulomb interactions at a larger distance[94], but in the material with a reasonable concentration of conduction band electrons, dielectric screening still reduces this effect significantly, keeping the effective resolution better than 1 nm, which is significantly below our resolution from beam spreading and our step size. Thus, the fundamental physics of EELS excitation will have a negligible effect on the spatial resolution of these measurements.

Of course, any overlaps of phases within the sample thickness are hard to resolve, although MLLS fitting of low loss can help here in identifying pixels containing two or more components (see below). Ultimately, the interface roughness imposes the most fundamental limit on the spatial resolution of these analyses.

3.6 EEL Data Processing

Every electron energy loss spectrum image acquired inherently contains noise. This can make quantification extremely difficult and many stages can be performed to the dataset in order to distinguish the real data from the noise. Many of the techniques used in order to achieve spectral clean up are standard and are readily available using Digital Micrograph (DM). Post-acquisition, datasets were processed using a sequence of

steps, within Gatan Digital Micrograph (version 2.3), in order to separate the real spectroscopic signals from artifacts and noise, and to quantify the resulting datasets. These processing steps are detailed below.

3.6.1 Basic Dual EELS Processing

i. Pre Zero Loss Background Removal

During acquisition, the DualEELS system can suffer from 'bleed through' between core- and low-loss spectrums, where negative counts cause spurious noise before the zero loss peak. Specifically, if the energy shift between low- and high-loss acquisitions is too small, the zero loss peak on the high loss data does not enter the beam trap at an appropriate point, resulting in extra background prior to the zero loss peak. This has been described recently by Bobynko *et al.* [116].

Low loss stray is also an issue when the ratio between low- and high-loss acquisitions is increased to a value > 1000 . However, in all cases within this thesis, data was acquired with a shift of 160 – 180 eV on the high-loss, as Fe $L_{2,3}$ edges at 721 and 708 eV respectively were the highest edges of interest. This resulted in a relatively small time ratio of around 25 in most cases, thus, pre zero loss background removal was not required. Nonetheless, this step is an important one which must be considered when aiming to acquire edge information at energies in the range of 1500 eV and above.

ii. Align SI by Peak

The Zero Loss Peak (ZLP) acts as a self-calibration for both the low loss and the high loss regions, in that, if the zero loss peak is correctly aligned to zero, any shifts made in the spectrum can also be identically applied to the high loss dataset, allowing for one to accurately check onsets of edges which occur at high energies. Any instrumental instability in the microscope may shift the zero loss peak. Alignment is achieved by selecting the centre of the zero loss peak, and using the Spectrum → Calibrate tab in order to ensure the zero loss peak occurs at exactly 0 eV. One should remember that any shifts in energy performed to the low-loss, should also be performed to the high-loss dataset.

iii. Correct Zero-Loss Centering

Zero loss centering is performed in order to correct the zero loss peak centring

with respect to the calibrated zero loss centre. This procedure is useful, for example, for removing any zero-loss drift from arising from chromatic effects or microscope high-tension instability.

iv. *Extract volume*

After realigning the zero loss peak, a small range of channels at each end of the spectra often contain unreliable data. Moreover, there is loss of detection efficiency at either end of the spectrum caused by shadowing of the electron beam by the entrance aperture of the EELS spectrometer. Only the central region of the dataset where these effects are not an issue is selected, thus cropping the outer edges which contain alignment artifacts is required. This is done using the Volume → Extract tab in Digital Micrograph.

v. *Remove X-rays*

In order to optimise the outcome of subsequent processing steps, x-ray spikes caused by spurious external radiation, alongside energy shifts caused by instrumental instabilities, are removed. The routine checks each image plane of the dataset for spikes which lie more than 10 standard deviations above the local median. If an anomalous pixel is found, its value will be set to the local median.

vi. *Principal Component Analysis (PCA) noise reduction*

A Multivariate Statistical Analysis (MSA) [117] plug in for DM can then be used to perform principal component analysis (PCA) to a SI with proper weighting based on Poisson statistics. This routine separates the real spectroscopic signals from random noise in the datasets [118], producing a screeplot with a log of the eigenvalues of each abstract component in decreasing order of importance. This then allows one to reconstruct a noise-free (or noise-reduced) dataset from the original SI to be used for mapping and quantitative evaluation.

vii. *Log-ratio low-loss deconvolution*

One can choose to deconvolute the SI by electing to remove the effects of plural scattering (described in section 2.3.6) using the Fourier Logarithmic Deconvolution method in DM [119]. This is an optional procedure, and was only used in certain instances within this thesis, for example, when probing Zr L_{2,3} edges.

In principle, this method correctly removes plural scattering from all energy-loss regions of the spectrum at the same time, making it a very efficient procedure. This is particularly important for later processing steps as the thickness of the sample can greatly affect the low loss shapes in the spectrum. Inherently, there are issues with this deconvolution process, in that if there are negative counts in the original data (before the zero loss peak), then the function will introduce artifacts into the resulting deconvolved image. This is why it is particularly important to initially crop the data, so that negative counts before the ZLP due to bleed through are removed before deconvolution. In general however, this procedure was not employed, as the data was deconvolved using the forward modelling approach as will be discussed in Section 3.6.3.

3.6.2 Multiple Linear Least Squares (MLLS) Low Loss Fingerprinting

In order to achieve a spectral signature for each phase pure region within the dataset, Multiple Linear Least Squares (MLLS) Low Loss Fingerprinting can be performed by fitting to standard spectra. Specifically, the program forms a model function consisting of a linear combination of the specified spectra and/or models, and then fits that model to the foreground spectrum by adjusting the coefficient of each linear term to minimize the square deviation between the model and the selected spectrum. In effect, this command is a general (linear) fitting facility that can be applied to the analysis of overlapping edges and superimposed fine structure. This was a trial and error technique, and fits had to be made iteratively to regions which we believed to contribute to the data set, constantly analysing the resulting chi squared map to see where the fits were not perfect. It soon became clear that all contributions to the data had to be fitted, including spectral signatures arising from cracks in the material.

Once the MLLS fit is complete, the algorithm then returns the fit coefficients corresponding to the optimal linear combination of the specified reference spectra to the input data. When applied to an SI, the technique allows one to interpret not only how much of each reference is given but also where. Hence if MLLS is applied correctly to a spectrum-image dataset it provides the ability to map the spatial distributions of the input reference spectra. Specifically, spectral fingerprints of Zr metal, oxygen saturated Zr metal (Zr(O)), ZrO suboxide, ZrO₂ and Zr hydrides were routinely selected for MLLS fitting. This allowed for determination of whether suboxide phases were

present under specific oxidation conditions, by determining whether these phases were just a linear combination of the oxide and metal, or indeed, whether a completely different electronic loss near edge structure (ELNES) was seen, indicating an independent phase. It also proved to be an excellent method to probe the oxidation of Secondary Phase Particles (SPPs) in our Zircaloy-4 material.

3.6.3 Core Loss Quantification

Historically, extracting quantitative information from an EEL spectrum has proven rather difficult due to the complex shape of the EELS edges under analysis and the presence of a strong background resulting in a low signal to noise ratio. The validity of results acquired from previous conventional quantification procedures have been challenged, principally due to inconsistencies in fitting of backgrounds preceding edges of interest as well as issues surrounding the process of Fourier-log or Fourier-ratio low loss deconvolution. Further, the prerequisite of a pre-edge fit region means that this approach is incompatible for the analysis of overlapping edges. To address these issues, J. Verbeeck *et al.* [120] developed significant improvements for a model based quantitative EELS approach, based on fitting a model to observations, using a 'goodness of fit' factor, taking into account all processes involved in the recording of an EELS spectrum. By constructing a parametric statistical model of the observations which depict both what is expected, and the noise statistics, Verbeeck *et al.* [120] were able to obtain estimates of physical parameters describing an EELS spectrum. Following this, Verbeeck *et al.* [121] presented an extension to earlier work, depicting a phenomenological model for the improvement of modelling the electron energy loss near edge structure (ELNES) region. By using an equalisation function, the relative density of unoccupied states for any selected excitation edge could be approximated, resulting in a fitting method which is able to model the entire acquired spectrum including plural scattering effects. This was later interpreted by Thomas *et al.* [122] to allow this routine to be user accessible using Digital Micrograph (DM).

The 'core loss quantification' routine in DM contains an array of edge identification and analysis tools, so that quantitative analysis of EELS edges can be performed in order to achieve elemental concentrations. The process permits the user to swiftly extract and summarise elemental composition data for single or multiple edges from the spectra. This is particularly effective when used in combination with the low loss MLLS fitting. The procedure which is undertaken in order to achieve this is detailed below;

i. Edge Identification

Primarily, one wishes to correctly identify the features in the EELS spectrum i.e. ascertain which spectral features are edges of interest and which ionisation transitions, and therefore what elements they represent. We can have absolute confidence in determining the energy threshold at which the edge occurs as the zero loss peak in the low-loss is calibrated to zero, and any relative shifts are also applied to the core-loss data. With tabulated edge data to look to such as the EELS Atlas [112], the energy threshold of an edge can easily be uniquely correlated with a particular element.

ii. Quantification List Compilation

Using the 'Quantify' tab, the user can then identify the edges to check their identity and mark them for further quantitative analysis. Each edge is then added to the 'Quantification List' for quantitative analysis in the next stage of the edge analysis process.

iii. Edge Setup

This stage in the quantification process varies significantly from one sample to another. The precise set up for each edge will differ due to thickness effects. Precise set up for each quantification scenario is provided in Table 3.1.

In general, suitable signal extraction parameters are specified for each core loss edge within the Quantification List, for example, one must alter the background fit in order to minimise noise and ensure a sensible background fit under the edge of interest, and also must alter the signal window such that it is placed over a suitable area where an edge of increased signal intensity is expected. Fig. 3.5 shows an image window in Digital Micrograph where there is a background fitted before the O edge onset. It can be seen from Fig. 3.5 that the O-K edge onset at 532 eV lies within such close proximity to the Cr-L_{2,3} edge onset at 575 eV, that the two edges have to be overlapped in DM (indicated by a double headed arrow in Table 3.1), with one background fitted before the O edge to remove background from both O and Cr. Special care has to be taken in order to include sufficient ELNES for both edges, whilst selecting a background model which does not over, nor underestimate the signal.

Table 3.1: Details of elements and edges of interest, corresponding edge energy and details of the ideal signal extraction windows for three cases (metal:oxide interface, a $Zr(Fe, Cr)_2$ SPP and a Zr_2Fe SPP) where high loss quantification using the modelling approach was required.

Metal:Oxide Interface				
Element/Edge	Zr M_{4,5}	O K	Cr L_{2,3}	Fe L_{2,3}
Edge Energy (eV)	180	532	N/A	N/A
Signal Extraction (eV)	165 - 235	515 - 600	N/A	N/A
Zr(Fe, Cr)₂ SPP				
Element/Edge	Zr M_{4,5}	O K ↔ Cr L_{2,3}	Fe L_{2,3}	
Edge Energy (eV)	180	532	575 - 584	708 - 721
Signal Extraction (eV)	165 - 235	515 - 630	515 - 630	680 - 770
Zr₂Fe SPP				
Element/Edge	Zr M_{4,5}	O K	Cr L_{2,3}	Fe L_{2,3}
Edge Energy (eV)	180	532	N/A	708 - 721
Signal Extraction (eV)	165 - 235	515 - 600	N/A	680 - 770

A number of factors can prevent such a good fit being obtained. If there is a lower lying edge close to the edge of interest, the overall shape of this edge, its ELNES or its extended energy loss fine structure (EXELFS) can perturb the background shape in front of the edge of interest. If the specimen is relatively thick, plural scattering can also modify the background shape. This is more of a problem for moderate energy losses (up to a few hundred eV), where the background slope changes on the scale of the plasmon energy.

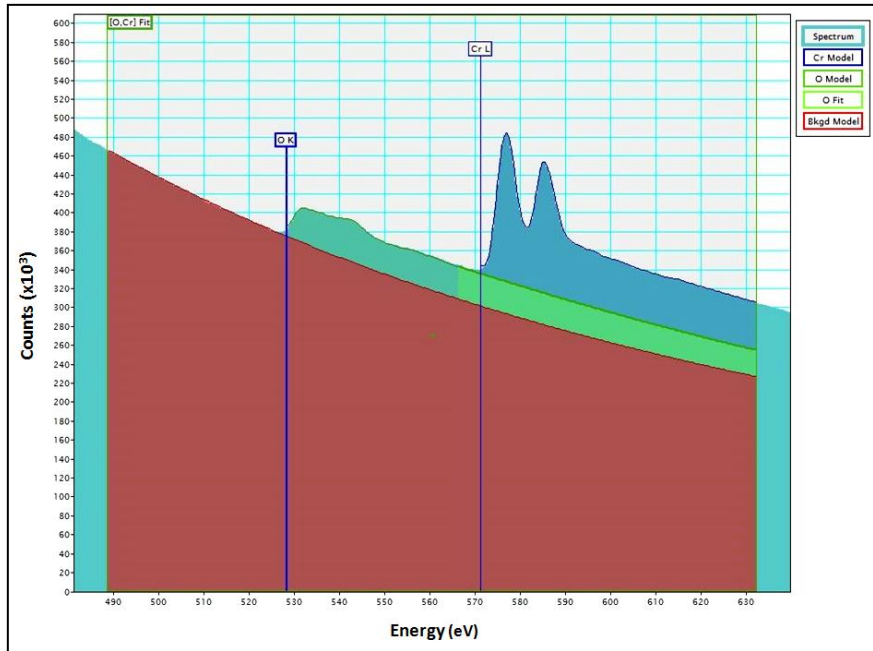


Figure 3.5: A background fitted before the O-K edge onset in order to achieve as sensible a fit as possible to both the O-K, and the Cr-L_{2,3} edges. The background fit was altered to include as little noise as possible, whilst encapsulating an accurate representation of each edge by selecting a sensible ELNES width, background window width and background model.

The cross section model used to provide reliable cross sections for EELS analysis in this thesis is the Hartree Slater model, first calculated by Leapman *et al.* [123]. Calculated in more detail in the following years by Egerton [98, 124] and published as a parameterisation which would work for any element, Gatan use this to generate Hartree-Slater atomic cross sections automatically in the Digital Micrograph software.

The spectrum is then quantified using the specified parameters and areal densities, relative compositions, and edge maps of each element are displayed.

3.7 O:Zr Ratios

The absolute composition of any regions of interest within this work, whether that be the presence of suboxide layers at the metal:oxide interface, or secondary phase particles, was performed using the quantification routine in Digital Micrograph. The routine involves integrating the spectra from much of as much of the area of interest as possible, and quantifying the edges, allowing one to achieve an oxygen concentration for anywhere in the sample.

3.8 High Loss L₂/L₃ Investigations

In zirconium, the two strong L₃ and L₂ threshold peaks originate from the excitation of 2p electrons, and, it is well known that fourth-period elements such as zirconium, give rise to quite distinctive L-edges [93]. These sharp threshold peaks are known as ‘white lines’ as when they were first observed in x-ray absorption spectra, the high absorption peak at the ionization threshold resulted in almost no blackening on a photographic plate [93]. Pearson *et al.* [125] experimentally and theoretically (based on one-electron Hartree-Slater calculations) found that the intensities of L_{2,3} white lines for most of the 3d and 4d transition metals decreased nearly linearly with increasing atomic number, reflecting the filling of the d states in the solid. Fig. 3.6 shows the deconvoluted and background-subtracted L_{2,3} energy-loss spectra for the 4d transition metals. The edge energies are not shown in order to present all the spectra on the same figure, while the intensities of the white lines are scaled simultaneously for all elements.

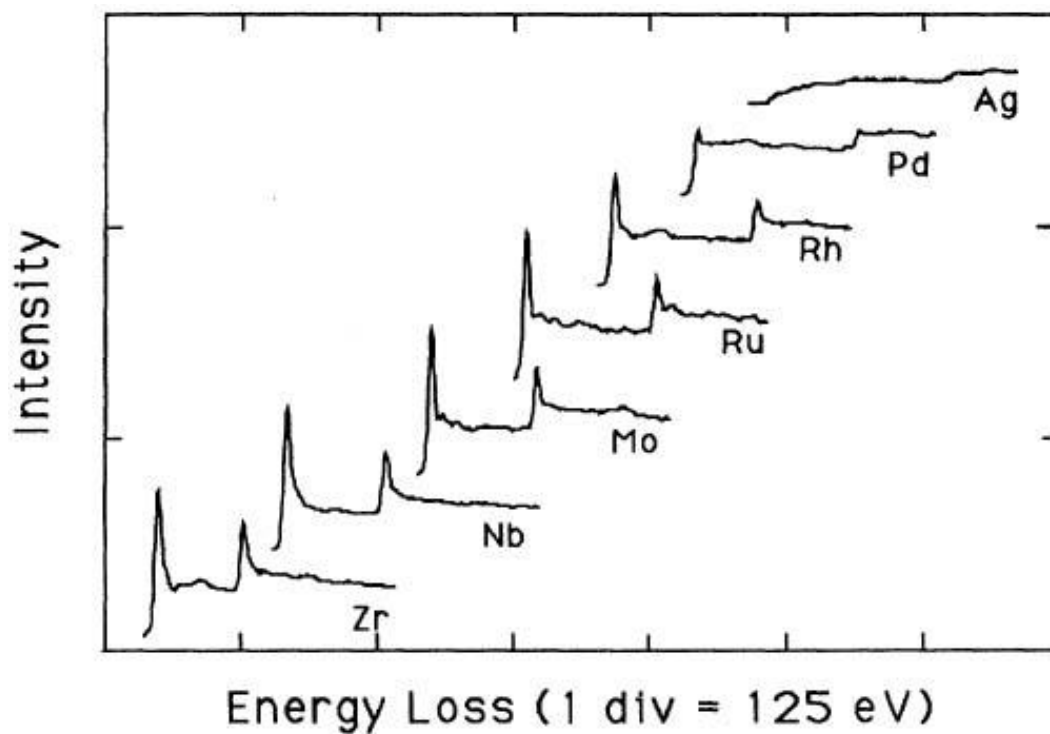


Figure 3.6: The deconvoluted and background-subtracted L_{2,3} energy loss spectra for the 4d transition metals [125].

Spin-orbit coupling causes the magnitude of the L₂ binding energy to be slightly higher than the L₃ level, causing two threshold peaks to be observed, whose separation

increases with increasing atomic number. A study of the white line ratio in Zr-L_{2,3} ELNES for Zr metal, ZrO and ZrO₂ is given in Chapter 4 when discussing the morphology of the metal:oxide interface subject to oxidation. This information is particularly vital as due to the fact that the ratio of the intensities of the L₃ and L₂ white lines are found to deviate from the statistical value based on the relative occupancy of the initial-state values [126] (caused by spin coupling between core hole and the final state [127]), white line ratios prove to be a valuable and reliable indicator when determining valence states.

In summary, this chapter set out to introduce the application of STEM coupled with DualEELS to the analyses of the corrosion of Zircaloy-4 in simulated nuclear reactor conditions. This system is ideally suited to probing energy loss of the incident beam, providing information regarding electronic structure, chemical bonding and valence state of the specimen in nanoscale detail. It has been shown that DualEELS spectrum images can be processed in such a way that allows for the extraction of significant phases from the matrix signal. With the ability to probe differences in oxidation state, one can accurately investigate oxygen containing layers at the metal:oxide interface, the results of which are presented in Chapter 4. Similarly, this set up has been shown to be optimal for probing the corrosion process of SPPs within Zircalloys, as can be seen in Chapter 5, and for probing oxygen content through the oxide scale, as highlighted in Chapter 6 of this thesis.

“Nothing in life is to be feared, it is only to be understood. Now is the time to understand more, so that we may fear less.”

— Marie Curie

chapter

4

The Metal:Oxide Interface

Avast array of careful experimentation has been carried out over the past 50 years on the critical mechanisms of oxidation in the zirconium alloys used for nuclear fuel containment. In particular, the metal - oxide interface has been a predominant focus of previous research, however, due to the complex oxidation process of zirconium cladding, there is still no clear understanding of the chemistry and structure of the interface. Using Scanning Transmission Electron Microscopy (STEM) and Dual Electron Energy Loss Spectroscopy (DualEELS), we have studied the corrosion of this material under conditions similar to those that could be encountered in service. It is shown that under all conditions, whether during faster oxidation in the early stages, slow growth just prior to the transition to a new growth regime, or in the faster growth that happens after this transition, the surface of the metal below the scale is loaded with oxygen up to

around 33 at.%. Approaching transition, in conditions of slow growth and slow oxygen supply, an additional metastable suboxide is apparent with a thickness of tens of nm. By studying changes in both chemical composition and dielectric function of the material at the oxide scale - metal interface with nanometre resolution, quantitative mapping could be achieved, clearly showing that this is a suboxide composition of ZrO with a Zr oxidation state close to +2.

4.1 Motivation

Previous studies such as those highlighted in Chapter 1 of this thesis [40, 45-47] have shown that the link between the transition and lateral cracking in the oxide layer is indicative of some interaction between the mechanical behaviour of the system, and its corrosion kinetics. However, such works do not provide a clear understanding of the morphology of the metal:oxide interface during the corrosion process, at the nanometre level. Understanding why this transition behaviour happens is critical when modelling the rate of growth of oxide, and therefore is crucial to the lifetime prediction of Zr clads, and ultimately to the safety of nuclear power reactors. No model will be complete without a nanoscale understanding of what is going on during oxidation. Whilst a number of techniques have been employed for this purpose, it is clear that various techniques within transmission electron microscopy (TEM) will be among the most versatile and informative for this purpose, although additional information can be added by techniques such as atom probe tomography.

Whilst prior studies have used EELS to analyse the chemistry of the oxidation process, the quantification has not taken proper account of multiple scattering within the material [128]. In addition, it has not previously been possible to map larger areas of the oxide and metal, or to provide detailed correlated mapping between the electronic structure in the low loss and the chemical information from the high loss datasets. In order to achieve these aims, it is necessary to use the DualEELS approach [129], as discussed in Chapter 3. This thesis applies DualEELS on a modern aberration-corrected STEM to the study of the evolution of the suboxide phase through the corrosion process, as well as revealing further details of its chemistry through the analysis of the details of the EEL spectra.

4.2 Experimental Detail

All samples analysed within this study were prepared by AMEC Clean Energy Europe and lifted out using a conventional focussed ion beam (FIB) lift out technique using a FEI Nova Nanolab instrument as also described in Chapter 2 of this thesis. Scanning transmission electron microscopy (STEM) and electron energy loss spectroscopy spectrum imaging (EELS-SI) was performed using a probe corrected JEOL ARM200F (cold FEG) with a GIF Quantum ER electron energy loss spectrometer with DualEELS functionality. Typically, EELS acquisition was done with a probe with a semiconvergence angle of 29 mrad and a post-specimen lens setup that gave a spectrometer acceptance angle (also known as the collection semi-angle) of 36 ± 0.4 mrad for EELS-SI. The Zr-L_{2,3} edge data was recorded at an acceptance angle of 55.1 ± 0.9 mrad. Step sizes for EELS-SI were typically a few nm.

4.3 Post-Processing of Electron Energy Loss Spectroscopy Data

Post-acquisition, datasets were processed using a sequence of steps, all performed within Gatan Digital Micrograph (version 2.3), in order to separate the real spectroscopic signals from artifacts and noise, and to quantify the resulting datasets. Phase mapping could then be performed using the Multiple Linear Least Squares (MLLS) approach, as detailed in Chapter 3 of this thesis. Clearly, in order for the MLLS fitting routine to provide a sensible fit to the data, low-loss spectra for all phases need to be included in the MLLS fit, otherwise spurious and misleading results are found. Notably, this meant that acceptable fits were only achieved for areas containing the ZrO suboxide if a low loss spectrum for this phase was included in the fit. It also meant that even low-loss spectra for the cracks in the oxide in the scan area had to be included as one of the components – these areas contain more surface material and thus have a strong surface plasmon contribution below 10 eV. All these low-loss spectra are shown in Fig 4.1. These spectra will be discussed in the following section, and, in this figure and in all the descriptions below, the following nomenclature is used for phases: Zr – alpha zirconium, ZrHy – zirconium hydride, Zr(O) – alpha zirconium containing diffused oxygen, ZrO – zirconium suboxide, and ZrO₂ – zirconium dioxide. In Fig 4.1, the red dotted line represents the energy (28 eV) where we would expect the Zr N_{2,3} edge onset to occur. In accordance with expectations for such edges, the main peak of intensity is

10-15 eV later. For each phase, multiple measurements were taken over several datasets and an average was taken.

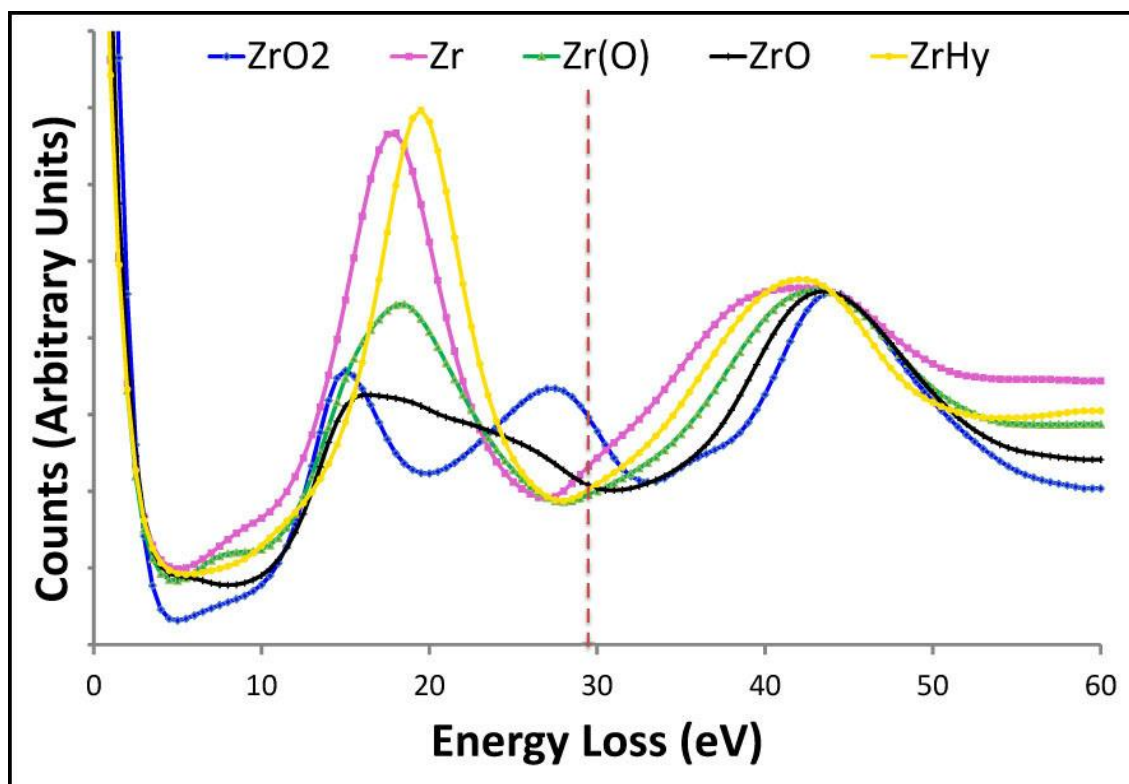


Figure 4.1: Representative low loss spectra for each phase in the oxidised material, recorded for a Zircaloy-4 sample corroded in pressurised water reactor (PWR) conditions at 350 °C.

Quantitative mapping of the core-loss data was performed using a spectrum fitting approach, which explicitly accounts for multiple scattering [99], in a similar manner to earlier work [100, 120, 121, 130-132]. The quantification of the data concentrated on the relative concentrations of Zr and O across the interface and was performed using the Zr-M_{4,5} and O-K edges. Calculated partial cross sections for these edges were used. It was unnecessary to correct the data in any way.

4.4 Results

4.4.1 Details of EELS Spectra from the Different Phases

In order to understand any chemical mapping produced as a result of quantification of the core- and low-loss data, it is necessary to firstly examine the details of the EELS for each phase. Thus, we consider the low loss shape for each phase, the details of the O near-edge structure and how this changes in the transition from metal to oxide, and finally the details of the Zr L_{2,3} edges and what this tells us about oxidation of zirconium.

4.4.2 Low-loss shapes

In Fig. 4.1, everything should be compared to the two obvious end-members in the series. On the one hand, the alpha-Zr metal has just two peaks, a single plasmon peak at about 17.8 eV, in accordance with previous studies [44, 64, 133-135] and which can be explicitly calculated using Equation 3.1, and the delayed peak beyond the Zr $N_{2,3}$ edge at 28 eV. On the other hand, the ZrO_2 phase (blue) shows a three peaked spectral signature on the MLLS fit – two plasmon-like peaks, as in many oxides [44, 64, 133-135], one at 15.7 eV and the other at 27.3 eV, which are suppressed in intensity compared to the metal peak, followed by a rather delayed peak behind the Zr $N_{2,3}$ edge. Metal hydrides appear in the sample, both as a consequence of hydrogen uptake during corrosion, as well as during sample preparation. Their low loss signature is broadly similar to that of Zr metal, with a significant shift of the plasmon energy upwards to 19.6 eV. The oxygen diffused metal, denoted Zr(O), is an ordered or semi-ordered α -Zr(O), where oxygen occupies the octahedral interstitial sites in the α -Zr. Spectra of this phase follows a similar shape to metallic Zr, and has clearly and consistently throughout this work, been seen to exhibit a significantly damped plasmon peak in comparison to metallic Zr, presumably due to the large amount of interstitial oxygen in the lattice. In view of the similarity of the plasmon shape to that in metallic zirconium, we can conclude that this region is likely to be metallic in nature, albeit with a higher resistivity than bulk metal. The ZrO spectrum shows a completely different fingerprint to what would be expected of a typical Zr signal. Instead, the primary plasmon peak is identified by a sharp onset followed by a gradually decreasing shoulder. This signal is clearly not a linear combination of the Zr and ZrO_2 phases, but rather, is a completely distinct signal in itself and is in very good agreement with the shapes calculated by Nicholls *et al.* [64], who calculated this as the sum of 3 different plasmon-like features centered at 13.9, 16.9 and 23.1 eV. This is clear evidence that this phase is no longer metallic in nature, and is an insulator or a semiconductor.

Measurements from the current work are compared with previously measured or calculated values for these plasmon peaks in Table 4.1. The reason for the slightly higher peak positions in this work as compared to previous work is uncertain, but the discrepancies are probably statistically significant as the precision should be of the order of better than 0.5 eV. We are quite certain that the calibration of the spectrometer used in this work was correct and linear, as this calibration was

performed recently before these datasets were acquired. The fact that both the metal peak 1 and the oxide peak 1 are a little high does, however, point to calibration issues, either in this spectrometer or in previous EEL spectrometers used in older work, and this requires further investigation.

Table 4.1: Peak positions in the low loss for the Zr and the ZrO₂, compared with previous published values.

	Metal (Zr)	Oxide (ZrO ₂)	
	Peak 1 (eV)	Peak 1 (eV)	Peak 2 (eV)
This Work	17.8	15.7	27.3
P. Prieto <i>et al.</i> [135]	16.3	14.3	26
C. Palacio <i>et al.</i> [44]	15.9	13.9	27.6
K. O. Axelsson <i>et al.</i> [134]	16.2	13.8	27.3
J. Frandon <i>et al.</i> [133]	16.9	14.8	26
R. J. Nicholls <i>et al.</i> [64]	16.8	14.4	25.4

4.4.3 O Electron Energy Loss Near Edge Structure (ELNES)

Electron energy loss near edge structure (ELNES) is a technique which can be utilised to measure the electronic structure in materials. When a core loss atom undergoes an interaction with the incident electron beam as described in Section 3.2, ionisation edges are created. ELNES is the small perturbations in the intensity just above these edge onsets and has been found to be very sensitive to the details of the local atomic environment such as valence, coordination and type of bonding [136]. Fig. 4.2 shows the O-K ELNES for three of the phases present at the interface, ZrO₂, Zr(O) and ZrO. These have all been normalised to the same maximum height at the first peak. The ZrO₂ shape is consistent with expectations for this phase containing a clearly split peak consisting of a weaker p_1 peak at the front and a stronger p_2 component a few eV higher in energy [137-139]. In contrast to this, both Zr(O) and ZrO show a single peak midway between the p_1 and p_2 positions for ZrO₂. ZrO also shows a slight chemical shift, with respect to ZrO₂ with the edge onset energy about 1 eV later (which is not visible in the figure), which may indicate a reduction in the oxidation state and a reduced amount of charge transfer to the oxygen in this suboxide phase. The additional structure further behind the edge is more difficult to interpret without recourse to

detailed multiple scattering simulations but it is notable that all three phases show characteristic shapes with significant differences in this region about 10 eV after the edge offset.

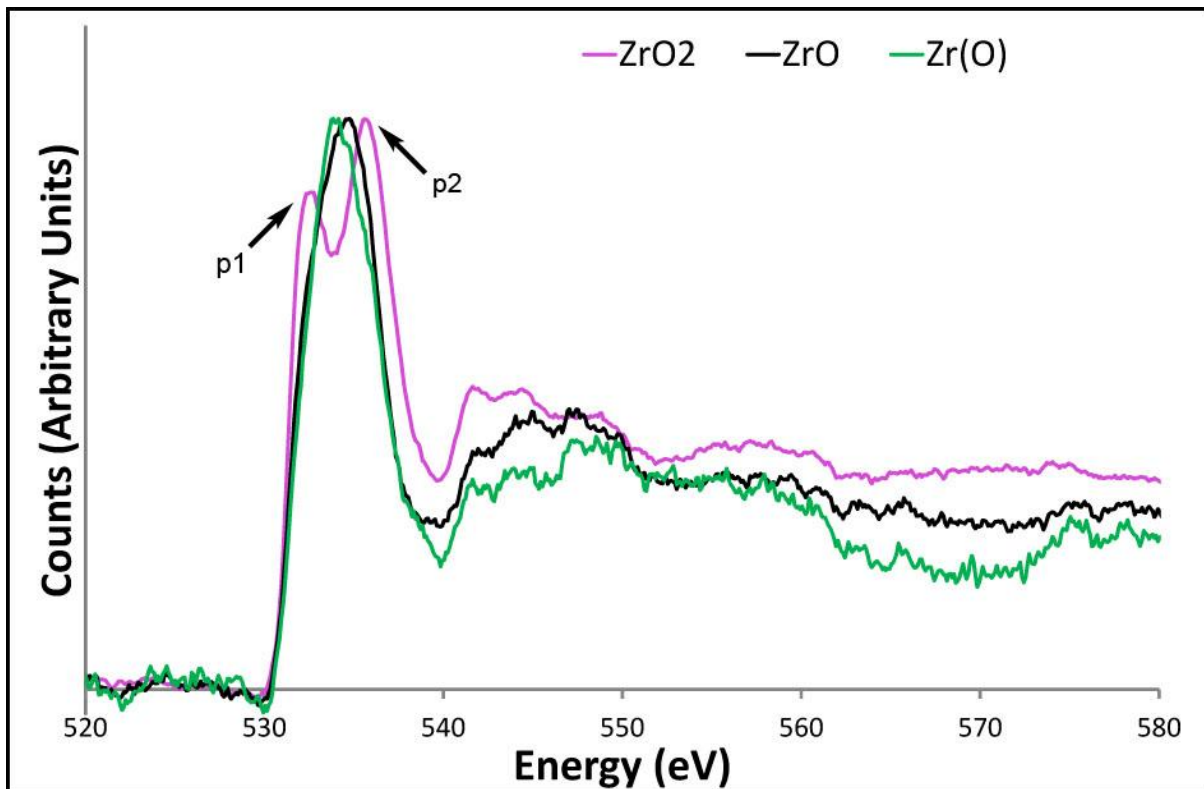


Figure 4.2: A plot of the Oxygen K edges for the zirconium Oxide (ZrO_2), oxygen saturated metal ($Zr(O)$) and the suboxide (ZrO) phases.

4.4.4 Zr- $L_{2,3}$ ELNES

Fig. 4.3 shows the Zr- $L_{2,3}$ ELNES for three phases, Zr metal, ZrO and ZrO_2 . Unsurprisingly, there is a significant increase in the L_3/L_2 ratio for ZrO_2 of 2.45 as compared with metallic Zr with 1.87, as is commonly seen for transition metal $L_{2,3}$ edges on oxidation as a result of the transfer of electrons from the d band to the oxygen. ZrO sits somewhere between these two extremes, with a peak L_3/L_2 ratio of 2.11. This shows clearly that the ZrO is an intermediate oxidation state between the 0 of the metal and the +4 of the ZrO_2 , although it is not possible to directly relate the ratio to the oxidation state without calibrating this ratio to compounds of proven Zr oxidation state, as has previously been performed for Mn and Fe [140-144].

Additionally, there is a notable chemical shift of the onset of both edges on oxidation. At the L_3 edge, this is +2.5 eV for ZrO_2 as compared to Zr metal, as would be expected

due to the increased binding energy for the remaining electrons in a Zr atom on the removal of some outer electrons. As expected, the ZrO lies midway between the two extremes with a shift of about +1 eV, suggesting an intermediate oxidation state. In summary, we conclude that the “ZrO” phase clearly has Zr in an oxidation state approximately midway between 0 and +4, although further work with a standard would be required for definitive proof that this is +2.

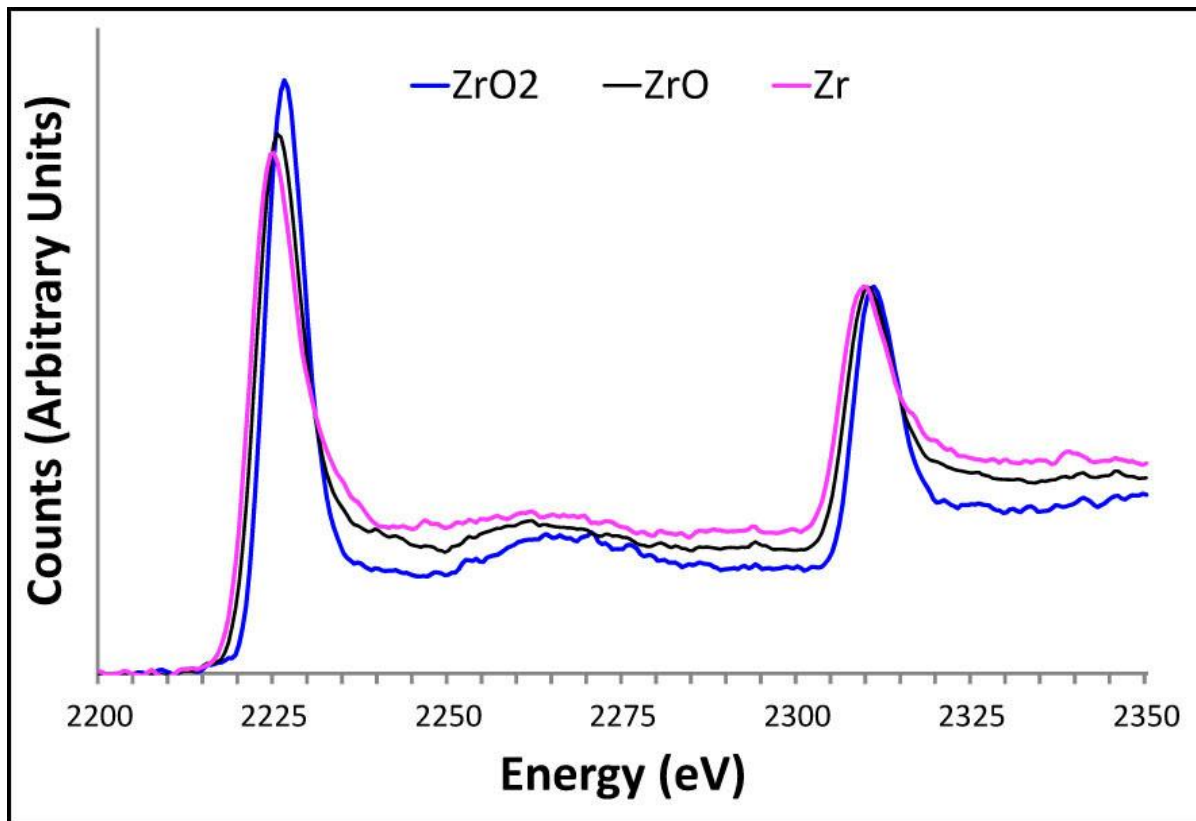


Figure 4.3: Zr- $L_{2,3}$ ELNES for three phases: Zr metal, ZrO and ZrO₂.

4.4.5 Mapping of the Interface Through the Corrosion Process

Armed with a better understanding of the chemistry of the different phases presented earlier in this chapter, we now show chemical mapping of 3 representative samples from different stages in the oxidation process. Firstly, we map a sample relatively early in the corrosion process, where the oxide growth was still fairly fast. Secondly, we map a sample almost at transition. Finally, we examine a sample that is clearly post-transition. In all cases, the data were collected in DualEELS mode and we compare the mapping of low loss shapes to identify different phases with a quantification of the Zr and O content from the core-loss spectra (accounting for multiple scattering).

4.5 Pre-Transition

Fig. 4.4 shows maps of one area of oxide-metal interface in a sample corroded under accelerated pressurised water reactor (PWR) conditions at 350 °C in water to form an oxide of thickness 1.5 μm (prior to the transition to a rapid corrosion rate). It is immediately apparent in the O percentage map and the line trace that there is a relatively thick region of roughly 300 nm diffusion of oxygen into the metal matrix. This region is also clearly seen in the MLLS fit map to the low loss as the green phase (fitting the Zr(O) shape in Fig. 4.1). Quantifying the oxygen content in this region shows that it rises from almost zero in the pure metal to a plateau region of around 30 at.% oxygen, as exemplified by the plot. Whilst there is significant O-diffusion into the metal, there is absolutely no evidence for a ZrO suboxide phase in this sample – there is a very thin yellow line in the Zr and O percentage maps that corresponds to this composition (yellow is around 50% on the colour scale), but no distinct low loss shape for this phase is seen, even in the areas where the yellow area appears thicker. This suggests that the 50% regions are simply found as a consequence of interface roughness and the overlap of Zr(O) and ZrO₂ regions in the thickness of the specimen.

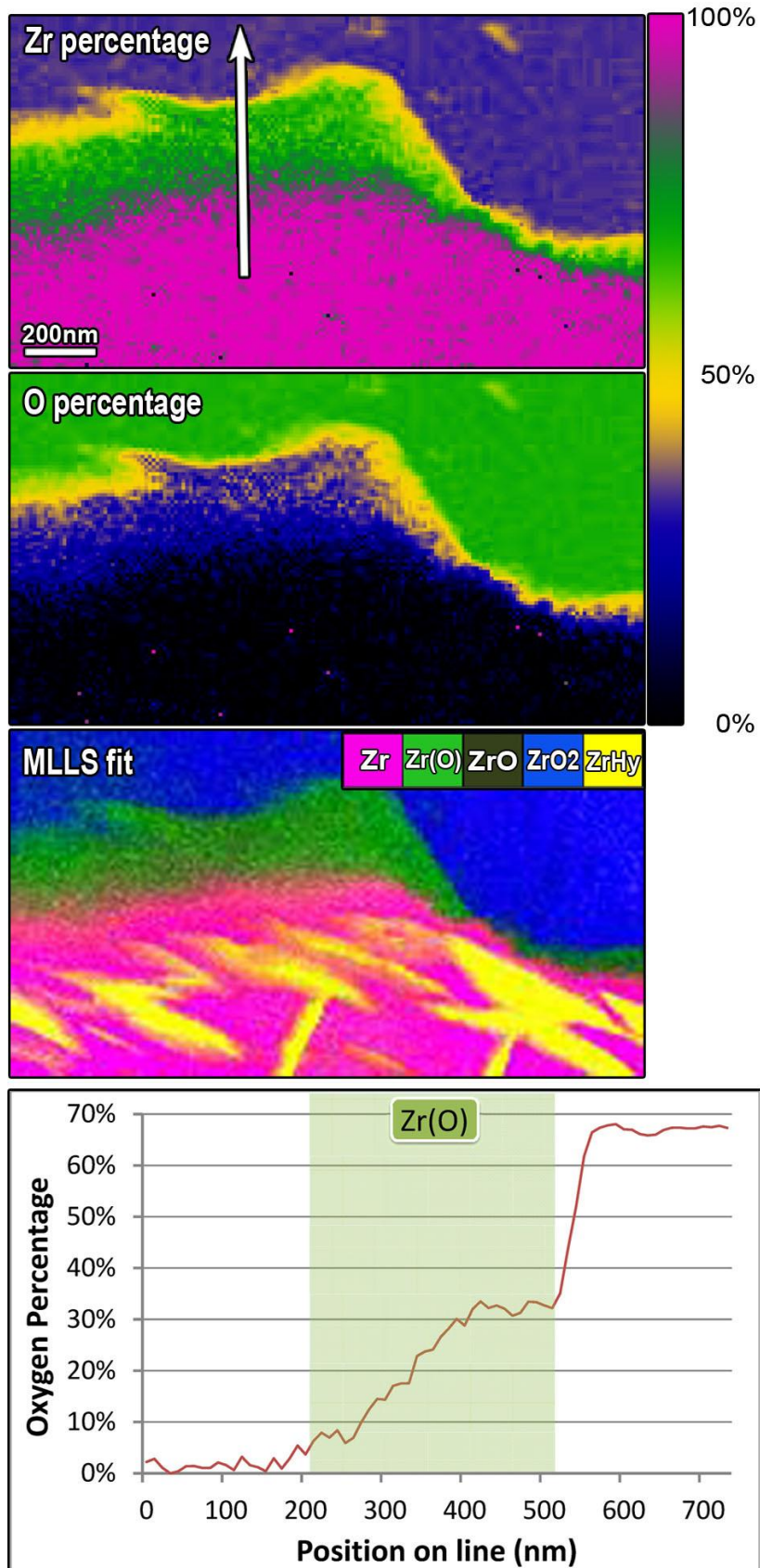


Figure 4.4: EELS mapping of an oxide-metal interface in a pre-transition specimen. From top to bottom: Zr percentage composition map on a quantified colour scale; O percentage composition map on a quantified colour scale; multicolour composite image created from MLLS fitting of the low loss for each phase; line profile taken across the sample in the direction indicated by the arrow in the Zr percentage map, with an overlay box depicting the Zr(O) area.

4.6 At Transition

Fig. 4.5 shows maps of a sample corroded under the same conditions for longer until an oxide thickness of 2.17 μm was formed. From the corrosion data of numerous samples, it is known that this thickness is just prior to the transition point at which the corrosion rate increases again [45].

As for the pre-transition sample, there is a significant layer of oxygen diffused Zr, the so-called Zr(O) phase, as can be seen in green in the Zr percentage and the MLLS fit maps. This reaches thicknesses of 400-500 nm at points, and a peak composition just over 30 at.% O. In contrast to the pre-transition sample, however, there is also a distinct suboxide phase between the Zr(O) and the ZrO₂. This shows up very clearly in both the Zr percentage and O percentage maps as yellow (~50%), and is depicted in the MLLS fit as black. This region is rather rough with sharply defined, almost saw-tooth shaped, boundaries to Zr(O) which is concurrent with findings by Ni *et al.* [33]. This suboxide region has thicknesses varying between just a few nm and 200 nm. In the particular case shown, there are additional areas of ZrO fully encased in the ZrO₂ below the crack.

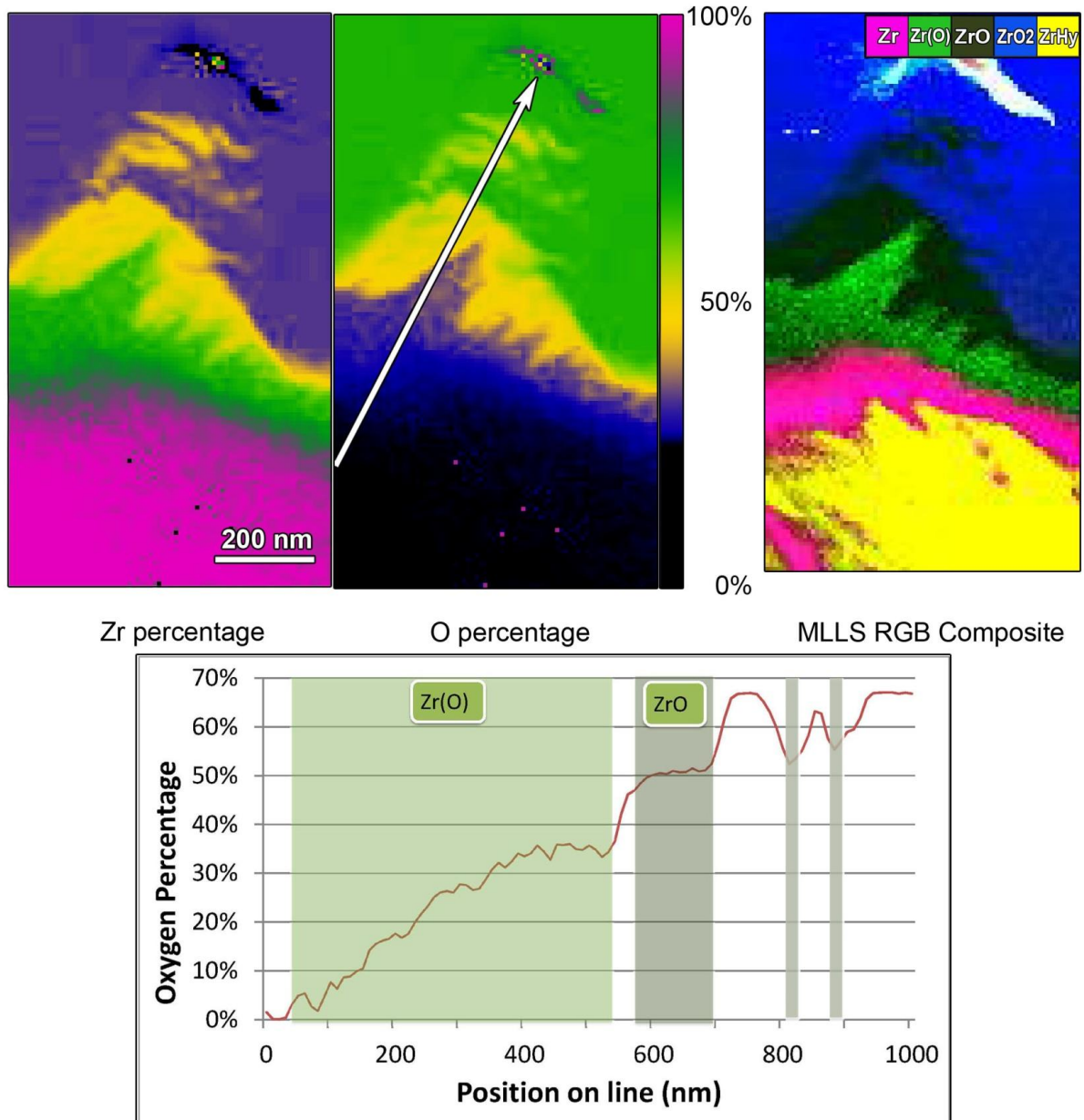


Figure 4.5: EELS mapping of an oxide-metal interface in a specimen at transition. Along the top from left to right: Zr percentage composition map on a quantified colour scale; O percentage composition map on the same quantified colour scale; multicolour composite image created from MLLS fitting of the low loss for each phase. Bottom: line profile taken across the sample in the direction indicated by the arrow in the Zr percentage map, with overlay boxes depicting the Zr(O) and ZrO areas.

4.7 Post-Transition

Fig. 4.6 shows maps from a third sample, this time representative of the post transition phase of oxidation, with an oxide layer of around 2.85 μm in thickness. This sample exhibits an oxygen diffused metal region of around 150 nm, but it is clear that any suboxide layer is undetectable at this point in the oxidation process. As for Fig. 4.6, there is a very thin yellow line in the percentage maps, but this does not correspond to any ZrO low loss shape and is almost certainly just due to interface roughness in the thickness of the specimen, resulting in the overlap of ZrO_2 and Zr(O) areas.

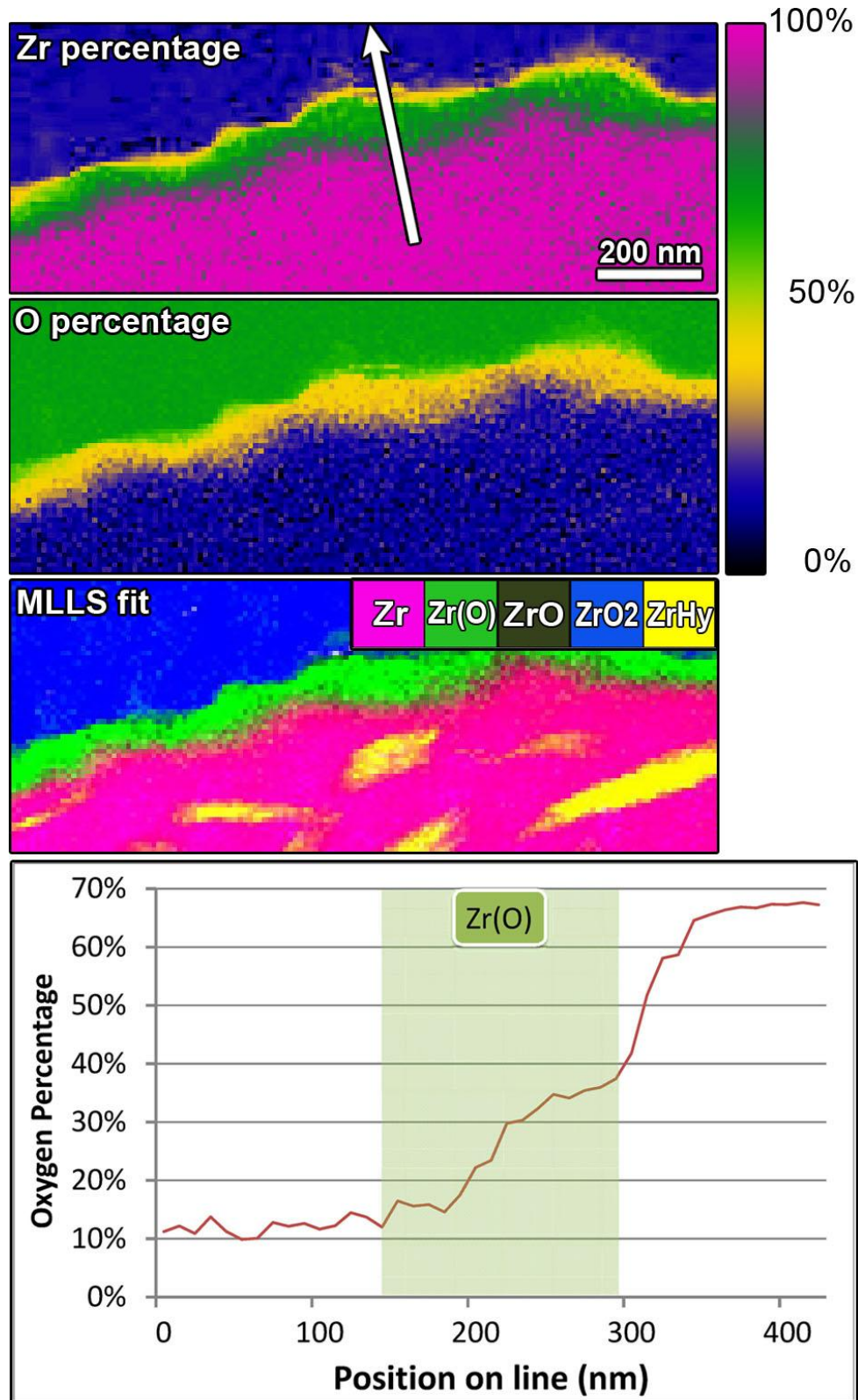


Figure 4.6: EELS mapping of an oxide-metal interface in a post-transition specimen. From top to bottom: Zr percentage composition map on a quantified colour scale; O percentage composition map on a quantified colour scale; multicolour composite image created from MLLS fitting of the low loss for each phase; line profile taken across the sample in the direction indicated by the arrow in the Zr percentage map, with an overlay box depicting the Zr(O) area.

4.8 Discussion

As has been shown previously, EELS is extremely well-suited to the analysis of the chemistry of Zr:ZrO₂ interfaces in oxidised Zr-base nuclear alloys [33, 64, 128]. Unfortunately, previous generations of spectrometers had limited speed readout and this restricted the area that could reasonably be analysed by EELS, and the majority of work was performed by simply taking line profiles through interfaces. The full complexity of the chemistry of the interfaces can only, however, be revealed in a two-dimensional map. With the advent of newer EEL spectrometers that can read out at up to 1000 spectra per second [145] it is now possible to map hundreds of nm of sample at a few nm resolution in a matter of minutes. This has been used in the present work to show both the phase distribution and detailed chemistry of these complex interfaces and to illustrate the changes that go on as the oxidation process advances.

Additionally, previous EELS studies have performed quantitative studies using just the core-loss spectra using a phenomenological *k*-factor approach [146] corrected using the assumption that the outer oxide is ZrO₂ [128]. This *k*-factor approach involves calculating the partial scattering cross-sections for K ionisations as determined by fabrication of thin film standards, which can be done with some accuracy [147]. Thus, unknown cross-sections of L, M, N or O ionisations can be calculated. This *k*-factor approach does not require accurate knowledge about the thickness of the *standard* sample, however, it should be noted that as the ELNES of the core-loss signal depends on chemical environment, implementation of the *k*-factor approach as a routine method of analysis in EELS is problematic [148]. Clearly, this only works up to a point and does not properly account for the effects of *specimen* thickness and multiple scattering, and so the quantification results may not be entirely linear with concentration and may be slightly thickness dependent. Thickness effects will always be an issue in specimens prepared using the FIB lift-out technique where it is essential that alongside a section of bulk metal, a several micron thick layer of oxide is required to be extracted for analysis. As described in Chapter 2, a sufficiently long specimen cannot feasibly be thinned to much less than 100 nm, and thus, plural scattering (detailed in Chapter 2) is inherently an issue. It has been known for some time that the ideal approach is to remove the effects of multiple scattering from the quantification. This could be done in one of two ways: either the low loss spectrum is deconvolved from the core-loss spectrum [93] using the Fourier-log or Fourier-ratio methods as discussed in Section 3.6.1, or the high loss spectrum is modelled as a forward convolution of a model spectrum and the low loss in

an iterative procedure [100, 120, 121, 130, 131] as described in Section 3.6.3. In either case, mapping chemistry in a quantitative manner therefore requires a near-simultaneous, fast recording of the low-loss and the high-loss data. This capability has been developed in previous work at Glasgow on the development of the DualEELS concept [129]. The subsequent commercialisation of this into the latest generation of spectrometers and its combination with fast readout technology [145] has allowed the large area, high resolution DualEELS mapping that makes this quantitative visualisation of the chemistry possible in 2D. An EELS modelling approach has been chosen to perform the quantification, as this worked well on the relatively thick specimens ($t/\lambda > 1$) used in this work, and was more noise tolerant than deconvolution.

An additional benefit of having the low loss datasets was that the plasmon and low loss shapes could also be mapped for each region. Since these are distinctive to each phase and act as a sensitive fingerprint of the local electronic structure (i.e. the real part of the dielectric function) then this is a powerful way of distinguishing similar phases, such as Zr metal from Zr hydride or Zr(O). The visualisation of these in multicolour maps using MLLS fitting therefore provides a useful counterpart to the quantitative Zr and O content maps from the core-loss spectroscopy. This has an additional advantage over the use of elemental quantification from core-loss EELS alone, that the overlap of two phases in the beam path due to the interface roughness will give a weighted average of the Zr:O ratio of the two phases, which is not unambiguously interpretable, whereas MLLS fitting fits this as a sum of the two phases with distinct low-loss shapes and is not confused by the overlap.

A further advantage of DualEELS for this kind of work is that these low loss spectral shapes can be analysed in detail for each mapped area. A new feature of this work is the clear and consistent reporting of a distinct plasmon shape for Zr(O) as shown in Section 4.2.2. This plasmon appears at almost the same position as the plasmon for metallic Zr, but is significantly damped. It would suggest therefore that the incorporation of oxygen into Zr up to the solid solubility limit does not prevent the Zr(O) from behaving as a metal, but the damping of the metallic plasmon suggests a change in the resistivity of the metal. This presumably happens through impurity scattering by the interstitial oxygen atoms, and the high concentration of these oxygen atoms allows the impurity scattering to dominate the transport behaviour right to room temperature. In contrast to this, the ZrO shows a very clear ‘shoulder’ to the primary plasmon peak and this very spread peak is in good accordance with the experiments and simulations reported by Nicholls *et al.* [64].

A further unique feature of this study has been the possibility to measure the absolute energies and the relative chemical shifts of the Zr L_3 and L_2 edges with high reliability because of having the absolute reference of position of the zero loss peak for every data point. Consequently, we can clearly show that when going from metallic Zr to ZrO_2 , a chemical shift of +2.5 eV is noticed at the L_3 edge. In the ZrO, this chemical shift was approximately +1 eV, which would suggest an intermediate formal oxidation state between the 0 of Zr metal and the +4 of Zr in ZrO_2 . This is consistent with work done on Zircaloy-2 by Yoshitaka *et al.* [56] who postulated a ZrO oxidation state of +2. Simultaneously, it was possible to examine the white line ratio of the L_3 and L_2 edges for these 3 phases in much the same way as has been performed for a range of first row transition metals in the past [140, 141, 143, 144]. This showed that ZrO had a peak L_3/L_2 ratio of 2.11, which is midway between that for Zr^{4+} in ZrO_2 of 2.45 and that of Zr^0 in metallic Zr with 1.87, following a similar trend to that for iron oxidation in which the L_3/L_2 ratio increases with increasing oxidation state [141], rather than the trend seen for manganese in which the L_3/L_2 ratio decreases with increasing oxidation state [140, 143, 144]. In both of these studies, the relationship between the oxidation state and the white line ratio was non-linear. Consequently, there is no reason why the white line ratio of the Zr^{2+} state should be the arithmetic mean of those for Zr^0 and Zr^{4+} , which would be 2.16. Nevertheless, the fact that the measured white line ratio for ZrO is 2.11 certainly suggests that the oxidation state is likely to be close to +2. Confirmation of oxidation state could be achieved by comparison with white line ratios from well-understood standards, as used in previous studies of first row transition elements [140, 141, 143, 144]. More generally, this also suggests that the use of white lines ratios at the L_3 and L_2 edges could also be more generally used in EELS for the characterisation of the oxidation states of second row transition elements. Of course, it would also be possible to determine oxidation states of these elements by MLLS fitting between standard spectra, as was previously performed for Fe by Garvie and Buseck [142].

Analysis of the O electron energy loss near edge structure (ELNES) for the three phases - ZrO_2 , Zr(O) and ZrO - allowed for the direct comparison of the shape of each of the oxygen K edges. As can be seen in Fig. 4.2, the ZrO O-K near-edge structure has a somewhat similar shape to the O-K structure of oxygen saturated Zr metal, albeit showing a shift in the ZrO edge onset energy about 1 eV later in comparison to Zr(O). This shift may indicate a reduction in the oxidation state and a reduced amount of

charge transfer to the oxygen in this suboxide phase and suggests that they may have similar oxygen coordination. This is intuitive as the O positions in both oxygen saturated Zr and ZrO have similar bonding and coordination. Studies undertaken by Puchala *et al.* [50] confirm that as hexagonally close-packed Zr is able to dissolve unusually high amounts of oxygen into its interstitial octahedral sites, it has the ability to create a range of ordered suboxides up to a composition of ZrO. All of these contain oxygen in octahedral interstices. All were predicted to be metallic. Thus, the oxygen environments in ZrO and in the lower suboxides should be very similar and it is therefore not surprising that these have a very similar O-K ELNES, which was found to consist of a single unsplit peak just after the edge onset. It is likely that the subtle differences are due to the influence of other oxygen atoms on the Zr neighbours for ZrO, an effect that will be less prevalent for the lower suboxides. All this is radically different to ZrO₂, which showed a completely different ELNES, with a clearly defined split peak, consisting of a weaker p_1 peak at the front and a stronger p_2 component a few eV higher in energy [137-139]. These observations are consistent with those of Ostanin *et al.* [137] for monoclinic (*m*) ZrO₂, which is already known to be the majority phase in the oxide scale [48].

With the benefit of being able to map a few μm^2 of metal-oxide interface to show both phase composition and oxygen and zirconium content, it is now possible to discuss in more detail the chemical changes going on during the oxidation of Zircaloy-4 in superheated water. As shown in Fig. 4.4, in the pre-transition stage of corrosion after the initial fast growth phase, a certain degree of roughness develops on the oxide-metal interface. Parts of the interface (left of the figure) lie deeper into the metal and suggest that oxidation has been happening faster at this point, whilst other parts (centre and right) show a slower growth of oxide into the metal. This correlates clearly with the thickness of oxygen-loaded zirconium. In the regions with fast growth of oxide, there is little opportunity for further significant diffusion of oxygen into the metal ahead of the growth front and the Zr(O) layer is rather thin and much less than 100 nm. At other points where growth is slower, then the width of the Zr(O) layer is much larger, measuring hundreds of nm, and it would seem that when growth of oxide is slowed, the free oxygen available has time to diffuse long distances into the metal. The reasons for this roughening are not totally clear from this study, but it may be that local differences in the outer oxide scale are causing difference in the rate of oxygen transport that result

in some regions growing quicker than others. These local variations in oxidation rate have also been seen by Ni *et al.* [33] in ZIRLO and by Tejland *et al.* [45, 58] in samples of Zircaloy-2 who purport that this interface undulation exists in both the large scale (typically 20 μm) and on the small scale (typically around 1 μm), and there is suggestion that this wavy interface is most probably a two-dimensional representation of a 3-dimensional “cauliflower” oxide structure. Bossis *et al.* [52] also confirmed using SEM on samples of Zircaloy-4, the occurrence of a wavy interface, identified as a succession of advanced and delayed portions of the oxidation front, distanced by up to 1 micron. These local deviations in the rate of oxidation have also been witnessed by Saillard *et al.* [149] when studying the development of stress-induced roughness during oxide scale growth on a metallic alloy for solid oxide fuel interconnects. At this early point in the corrosion process however, there is no convincing evidence for the growth of any ZrO at this point in the corrosion, and oxygen supply to the interface is clearly sufficient to make direct conversion of Zr(O) to ZrO₂ the dominant process. This conclusion, whilst explaining the dataset presented here, is completely representative of a range of studies carried out on a number of pre-transition specimens.

As shown in Fig. 4.5, the interface roughness is further exaggerated in the sample at transition and additionally a significant amount of ZrO occurs at the interface. This roughness occurs both in the form of a bumpy metal oxide interface, but is also demonstrated by a rather jagged and well defined interface between the ZrO and the Zr(O). Such an effect has been seen previously by Ni *et al.* [33] (particularly in their Figure 10), Bossis *et al.* [52] and Tejland *et al.* [60] and has also been seen in other samples examined at Glasgow, both from this specific material and other near-transition specimens. This would suggest that the transition from oxygen loaded metal to ZrO is abrupt. Quite why this generates such saw-toothed structures, however, is an interesting question that requires further investigation. One particular feature of interest is that the largest amount of ZrO was found beneath a lateral crack at a particularly slow-growing part of the ZrO₂:Zr interface. Additionally some regions of ZrO were found stranded within the ZrO₂ beneath this crack. Finally, the Zr(O) area is relatively wide for most of the interface in this specimen. Quite why there is so much metastable ZrO and Zr(O) would tend to suggest one of two things. Either, the lateral crack is actually blocking the supply of oxygen to the region below it and thus stabilising the ZrO phase, as well as a particularly wide region of Zr(O) below this – which is

entirely consistent with the recent work of Yardley *et al.* [150] who showed using ^{18}O tracer studies in SIMS that lateral cracks can block oxygen transport to the interface. Alternatively, rather than the cracks being the cause of slow oxidation, they could instead be the result thereof, since, due to very high tensile stresses perpendicular to the interface, cracks are formed above parts of the interface where the oxide front has not advanced so much [45, 48, 151]. Once the transition has taken place, the difference in the distribution of phases is remarkable. The metal-oxide interface is much flatter, no ZrO is found, and there is very little Zr(O) . Again, this conclusion is based on examining many areas in the microscope, and not just one dataset. This transformation is consistent with a plentiful supply of oxygen to the interface through an interconnected network of cracks in the outer oxide resulting in fast oxidation and minimal formation of metastable phases. This is also consistent with the previous studies of Yardley *et al.* [150] and Ni *et al.* [33], that oxygen supply to the interface is very fast immediately after transition resulting in the fast growth of a dense oxide scale and a flat interface.

There is finally an interesting observation and question. In this work, it is found that the Zr(O) is wider where growth of oxide is slow and narrower where oxide growth is fast. This trend was not observed by Tejland *et al.* [58] for the oxidation of Zircaloy-2 tube, but this was only done for a small number of EDX line scans (rather than the larger area maps used in this work). However, similar observations to those in the present work have been made by Ni *et al.* [33] using combined EELS/STEM and APT analysis on samples of ZIRLO and Zircaloy-4 in order to study this oxygen-saturated (30 at.% O) metal region. Evidence from diffraction patterns suggested that the Zr_3O phase is confined to this oxygen-saturated metal layer and after studies were performed on all samples, it was found that this layer was thickest in the (late) pre-transition samples and significantly thinner in the post-transition samples in much the same way as observed in this work.

According to Béranger and Lacombe, [152] the diffusion profile only depends on the diffusion coefficient for oxygen in the metal, the time for diffusion and the oxygen concentration in the metal at the metal/oxide interface. The latter of these seems to be fixed at around 33% and the diffusion coefficient should also be fixed at any given growth temperature. However, the time for diffusion may well be much reduced if the oxide interface is growing rapidly, which may well explain this observation. Further work is needed on calculations to investigate this point in detail.

In summary, combining EEL spectroscopy with imaging on a modern aberration-corrected STEM has not only allowed for the development of the understanding of the metal:oxide interface of Zircaloy-4 at the sub angstrom level pre-, at and post-transition, but has provided the required technology with which to produce detailed maps of the interface. Considering the low loss shape for each phase, the details of the O near-edge structure and how this changes in the transition from metal to oxide and finally probing the details of the Zr $L_{2,3}$ edges have facilitated a more accurate prediction of the performance of this existing alloy. However, whilst a thorough understanding of the morphology of any suboxide phases generated during the process of corrosion is fundamental, no model is complete without contemplating the effect the alloying elements have on the rate of the corrosion process. Chapter 5 will provide a study of the nanoscale details of the corrosion of intermetallic $Zr(Fe, Cr)_2$ and Zr_2Fe secondary phase particles in Zircaloy material under differing temperatures and pressures. This nanoanalytical approach will inform the role of SPPs and the influence the different alloying elements have on the oxidation mechanisms taking place within the alloy. Ultimately, the revelation of the true complexity of the oxidation of the SPPs is necessary for the development of sophisticated models of their influence on oxidation behaviour.

*"In nature's infinite book of secrecy
A little I can read."*

— William Shakespeare

chapter

5

Secondary Phase Particles (SPPs)

As in the previous chapter, Scanning Transmission Electron Microscopy (STEM) coupled with Dual Electron Energy Loss Spectroscopy (DualEELS) has been utilised to study one facet of the corrosion of Zircaloy-4. This chapter focuses on the corrosion and incorporation of Secondary Phase Particles (SPPs) in the oxide layer of the material. Specifically, mapping of Zr_2Fe and $Zr(Cr,Fe)_2$ precipitates during the oxidation process has been performed, and their morphology analysed as the oxidation front advanced through the material.

It has been found that the Zr_2Fe SPPs exhibit no notable change in their internal structure upon oxidation. They retain the same general shape as in their pre oxidation stage and depict a composition consistent with full oxidation of both Fe and Zr.

The $\text{Zr}(\text{Cr,Fe})_2$ SPPs however, oxidise in a notably more complicated manner. As these precipitates exhibit the hexagonal Laves phase structure, they originally appear as very faceted structures within the metal matrix. The body of the SPP tends to contain more Cr than Fe, however, Fe is often seen to segregate to the outside rim of the particle, and occasionally also sit preferentially in regions within the body of the particle, resulting in Fe enriched areas. As the α -Zr around an SPP begins to oxidise, the SPP is completely encapsulated by the ZrO_2 whilst much of the SPP remains initially unoxidised. Upon oxidation of the SPP, an out-of-plane expansion occurs due to the volume expansion on the formation of the oxide, often resulting in particles that are quite elliptical in cross section with the major axis in the out-of-plane direction. Additionally, the elemental distribution does not remain homogeneous, as in the original SPP, and three principal phases have been identified in the oxidised SPPs. The first thing to oxidise (i.e. the cap of the precipitate) is very Cr-rich and is probably mainly Cr_2O_3 with some Fe substitution – this must consume a reasonable proportion of the Cr in the SPP. Subsequently, the main body of the particle itself is found to oxidise to a Zr, Cr oxide with an approximate 3:2 ratio of Zr:Cr, and very little Fe content. The result of the formation of this majority phase and the rejection of the Fe is the precipitation of veins of Fe-rich material. Early in the process, this Fe remains at least partially metallic. Even when the SPP is well encapsulated in the oxide scale, Fe-rich veins have been observed to be very low in oxygen.

5.1 Motivation

As detailed in Chapter 1, as α -phase zirconium has a high affinity for transition metals, the formation of second phase particles (SPPs) is favoured. These alloying elements sit within the Zr matrix as globules of complex intermetallics which are entirely insoluble in the metal matrix and improve the corrosion resistance of zirconium based alloys by anodic protection [69]. Whilst there have been many previous studies of the oxidation of SPPs in Zircalloys, most studies have left significant unanswered questions. In particular, most studies to date have either performed some imaging and some diffraction, or some imaging and some single point chemical analysis. Performing spatially resolved chemical mapping, and correlating this with the actual crystallographic structure is essential to a complete understanding of what actually happens when SPPs in Zircalloys are oxidised. Achieving a thorough understanding of the microscopic details of the corrosion of secondary phase particles will aid to inform

the macroscopic details of corrosion of the alloy, ultimately, to more precisely predict the behaviour of the corrosion and determine a more accurate lifespan of nuclear fuel rods. Details of the two categories of SPP which have been found in the Zircaloy-4 material as detailed in this thesis - Zr_2Fe -type and $Zr(Fe,Cr)_2$ -type - can be found in Table 1.2.

5.2 Microscopy of SPPs

The current work is a systematic study of the chemistry and morphology of SPPs in standard recrystallised annealed (RXA) Zircaloy-4 (Zr-1.5%Sn-0.2%Fe-0.1%Cr) after corrosion in pressurised water at 360 °C covering both Zr_2Fe and $Zr(Fe,Cr)_2$ type precipitates. All samples analysed within this study were prepared by AMEC Clean Energy Europe, and prepared for STEM analysis using the FIB lift-out technique by Glasgow University, as detailed in Chapter 2 of this thesis.

In order to determine crystallographic information of the particles, scanned diffraction was performed with a JEOL ARM 200F microscope using aberration-corrected Lorentz-mode (i.e. objective lens switched off, and the probe formed using the condenser lenses and the aberration corrector, with a small convergence angle) [153]. Acquisition of the scanned diffraction datasets was controlled using the Diffraction Imaging plug-in for Spectrum Imaging within Gatan Digital Micrograph. Datasets for Zr_2Fe and $Zr(Fe, Cr)_2$ -type SPPs in the oxide were acquired using the 30 μm condenser lens aperture which gives a convergence angle of 1.3 mrad and a diffraction-limited probe size of ~ 0.8 nm, a 40 cm camera length to give the appropriate size of diffraction pattern on the Gatan Orius CCD camera, and a 0.5s exposure time per pixel for the $Zr(Fe, Cr)_2$ dataset, and a 0.2s exposure time per pixel for the Zr_2Fe dataset.

All phases were calibrated on the assumption that the matrix of the bulk material was primarily monoclinic ZrO_2 , as consistent with Garner *et al.* [32] and many other studies.

As always, all images shown are oriented so that the vertical direction upwards is towards the outer surface of the oxide scale, and the vertical direction downwards is towards the metal bulk.

5.3 Results

This study has focussed on analysing the morphology and chemical composition of both Zr_2Fe and $Zr(Cr,Fe)_2$ SPPs found within samples of Zircaloy-4, as the oxidation front advances through the metal matrix. Particular focus has been made on mapping the particles both pre, and post oxidation. However, there are a few instances where the $Zr(Cr,Fe)_2$ particles are seen to sit right at the metal:oxide interface, just undergoing, or having undergone oxidation. Special mention will be made of these instances in section 5.3.4 when discussing the initial corrosion of these binary particles.

5.3.1 Zr_2Fe SPP in metal

Whilst Zr_2Fe SPPs have rarely been reported in the literature, more than 30 different Zircaloy-4 specimens have been prepared and analysed and Zr_2Fe -type precipitates have been observed on multiple occasions (even if they are still rarer than Laves phase SPPs). Fig. 5.1 shows elemental maps of Zr and Fe of one such particle within the unoxidised metal, together with a background-subtracted EEL spectrum covering the range from 500-800 eV (which includes oxygen-K and iron- $L_{2,3}$ edges as seen in Chapter 3, Section 3.2).

Quantification of this high-loss data (performed as detailed in Chapter 2) has shown that there is no detectable chromium content within this particle, as can be seen in the EEL spectrum in Fig. 5.1c, where the white lines of Cr above 575 eV are notably absent. Any presence of oxygen in the specimen is a consequence of surface oxidation. The absolute composition of the particle is shown in Table 5.1 and this is fully consistent with the idealised Zr_2Fe stoichiometry.

This specimen has an oxide thickness of 4.05 μm and thus, is a post transition specimen. The SPP is located $\sim 3 \mu m$ below the metal oxide interface, as can be seen in Fig. 5.1 d.

Table 5.1: Chemical composition of a typical Zr_2Fe particle found in the metal as determined by EELS analysis.

Element	Composition (at. %)
Zr ($M_{4,5}$ edge)	62 ± 5
Fe ($L_{2,3}$ edge)	38 ± 5

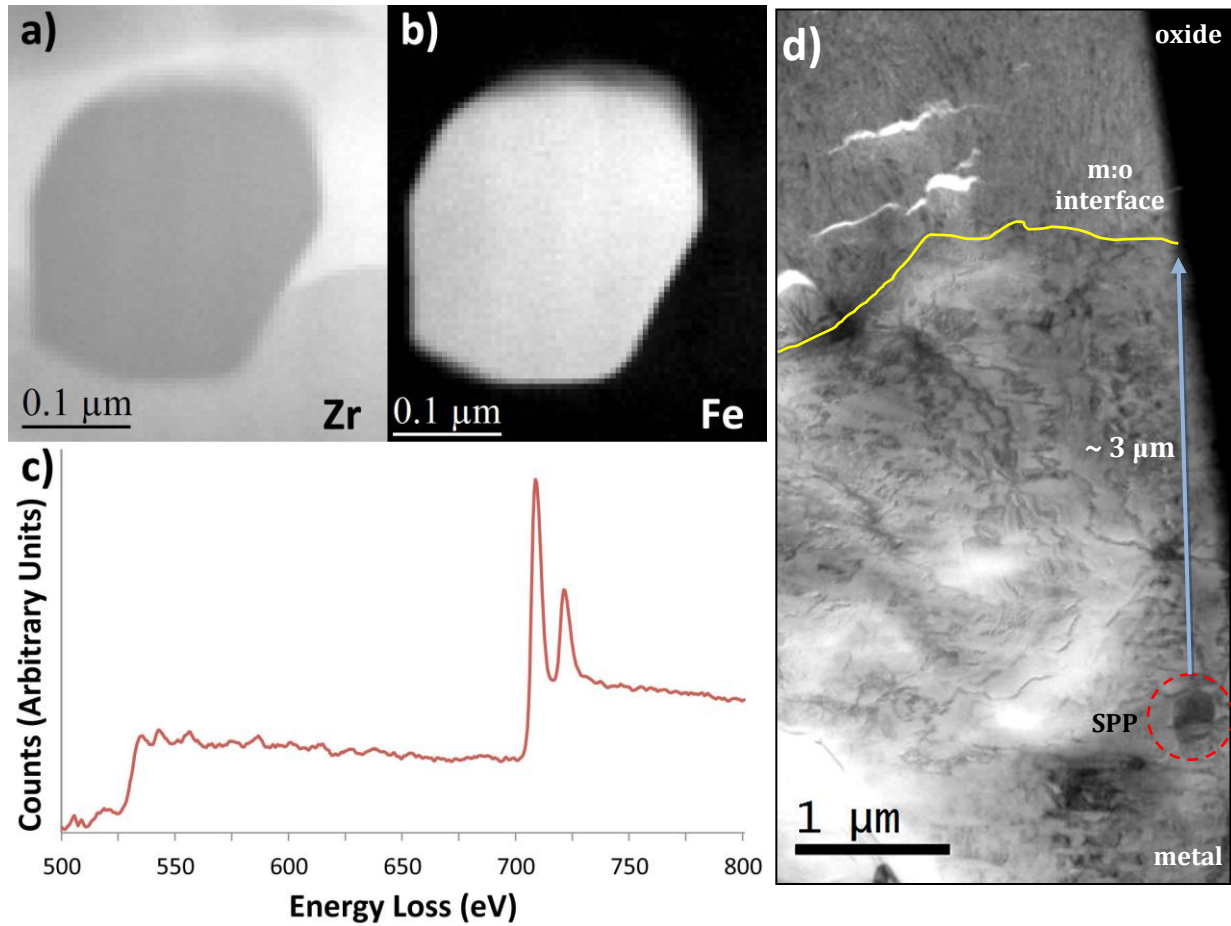


Figure 5.1: EELS spectrum imaging of a Zr_2Fe SPP in the unoxidised metal: a) map of zirconium areal density; b) map of iron areal density; c) EEL spectrum showing iron- $L_{2,3}$ edges at 721 and 708 eV respectively which depict a high Fe content within the SPP. The SPP contains no detectable Cr, as shown by the lack of the chromium- $L_{2,3}$ edges at 584 and 575 eV respectively; d) a low magnification survey image of the specimen showing the SPP embedded in the metal $\sim 3 \mu m$ from the interface.

5.3.2 Zr_2Fe SPP in oxide

As the oxidation front continues to advance through the α -Zr, secondary phase particles meeting this interface will be subject to corrosion. The oxidation front will proceed to oxidise the SPP and the surrounding material, leaving behind an oxidised SPP stranded in the oxide layer. EEL mapping, HAADF imaging, and scanned diffraction of one such oxidised Zr_2Fe SPP are shown in Fig. 5.2. This post transition specimen has an oxide thickness of $4.72 \mu m$, with the SPP found $3 \mu m$ above the metal:oxide interface, as can be seen in Fig. 5.2 f. The SPP is located just above the first transition layer of cracking in the oxide.

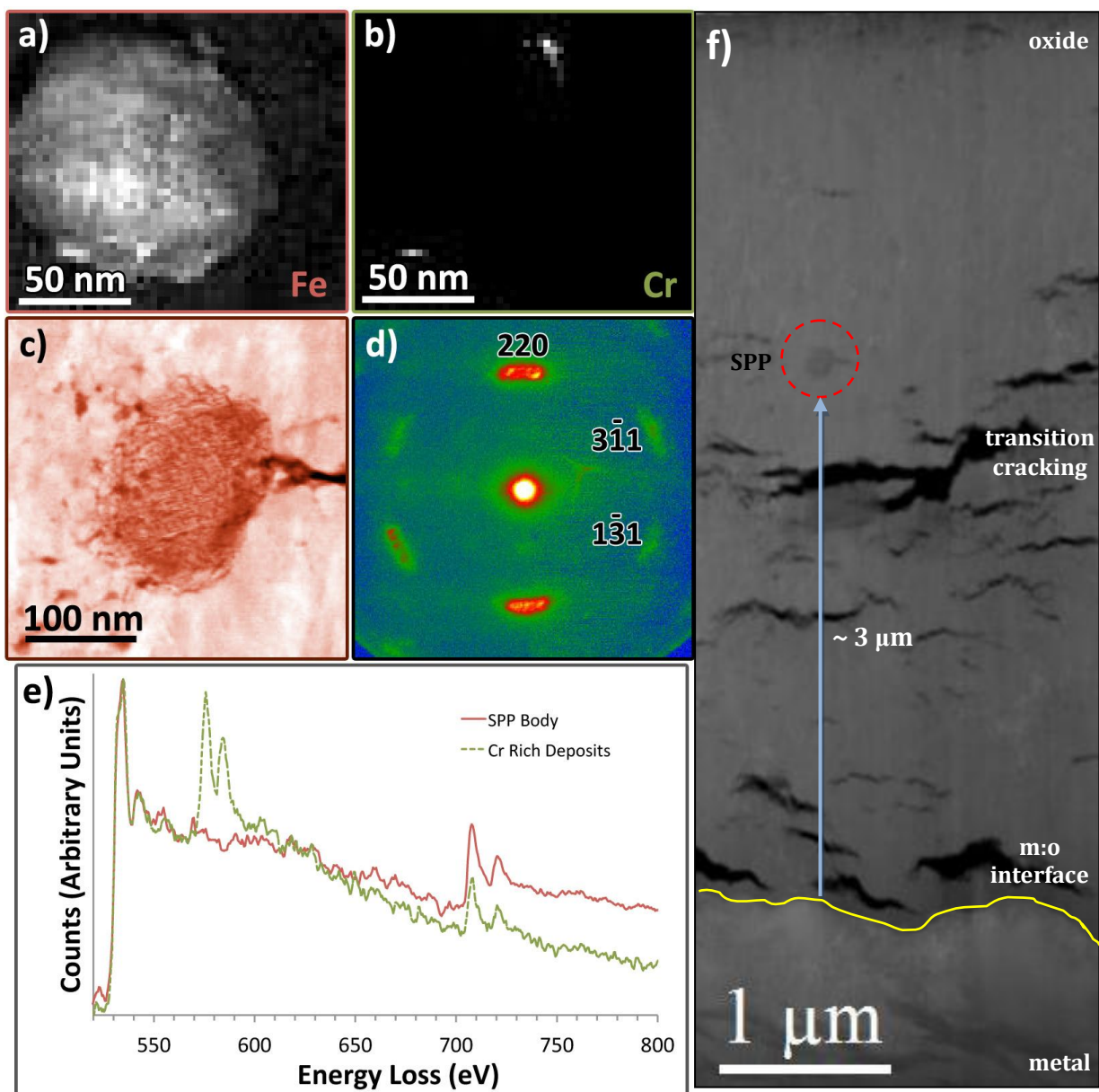


Figure 5.2: EELS spectrum imaging of a Zr_2Fe SPP stranded in the oxide post corrosion: a) map of iron areal density; b) map of chromium areal density; c) a false coloured HAADF image of a different oxidised Zr_2Fe SPP showing the nanocrystalline nature of particle; d) a diffraction pattern from a scanned diffraction experiment on the SPP shown in a), a tentative indexing on the basis of a face centred cubic unit cell is included; e) an EEL spectrum showing the SPP body (red) and areas of Cr deposits (green); f) a low magnification survey image of the specimen showing the SPP encapsulated in oxide $\sim 3 \mu\text{m}$ from the interface. The first transition region in the oxide can be seen to occur at $\sim 2.5 \mu\text{m}$ from the metal:oxide interface.

It is clear that the core of the oxidised SPP is rich in iron, as seen in Fig. 5.2a, but there is little evidence of any strong internal segregation of the iron – the variation of intensity in the iron map from centre to edge in the SPP is due to this being a ~ 100 nm precipitate fully embedded in a thin section thicker than this. Just quantifying the composition using the region of the energy loss spectrum shown in Fig. 5.2e covering the O-K and Fe-L_{2,3} edges results in the composition shown in Table 5.2. The calculated composition was achieved by doing some simple balancing of equations, based on the assumption that an ideally stoichiometric Zr₂Fe particle oxidises to a mixture of Fe₂O₃ and ZrO₂. The measured composition lies within one standard deviation of the calculated composition giving confidence that this assumption of full oxidation to Fe³⁺ and Zr⁴⁺ is likely.

Table 5.2: Chemical composition of a typical oxidised Zr₂Fe particle as determined by EELS analysis.

Element	Measured Composition (at. %)	Stoichiometric Composition (at. %)
O (K edge)	87 ± 5	84.6
Fe (L _{2,3} edge)	13 ± 5	15.4

A very small chromium-rich region can be seen at the edge of the SPP in Fig. 5.2b. Whether this arose from a separate Cr-containing SPP on the edge of the Zr₂Fe SPP, or from a small amount of Cr in the Zr₂Fe is not clear.

An HAADF image of another oxidised Zr₂Fe is shown in Fig. 5.2c. This shows a very fine, apparently nanocrystalline structure. Additionally, it appears to have expanded in the oxidation direction, but also seems to be associated with a crack in the neighbouring ZrO₂. This suggests that the expansion on oxidation for this phase and the Zr are different, leading to such cracking effects.

Fig. 5.2d shows a typical diffraction pattern from a scanned nanodiffraction dataset from the SPP also shown in Fig. 5.2a. The same diffraction pattern was seen across the particle, but with frequent small rotations of the spot pattern. Even in this pattern, whilst it is clear that it corresponds to a zone axis pattern, there are arcs of several spots for each reflection. Thus, the nanocrystallites that comprise the particle display a very strong crystallographic texture. The pattern shown could correspond to a $\langle 114 \rangle$

pattern of a cubic structure of lattice parameter 4.7 Å, and such an indexing is included on the pattern. This is unexpected, since iron doping of ZrO₂, whilst it stabilises tetragonal [154], and possibly cubic phases [155], has previously only been shown to result in lattice parameters down to 5.034 Å for Zr_{0.6}Fe_{0.4}O_y [155]. Conversely, this would also not be explained by the formation of magnetite Fe₃O₄ or maghemite Fe₂O₃ (cubic spinels with lattice parameters 8.35-8.4 Å [half the lattice parameter would be ~ 4.2 Å]). It is possible that this is a metastable hydrated phase formed at these low temperatures in superheated water and which bridges the lattice parameter gap between ~4.2 and ~5 Å for iron oxide and zirconia, but this is uncertain at this point and requires a further investigation which is outwith the scope of this thesis.

5.3.3 Zr(Fe, Cr)₂ SPP in metal

As expected, Zr(Fe, Cr)₂ precipitates were commonly observed in the metal matrix. Fig. 5.3 depicts two such Zr(Fe, Cr)₂ SPPs, which together have an average diameter of 0.3 – 0.35 µm and are not uniform in shape, but have a very definite, faceted outline. It is not uncommon to see two or more SPPs clustered together. In fact, this has been seen on several occasions throughout analysis of specimens during this study, and has also been reported by [70] when studying secondary phase particles in Zircaloy-2. Fig. 5.3 is acquired from a post transition specimen which has an oxide layer of 4.05 µm, where the SPP is located 2.8 µm from the metal:oxide interface. The size of these precipitates are consistent with the size of Zr₂(Fe, Ni) precipitates found in Zircaloy-2 by Meng *et al.* [71] (<1 µm), with a Fe/Cr ratio of 0.83. Whilst both Cr and Fe are found throughout, it should be noted that there is also some evidence of a Fe concentration within the centre of one precipitate. It may also be noted that there is a clear O enrichment at the edges of the SPPs, over and above the slight surface oxidation on the FIB-prepared specimen. It may be that some of the Cr or Zr in such particles reacts with any dissolved oxygen in the α-Zr matrix to form a thin surface oxide layer on such particles. Integrating the spectra from much of the particles and quantifying the edges yields the bulk composition shown in Table 5.3. This is very much as expected for Zr(Fe, Cr)₂.

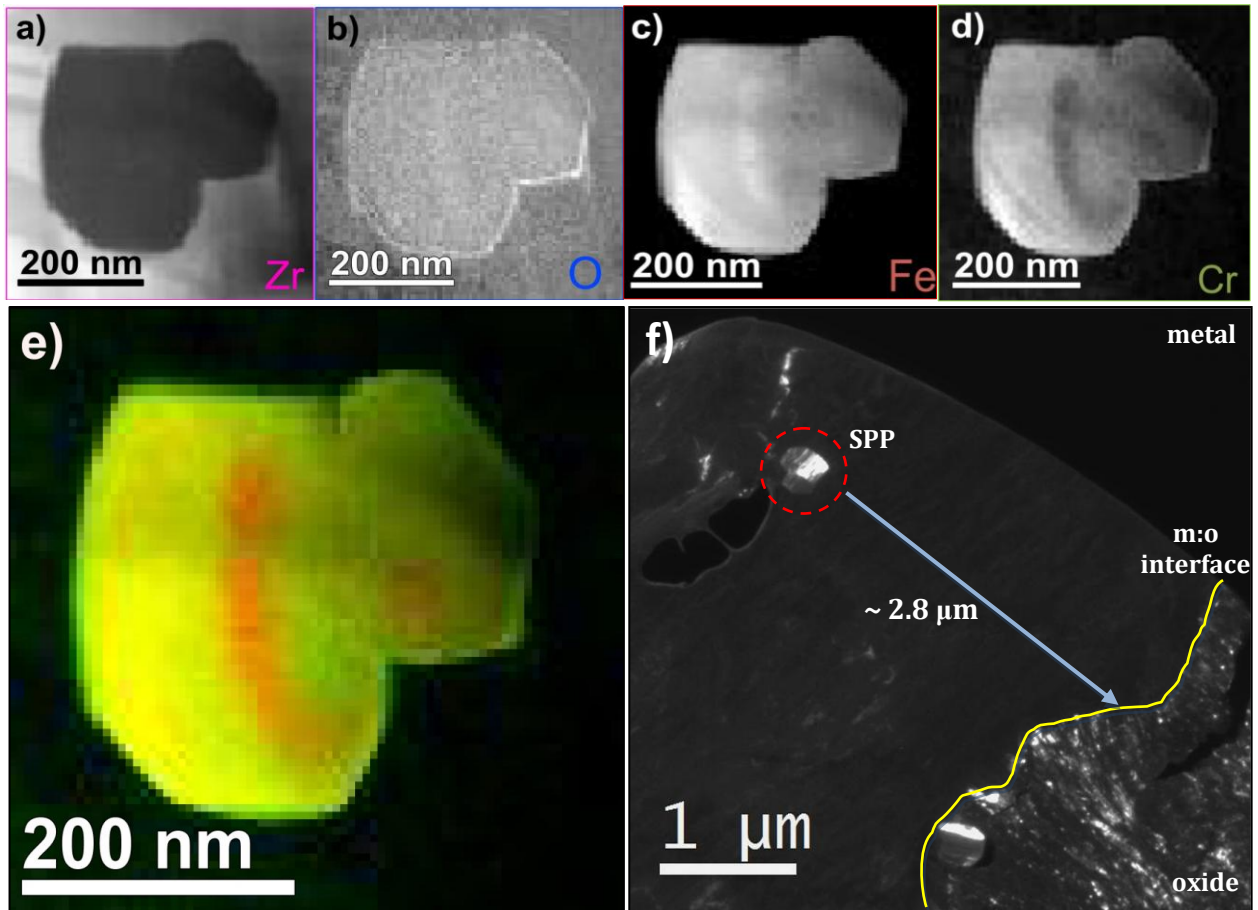


Figure 5.3: High-loss quantification of $Zr(Fe, Cr)_2$ SPP: a) map of zirconium areal density; b) map of oxygen areal density; c) map of iron areal density; d) map of chromium areal density; e) false colour RGB composite of SPP where green = Cr and red = Fe and f) a low magnification survey image showing the location of the SPP in the metal.

Table 5.3: Chemical composition of a typical unoxidised $Zr(Fe, Cr)_2$ particle as determined by EELS analysis.

Element	Composition (at. %)
Zr ($M_{4,5}$ edge)	34.6 ± 5
Fe ($L_{2,3}$ edge)	40.7 ± 5
Cr ($L_{2,3}$ edge)	24.7 ± 5

5.3.4 $Zr(Fe, Cr)_2$ SPP at Metal:Oxide Interface (during oxidation)

As the oxidation front advances into the metal, particles are seen which are in the process of being oxidised. It is expected on the basis of electronegativity values that the first constituent to oxidise will be the zirconium, followed by chromium and finally iron: consistent with the observations in this work

Fig. 5.4 shows an oxidised cluster of SPPs just inside the ZrO_2 scale, so the oxidation front had just moved past these precipitates when the sample was removed from the autoclave and prepared for STEM analysis. This post transition specimen has an oxide thickness of $2.96\ \mu\text{m}$ as calculated from weight gain measurements, and is located in the oxide, just at the oxide:metal interface. Overall, the majority of these particles are clearly rich in Cr and appear to be the $Zr(\text{Fe}, \text{Cr})_2$ type which has/have been at least partially oxidised. Whilst Fe is found throughout, it is clearly segregated strongly to bands within the particle. There is Cr throughout much of the particle, but there are some particularly rich areas at points. Wherever Cr is rich, there is also plenty of Zr (although naturally much less than in the pure ZrO_2 matrix surrounding). The oxygen map shows that the Fe-rich veins are very low in O, and also the areas closest to the unoxidised metal are very low in oxygen. A crack is observed intersecting with the particle to the top right, especially visible in this oxygen map, as previously also noted for the oxidation of $Zr_2\text{Fe}$.

Integrating the spectra from much of the two $Zr(\text{Fe}, \text{Cr})_2$ particles and quantifying the edges (as detailed in Chapter 3) yields the bulk composition shown in Table 5.4. This is reasonably consistent with the bulk cation composition for an unoxidised particle shown in Table 5.3, although a little high in Zr, however, there may have been some ZrO_2 matrix overlapped with the edges of the SPP. The oxygen:metal content is only 1:1, rather than 3:2 for Cr oxide or 2:1 for Zr oxide, suggesting that this particle is nowhere near totally oxidised.

Table 5.4: Chemical composition of a typical oxidised $Zr(\text{Fe}, \text{Cr})_2$ particle as determined by EELS analysis.

Element	Composition (at. %)
Zr ($M_{4,5}$ edge)	19.7 ± 5
O (K edge)	50.2 ± 5
Fe ($L_{2,3}$ edge)	19.1 ± 5
Cr ($L_{2,3}$ edge)	11.1 ± 5

Four regions highlighted in Fig. 5.4e have been selected, and their low- and high-loss EEL spectra shown in Fig. 5.4f and 5.4g respectively.

The region at the bottom centre of the oxidised SPP highlighted with a blue dot in Fig. 5.4e is unlike most parts of the SPP and shows almost no Cr, and low Fe content compared to the rest of the oxidised SPP. The low-loss which represents this (region 1 in Fig. 5.4f) shows a three peaked spectral signature, typical of an oxide (the highest peak being associated with the $N_{2,3}$ edge of Zr). The high-loss spectrum for this area (region 1 in Fig. 5.4g) confirms the oxidation of this area showing a strong peak of oxygen at 532 eV. The Fe $L_{2,3}$ edge is also present, however, there is no detectable Cr within this area of the SPP. This leads to the assumption that this area is an oxidised small Zr_2Fe precipitate, which was originally neighbouring a cluster of $Zr(Fe, Cr)_2$ SPPs prior to oxidation.

The orange dot in Fig. 5.4e highlights one of the Fe-rich veins in the SPP, and low- and high-loss spectra are shown as region 2 in Figs. 5.4f and 5.4g. The low-loss EEL spectrum has just a single plasmon peak at about 25eV, entirely consistent with a metal (and in a similar position to that for pure iron [156]). The high-loss signature for this area confirms that there is minimal oxygen content over and above surface oxide in this area, as well as little Cr content. As Fe is the final constituent to oxidise according to the electronegativity argument presented above, it appears that the Cr and Zr have monopolised the oxygen supply during corrosion resulting in the segregation of separate veins of metallic iron. The fact that many of these bands run perpendicular to the corrosion direction suggest that Fe is rejected by the growing oxide until it builds up into a sufficient concentration to precipitate separately, and that this process repeats itself multiple times in oxidation of such an SPP. This particular vein, however, runs at an angle to the growth direction, and it is speculated that this could have originally marked the boundary between two neighbouring $Zr(Fe, Cr)_2$ SPPs.

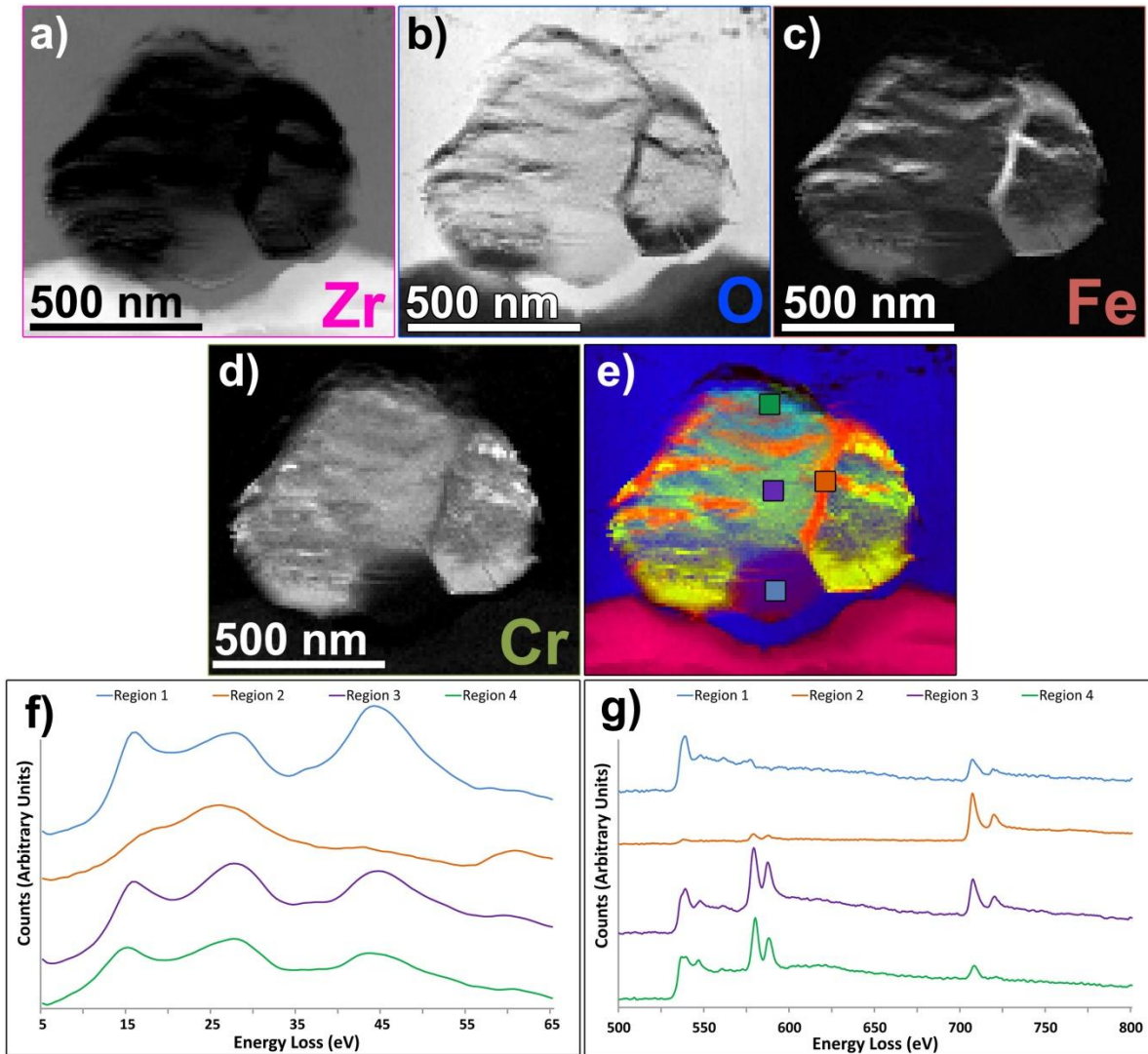


Figure 5.4: High-loss quantification of $Zr(Fe, Cr)_2$ precipitate at oxidation front showing: a) map of zirconium areal density; b) map of oxygen areal density; c) map of iron areal density; d) map of chromium areal density; e) RGB composite of all phases where pink = Zr, blue = O, red = Fe and green = Cr, with 3 areas highlighted and their corresponding; f) low-loss and; g) high-loss spectral signatures.

Much of the SPP is dominated by the mixed, Cr, Zr oxide. Representative spectra of this phase are taken from the area highlighted in Fig. 5.4e in purple and shown as region 3 in Figs. 5.4f and 5.4g. As for other oxide areas, a 3-peak structure is seen in the low-loss. Here, the high-loss spectrum demonstrates an oxidised region containing Cr, some Fe (and some Zr, not shown in this spectrum).

An area on the tip of the SPP is highlighted with a green dot in Fig. 5.4e with spectra shown as region 4 in Figs. 5.4f and 5.4g, whose low-loss EEL spectrum shows a composition somewhere between the oxidised regions 1 and 3, and the Fe-rich metallic region 2. The high-loss spectrum is principally chromium oxide, with little Fe. This is consistent with Cr being one of the first constituents to oxidise, resulting in a Cr rich SPP

tip (since this area would have been the first region of the SPP to come into contact with the metal-oxide interface).

The partial oxidation of precipitates, leading to Fe-rich veined structures within the particle has been observed within this project on multiple occasions in Zircaloy-4 specimens. One further example of this is shown in Fig. 5.5.

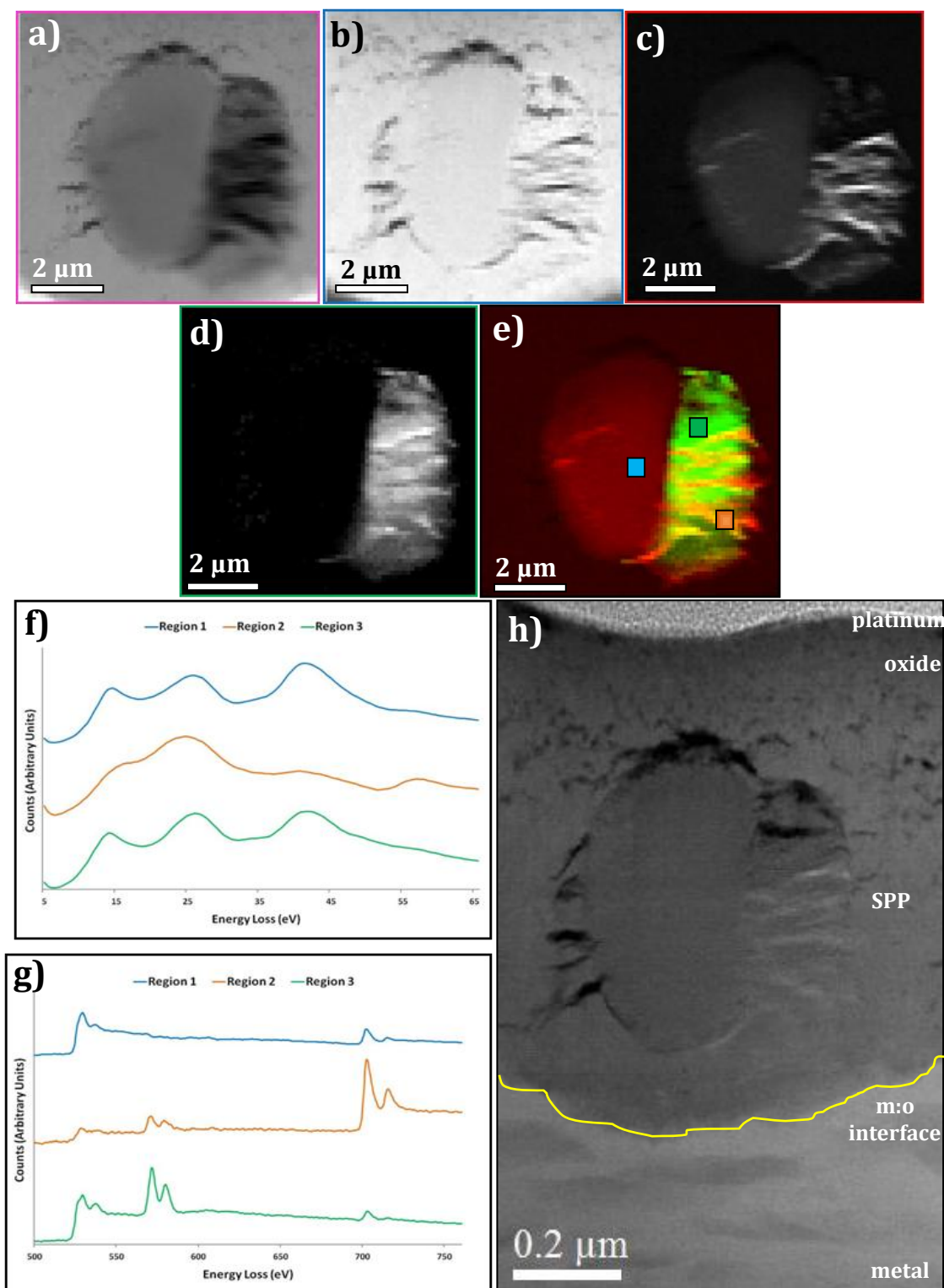


Figure 5.5: High-loss quantification of $Zr(Fe, Cr)_2$ precipitate at oxidation front showing: a) map of zirconium areal density; b) map of oxygen areal density; c) map of iron areal density; d) map of chromium areal density; e) RGB composite of all phases where red = Fe and green = Cr, with 3 areas highlighted and their corresponding; f) low-loss and; g) high-loss spectral signature, and; h) low magnification survey image of SPP showing distance to metal:oxide interface.

5.3.5 $Zr(Fe,Cr)_2$ SPP in oxide

Fig. 5.6 shows maps and scanned diffraction from a $Zr(Fe, Cr)_2$ particle $\sim 0.9 \mu\text{m}$ from the metal:oxide interface, within a $2.96 \mu\text{m}$ oxide. The structure seen here is totally consistent with the process that was seen as starting in Figs. 5.4 and 5.5. The segregation of Cr and Fe within the particles has continued to produce the very banded structure shown in Figs. 5.6a-d and f. As before the majority is a Zr and Cr rich oxide, interspersed with Fe-rich, oxygen-poor bands. As for the other precipitates, cracking can be seen at the tip of this precipitate.

Again, three regions of interest were selected to allow more detailed examination of the spectra, and these areas are highlighted by dots in Fig. 5.6f, with their corresponding low- and high-loss electron energy loss spectra shown in Figs. 5.6h and 5.6i, respectively.

The region highlighted in blue in Fig. 5.6f (the 'vein' in Fig. 5.6h and 5.6i) selected only the contributions to the data set coming from the Fe-rich banding and the low- and high-loss spectral signatures of the bands lying within the SPP shown. Here, the low-loss EEL spectrum shows more of a third peak at lower energy, suggesting some oxidation, but not as strong as in some full oxides shown in Fig. 5.4f. The high-loss spectrum shows an oxygen K-edge, a weak Cr-L_{2,3} edge, and a strong Fe-L_{2,3} edge. This suggests that the phase is still iron-rich, but contains more oxygen than immediately after the oxidation front passed through, as for the data shown in Fig. 5.4. Diffraction patterns from the scanned diffraction dataset of such regions all look similar to Fig. 5.4g, with a strong crystallographic texture, such that there are just slight rotations of this pattern. The spots shown are the 110 reflections of bcc iron, demonstrating that these areas are still principally metallic iron, albeit with more dissolved oxygen content than earlier in the oxidation process

A representative region within the Cr, Zr-rich body of the SPP is shown with a red dot in Fig. 5.6f which gives the spectra shown in the spectrum titled 'body' in Figs. 5.6h and 5.6i. This shows an SPP body which is rich in Cr and O (and Zr, not shown in the spectrum), and which is also deficient in Fe. Fig. 5.6e shows a representative diffraction pattern from a scanned nanodiffraction dataset of the body of the SPP. This mainly displays diffuse rings of intensity at an angle corresponding to a plane spacing of 2.73 \AA . This ring is better defined than a typical amorphous diffraction ring, but the individual

spots are difficult to resolve in most cases, suggesting that this material is composed of extremely small nanocrystals, of just a few nm in size. This ring at 2.73 Å could correspond to diffraction from $\{10\bar{1}4\}$ planes in Cr_2O_3 (the strongest reflection from this structure in X-ray diffraction). Thus, the phase could be interpreted as mainly nanocrystalline Cr_2O_3 . There are also reflections for monoclinic ZrO_2 in this area, which could also contribute to the ring.

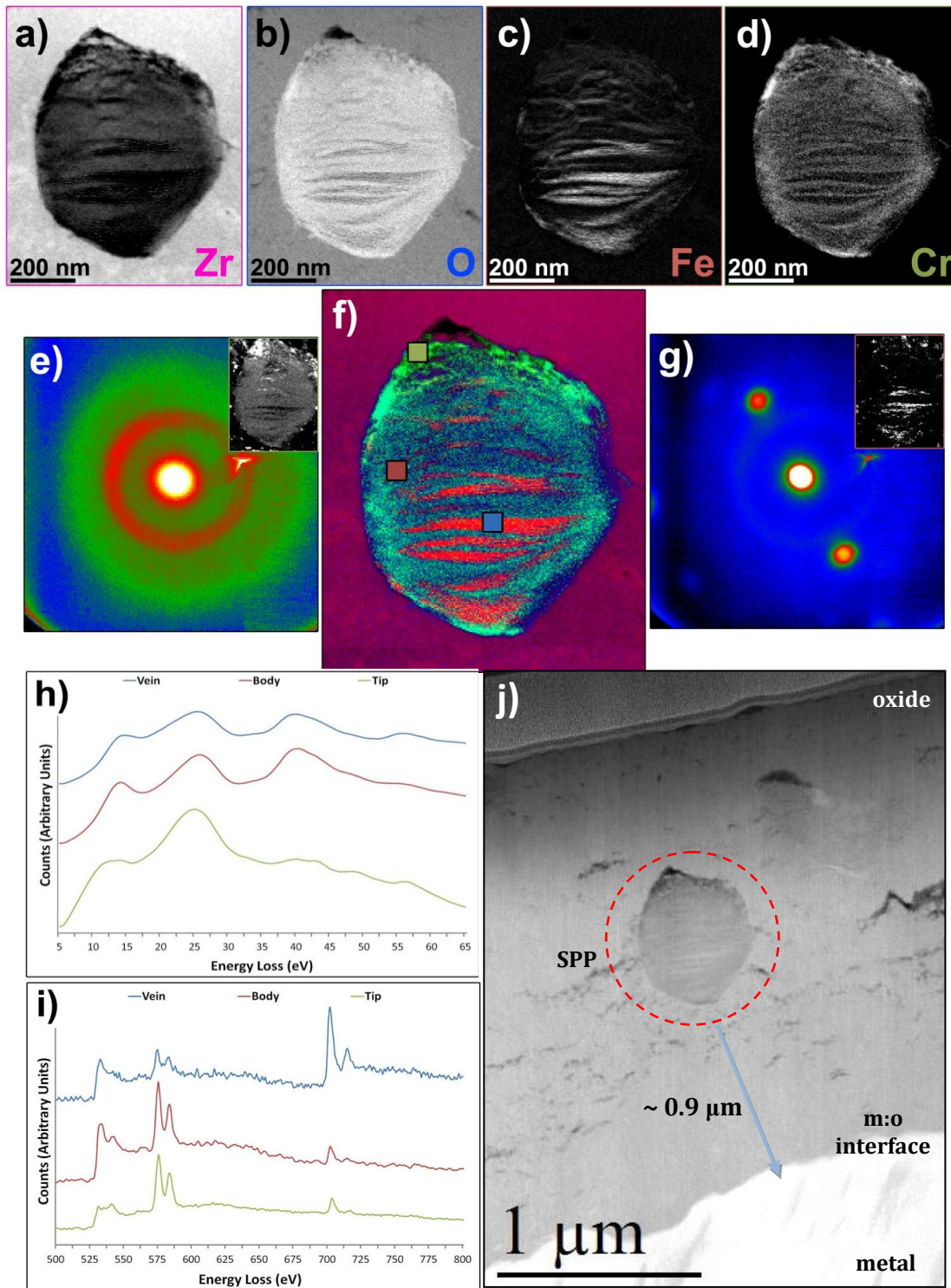


Figure 5.6: High-loss quantification of $Zr(Fe, Cr)_2$ precipitate encapsulated by oxide showing; a) map of zirconium areal density; b) map of oxygen areal density; c) map of iron areal density; d) map of chromium areal density; e) scan diffraction image showing diffraction pattern of body of SPP; g) scan diffraction image showing diffraction pattern of Fe-rich veins of SPP and; f) RGB composite of all phases where pink = Zr, blue = O, red = Fe and green = Cr,] with 3 areas highlighted and their corresponding; h) low-loss and; i) high-loss spectral signatures; j) a low magnification survey image of the SPP in oxide, $\sim 0.9 \mu\text{m}$ from metal:oxide interface.

Finally, the region highlighted by a green dot is shown in Fig. 5.6f (the 'tip' in Figs. 5.6h and 5.6i) was selected to include only contributions from a Cr-rich 'cap' of the precipitate (note, a Zr-rich cap is seen just above this in Fig. 5.6a). This region's high-loss spectrum is depleted in Fe, but rich in Cr and O. All this is then consistent with the theory that Zr oxidises first, shortly followed by Cr, and that the iron is pushed out of the oxide into separate regions, which never oxidise fully.

It should be noted that similar studies have been performed on Zircaloy-2 samples, and whilst full quantification of any secondary phase particles found is not provided in this thesis, quantification of high loss edges depict many consistencies with SPPs found in Zircaloy-4 specimens.

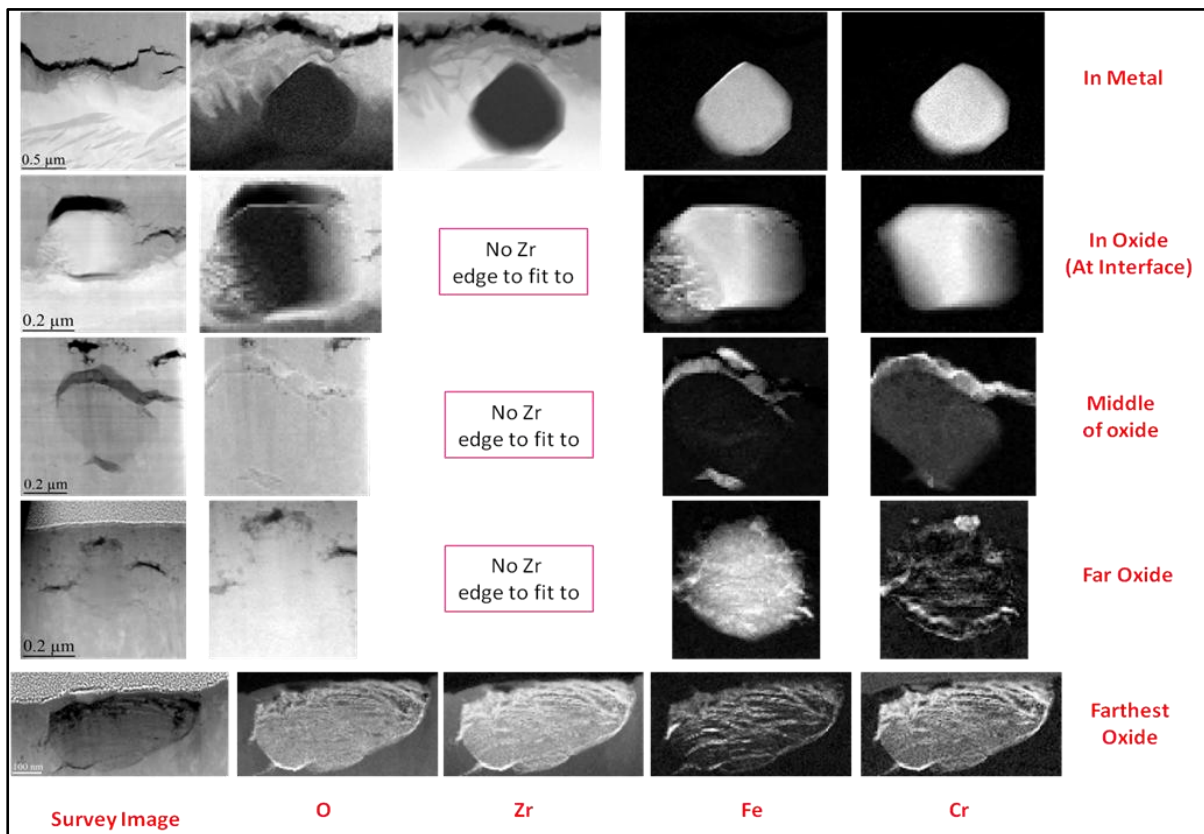


Figure 5.7: SPPs found in Zircaloy-2 material depicting all stages of oxidation, from still encapsulated by the metal matrix, right through to precipitates found at the farthest oxide (and therefore, subject to oxidation for the longest length of time). All initial mapping shows results which are consistent with findings from particles analysed within Zr-4 material.

As can be seen in Fig. 5.7, $Zr(Fe, Cr)_2$ precipitates have been found in Zr-2 specimens, where they begin as fairly round, homogenous precipitates. They are then seen to begin oxidising at the metal:oxide interface, showing some regions of preferential oxidisation

on the left of the SPP. As in Fig. 5.4 – 5.6, it can be seen in Fig. 5.7 that the Fe begins to preferentially oxidise out into veins, running parallel to the metal:oxide interface, leaving behind a Cr-rich body, which has limited oxygen content. The oxidation of these precipitates can then be mapped through the oxide layer, depicting their morphology from the middle of the oxide, right out to the farthest oxide, where a very fine microtextured SPP is noted, which has definite alternate bands of Fe-oxide, and Cr-oxide.

5.4 Discussion

Performing spatially resolved chemical mapping, and correlating this with the actual crystallographic structure has been shown to be essential to a complete understanding of what actually happens when SPPs in Zircalloys are oxidised. Of course, the spectroscopic mapping only became possible in recent years, as a result of major technical advances, such as fast DualEELS [114, 115]. The scanned diffraction also only became possible in recent years due to modern STEM instruments with the ready achievement of sub-nm, low-convergence angle probes [153] together with suitable CCD cameras and control software.

One of the interesting outcomes of this work is that the oxidation of the rarer Zr_2Fe SPPs is totally different to that of more common $Zr(Cr,Fe)_2$ SPPs. Specifically, the Zr_2Fe SPPs oxidise to form a nanocrystalline precipitate that appears chemically homogeneous down to the 5 nm scale, with a composition corresponding of full oxidation to Fe^{3+} and Zr^{4+} . These precipitates, however, display very strong crystallographic texture and a clear diffraction pattern throughout. The one mystery is that this diffraction pattern does not fit to either a well-known tetragonal ZrO_2 or any known Fe_2O_3 phase but seems to be possible to index to a cubic (or pseudocubic) structure with a lattice parameter close to 4.7 Å. Further work would be needed to elucidate exactly what is going on here.

In contrast to this homogeneity in the oxidation of Zr_2Fe particles, $Zr(Fe, Cr)_2$ oxidation results in huge segregation within the SPP into chromium and zirconium mixed oxide regions and metallic bcc iron regions. It is really quite remarkable that well-crystallised metallic iron is formed as a result of the corrosion process in veins parallel to the corrosion front. Presumably this happens by a mechanism whereby the Zr and Cr are oxidised into some form of mixed oxide, which does not welcome Fe in its

structure, thus the Fe diffuses away from the newly formed oxide into the unoxidised part of the SPP. This will gradually enrich in Fe until the concentration is so high that Fe is then precipitated and the crystallite grows rapidly with all the super-saturated Fe at the growth front accreting onto it to form large plate like single crystals. Once the Fe supersaturation has been precipitated, this procedure repeats itself, and this happens multiple times in oxidising a $Zr(Fe, Cr)_2$ SPP. The reader may be wondering why the Fe and Cr do not readily intermix in the oxide form, when Cr_2O_3 and Fe_2O_3 are isostructural (with the hematite/corundum structure). This is, however, well known from previous studies of the oxidation of Fe-Cr-Al alloys, where separate layers of Cr oxides and Fe/Fe oxides are found on the surfaces [157, 158]. This is to be expected when one considers the Fe_2O_3 - Cr_2O_3 phase diagram [159] where, whilst there is complete solid solubility, significant phase segregation into Fe_2O_3 -rich and Cr_2O_3 -rich phases would occur under most preparation conditions. Whilst some evidence of oxygen dissolved Fe has been found in a few precipitates in this work, (where plasmon peaks are significantly weaker than those seen for pure Fe), in most cases, Fe is seen *not* to fully oxidise. This has also been observed by other authors [69, 74, 81]. All evidence suggests that when SPPs are embedded in the oxide and oxygen supply is limited, Zr (being more electropositive than both Cr and Fe) reacts preferentially with oxygen, acting to sacrificially protect the Fe. Once Zr has been fully oxidised, Cr follows the same trend, resulting in a mixed Zr Cr oxide SPP body, with regions of metallic BCC Fe which segregates both to grain boundaries and is deposited as veins within the body of the SPP.

In all cases examined in this thesis, cracking can be seen at the edge of SPPs after oxidation. After further examination however, the cracking patterns around Zr_2Fe precipitates are different to those around $Zr(Fe, Cr)_2$ precipitates. Oxidised Zr_2Fe particles typically show lateral cracking in the ZrO_2 to one or other side of the SPP. In contrast to this, $Zr(Fe, Cr)_2$ precipitates typically show cracks at the top (and sometimes the bottom) of the particle. This latter tendency was not just seen in this work, but has also been seen by de Gabory *et al.* [77, 160], Proff *et al.* [69], and Pêcheur [21]. This difference can easily be explained by strain arguments. As the ratio of the molar volumes of zirconium (Zr) to zirconia (ZrO_2) (denoted the Pilling-Bedworth number) is in the range 1.48-1.56 [161-166], the resulting oxide film must expand on oxidation [167]. This results in the production of a stress gradient across the oxide, which appears at a maximum at the metal:oxide interface and a minimum at the oxide:gas

interface [168]. We calculate a Pilling-Bedworth ratio of 1.51 based on published lattice parameters [169, 170]. If Zr_2Fe is fully oxidised to a mixture of ZrO_2 and $\alpha-Fe_2O_3$, this Pilling-Bedworth number would be 1.67 (using $\alpha-Fe_2O_3$ parameters from [171] and Zr_2Fe parameters from [172]). This number may change slightly for a mixed Zr,Fe oxide, but would likely still exceed 1.51. Seeing as, to a first approximation, oxidation could be seen as a linear process happening along the surface normal direction (and not an isotropic expansion, as suggested by Proff *et al.* [166], full oxidation of a Zr_2Fe particle would result in the particle being in compressive strain along the growth direction and the surrounding matrix being in tensile strain along that same direction. This would have the effect of opening cracks in the ZrO_2 perpendicular to the growth direction, exactly as observed.

Now for the case of $Zr(Fe, Cr)_2$ SPPs, the volume expansion of full oxidation to a mixture of $m-ZrO_2$, Cr_2O_3 and $\alpha-Fe_2O_3$ should give a Pilling-Bedworth ratio of about 1.89 (based on published lattice parameters used above and for Cr_2O_3 from [173]) which would again result in the SPP being in compressive strain and the adjacent ZrO_2 in tensile strain; this is similar to that for pure $ZrCr_2$ of 1.78 [166]. But, these SPPs are not fully oxidised. In fact, the conclusions are that much of the Fe is not oxidised and instead precipitates as metallic bcc iron. When this is taken into account, the Pilling-Bedworth ratio is much smaller, just 1.53 for all iron remaining as metal and all Zr and Cr being fully oxidised (using lattice parameters for alpha iron from [174]). This would be close enough to the 1.51 for ZrO_2 such that stress and cracking would be minimal. But, if some of the Cr was also unoxidised (e.g. dissolved in the ferrite), the Pilling-Bedworth ratio would be smaller than 1.53 and the SPP would not quite fill the void created by the oxidation of the surrounding Zr. This is exactly what is observed where small voids or cracks are typically seen at the outer tip of such oxidised Laves phase SPPs. It is also true that differences in thermal expansion could contribute to such void formation, although this has not been calculated here as that would be a more complex calculation requiring detailed knowledge of the thermal expansion behaviour of all phases involved. Nevertheless, it is believed that thermal expansion mismatches would have a minimal effect [166].

This clearly demonstrates therefore, that Zr_2Fe SPPs will inevitably result in cracking of the oxide scale due to the expansion mismatch with the Zr matrix on oxidation. Since Zr_2Fe is only believed to form at higher iron content [7], it may be that

this effect could be reduced by reducing iron content somewhat. Indeed, this could be one reason why Charquet [7] found a worse corrosion resistance for high Fe:Cr ratios in Zircaloy. This happens in addition to any cracking that appears due to mechanical mismatches resulting from the undulation of the metal-oxide interface [36].

The formation of small voids above partially oxidised $Zr(Cr,Fe)_2$ Laves-phase SPPs is probably similar to the formation of crescent shaped cracking above unoxidised SPPs in the oxide layer of Zr1%Cr samples [69] and in unoxidised or partially oxidised SPPs in other studies. This is probably less significant for the formation of connected cracking, as they are generally just some free space at the SPP imposing no tensile strain on the zirconia scale.

In summary, it has been seen that the corrosion of secondary phase particles in Zircaloy-4 is a complex, and multi-faceted process with many mechanisms occurring simultaneously. With the ability to fast-map each SPP and perform spectroscopic imaging as has been performed in this chapter, an improved understanding of the microscopic details of corrosion of both Zr_2Fe and $Zr(Fe,Cr)_2$ precipitates within Zircaloy-4 can be achieved. Probing small scale cracking (voids) around SPPs has allowed for the development of an understanding of expansion of SPPs upon oxidation. This in turn, has allowed for correlation of oxidation and larger scale cracking of the oxide scale.

“Even in this world more things exist without our knowledge than with it and the order in creation which you see is that which you have put there, like a string in a maze, so that you shall not lose your way.”

— Cormac McCarthy

chapter

6

Oxygen Content Through Oxide Thickness

Since the 1930s [175] it has been realised that zirconium, alongside the other group IVB transition metals titanium and hafnium, has the capacity to dissolve excessive amounts of oxygen in interstitial solid solution. Previous studies have shown that the solubility of oxygen in hexagonal, close-packed α -zirconium in the temperature region 400 – 800 °C is just less than 30 at. % (Holmberg *et al.* [176] quote 28.6 at. % ($\text{ZrO}_{0.40}$), whilst Domagala *et al.* [177] quoted a value of 28.3 at. %). This is shown schematically in an equilibrium phase diagram for the Zr-O system [55] in Chapter 1 Fig. 1.7.

As can be seen in Fig. 1.7, during exposure of Zr to an oxidising environment, an oxygen concentration gradient develops from the surface into the metallic bulk. When the solubility limit is attained, a surface oxide scale begins to develop. This is also seen in a schematic of oxide growth on a zirconium metal in Chapter 1 Fig. 1.4. This oxide is highly stressed as a result of the lattice mismatch between the oxide and the metal. Thermal expansion differences between the oxide scale and the metal also contribute [168]. As the ratio of the molar volumes of ZrO_2 to Zr (denoted the Pilling-Bedworth number and discussed previously in Chapter 5) is 1.56 [161], the resulting oxide film becomes compressed [167]. This results in the production of a stress gradient across the oxide, which appears at a maximum at the metal:oxide interface and a minimum at the oxide:gas interface [168]. As a result of these high compressive stresses, the metastable tetragonal non-stoichiometric Zr-based oxide is then stabilised at the metal:oxide interface [48, 178] since this has a smaller molar volume and thus Pilling-Bedworth number than monoclinic ZrO_2 . In order to relieve stress on the oxide, the tetragonal to monoclinic phase transformation occurs a little away from from the metal:oxide interface. This transformation has a volume expansion of around 7% and may create defects such as cracks and pores [178] in the oxide. Due to the brittle nature of the oxide, this volume expansion results in a number of hairline cracks just at the tip of the larger crack, which propagate parallel to the neutral stress axis in the oxide [2]. The production of several smaller cracks will result in a blunting of the larger crack tip, and will prevent further cracking [178], leaving behind a thick un-cracked inner barrier layer [2]. As yet, there is little published literature directly commenting on oxygen levels present at different regions around a crack. Specifically this study directly links the level of oxygen present, to the presence of cracks within the oxide scale.

6.1 Microscopy of the Oxide Scale

Three specimens of Zircaloy-4 which have undergone corrosion in pressurised water at 360 °C have been analysed in this chapter. In particular, mapping of the chemistry of these sections of oxide by electron energy loss spectroscopy spectrum imaging using DualEELS to produce spatially resolved quantitative maps of elemental content with few nanometre resolution has been performed. The details of this instrumental set up can be read about in Chapters 2 and 3 of this thesis. All samples were as standard, prepared by AMEC Foster Wheeler and samples lifted out using an FEI Nova Nanolab as detailed in Chapter 2 of this thesis.

Digital Micrograph was utilised in order to improve signal to noise ratio of each of the datasets by methods described previously in [116, 179, 180] and in Chapter 3 of this thesis. The 'simple math' tab in Digital Micrograph was then used in order to achieve an estimate of the oxygen percentage at all points within the dataset, based upon the assumption that the portion of the oxide directly adjacent to the immediate outer oxide was ZrO_2 , as consistent with Garner *et al.* [32] and many other studies.

6.2 Results

This chapter focuses on analysing oxygen content through oxide thickness in three specimens of Zircaloy-4. Each specimen having been corroded for varying lengths of time allowed for the comparison of three differing oxide thicknesses: $\sim 1.6 \mu m$, $2.78 \mu m$, and $4.7 \mu m$. DualEELS datasets containing both the low- and high-loss information for each thickness were acquired. The first two datasets were obtained in order to analyse oxygen content either side of a large lateral crack bisecting the SI, and a third acquired to probe oxygen content at the tip of one of these large lateral cracks.

The detailed procedure for processing and signal extraction for each dataset is described as follows. Both the low-loss and corresponding high-loss spectrum image were aligned, zero-loss centered, volume extracted and x-ray removed as detailed in section 3.6 of this thesis. Following this, Principal Component Analysis was performed on both the low- and high-loss spectrum images in order to reconstruct a noise-reduced data set, again as detailed in section 3.6 of this thesis. Subsequently, both low- and high-loss spectrum images were spliced together to form a continuous spectrum. This spectrum could then be deconvolved using the Fourier Log routine on Digital Micrograph, and both the Zr $M_{4,5}$, and O K edges extracted using the SI \rightarrow Map Signal process. Specifications of signal extraction windows for each edge were as detailed in Table 3.1. Upon extraction of a Zr and O signal, some simple math was performed in order to ensure that the O to Zr ratio was 2 for the region furthest from the metal:oxide interface (for an ideally stoichiometric ZrO_2 composition). It should be noted that although this is a general assumption resulting in relative measurements, any small fluctuations in the O concentration across the SI would not result in any alteration of the shape of the trace acquired. A SI of the total number of atoms could then be created by the addition of the scaled O and Zr signals, and an oxygen percentage content through thickness SI created by dividing the scaled O SI by the SI of the total number of atoms.

By sampling for a long time with a bright, broad beam (achieved by careful adjustment of the gun lens), the number of counts per pixel could be maximised. This, coupled with scanning across several lines in each SI and adding the signal per pixel vertically, resulted in significantly noise reduced data. An estimate of the uncertainty in the O percentage is thus deduced to be equal to the root mean square (RMS) noise on the trace. RMS noise was estimated by selecting a suitable region on the trace and calculating the average and the standard deviation, found to be 0.6 % and 0.1 % respectively.

6.2.1 1.6 μm oxide layer specimen

Fig. 6.2a shows a survey image taken across the first sample with the area selected for the spectrum image indicated by the box (left to right): this crosses through the outer oxide, through ~ 1 micron of oxide, through a substantial crack, and ~ 0.2 microns beyond to the surface of the metal. Fig. 6.2b shows a line profile of the oxygen content in this spectrum image, starting from the far left of the spectrum image, spanning the bulk oxide, the crack, and into the oxide beyond. This single pixel line profile was integrated in Digital Micrograph over the full height of the SI dataset, and therefore, is as accurate a representation of the oxygen content within this section of the oxide – the noise on the profile suggests an uncertainty of about ± 0.10 - 0.15 at. %. Of course, the crack does not give such good results as there is little material here and the oxygen and zirconium contents are therefore small and noisy, thus giving a very noisy oxygen content at the crack.

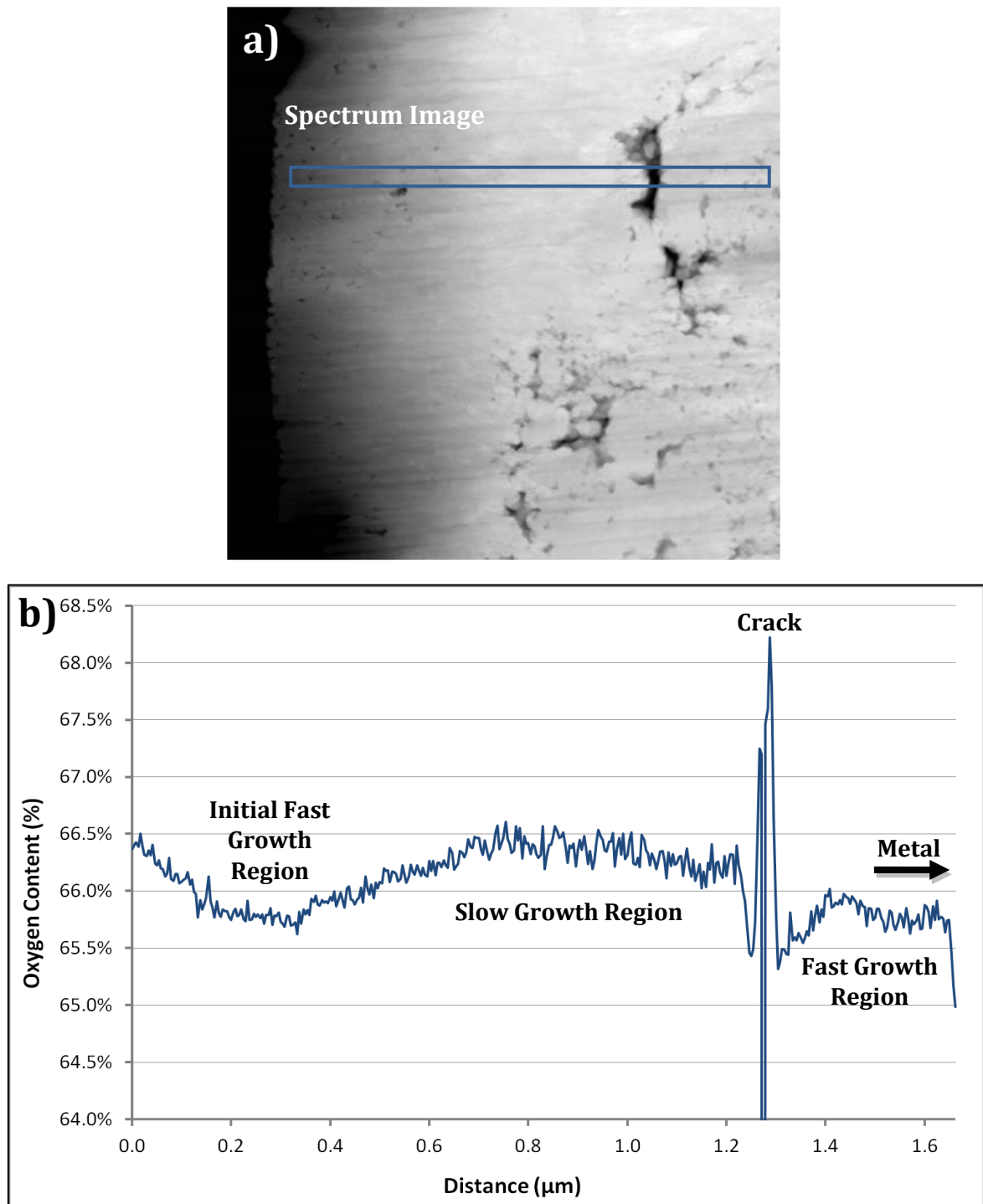


Figure 6.2: Spectrum imaging in a 1.6 μm oxide: a) A STEM survey image taken of a Zircaloy-4 specimen, where a spectrum image (SI) is acquired from the region inside the blue box. It can be clearly seen that the SI runs across a large crack; b) the oxygen content calculated from the SI running left to right.

It can be seen from the line profile in Fig. 6.2b, that the material is mostly stoichiometric at about 66.5% O at the outer surface of material, but this drops rapidly over the first 0.2 μm to a level of about 65.8% (i.e. $ZrO_{1.92}$). This region continues out

until around 380 nm, where the oxygen content then increases until around 800 nm into the oxide. At this point the oxygen content returns to what is stoichiometrically expected, and plateaus at 66.5% O until the profile reaches a crack which can be seen as a spike in the oxygen content due to the small amounts of oxygen and zirconium content within the crack, producing a noisy oxygen content signal. Post-crack, the oxide scale enters a new growth regime, with a decreased oxygen content compared to pre-crack.

By summing over a number of pixels in the corresponding deconvolved EELS spectrum image, representative spectrums of each growth region (initial growth, slow growth and fast growth) can be extracted from the SI, and plotted together on one graph as seen in Fig. 6.3. These profiles were aligned vertically by integral by selecting a region at 450 – 500 eV. This energy range represents the the atomic region of the Zr $M_{2,3}$ edge and is relatively high enough above the edge, well above the Fermi level, and into free electron states (which have little to do with which changes in compound structure). Thus, this region is a sensible choice to perform normalisation of the data. The Zr M and O K edges are also shown as insets of this figure to show finer detail of both the Zr M and O K edges.

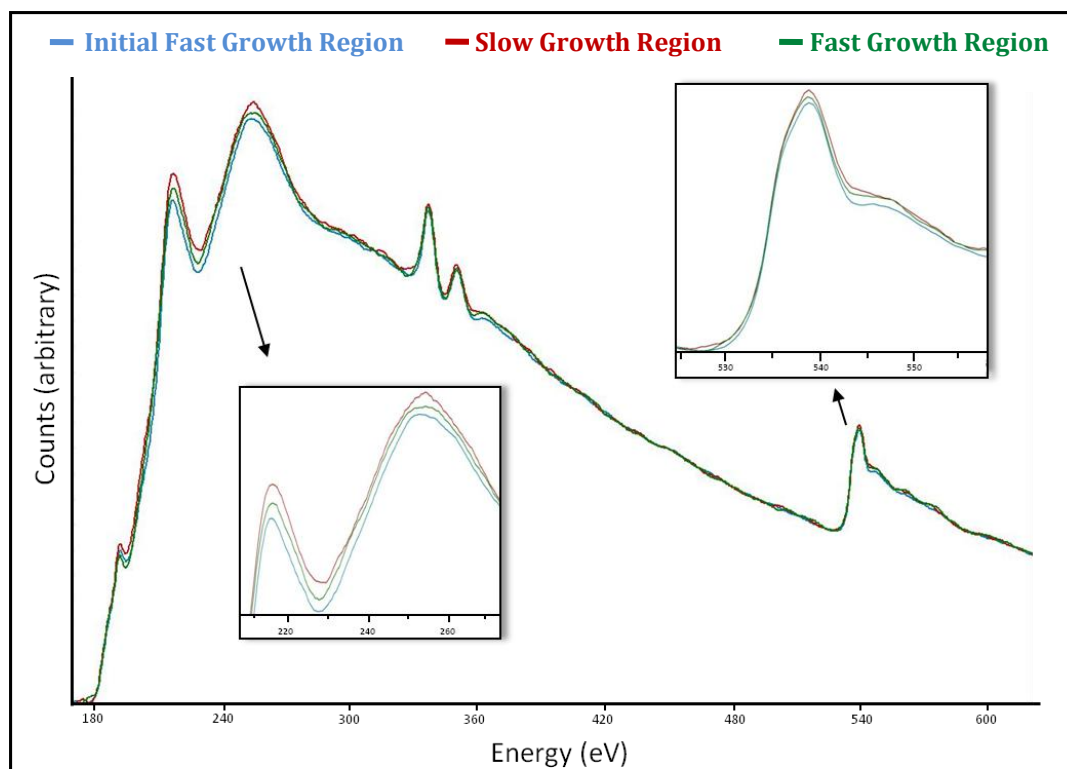


Figure 6.3: Three extracted EELS profiles from the initial, slow, and fast growth regions as shown in Fig. 6.2. The Zr M and O K edges can also be seen as insets to this figure.

As can be seen in Fig. 6.3, the slow growth region shows a relatively higher O K peak, suggesting that this area does have higher oxygen content in comparison to the initial fast and slow growth regions. Moreover, a clear change in the near edge structure of the Zr M_{4,5} edge can be seen. An increase in this pre peak in the slow growth profile may indicate oxidation effects taking place, and caused due to the creation of holes just above the Fermi level, resulting in a sharpening of near edge features.

6.2.2 4.7 μm oxide layer

A larger scale map spanning the entire 4.7 μm oxide was taken of a second Zr-4 sample, as can be seen in Fig. 6.4. The line profile (Fig. 6.4c) taken across the spectrum image in Fig. 6.4a highlights that after the initial stoichiometric outer oxide region as seen in Fig. 6.2, there is a region of around 1 micron which is uniformly constant, depicting an oxygen content which is indicative of a ZrO₂ composition. This region is also principally void of cracking. The oxygen content then rapidly falls off at around 2 microns as seen in Fig. 6.4b, where the profile reaches the lateral crack. The oxygen percentage inside the crack falls to ~ 64.5 at. %, depicting that there is still a significant amount of oxygen within the crack, and the crack does not span the full thickness of the specimen. A significant amount of noise is present in this dataset, again due to very little material being present within the crack, producing large amounts of noise in this area, however, there is still a clear delineation of the crack region. Post crack, the oxygen content is seen to recover to a value of ~ 65.5 at. % (1% less than prior to the crack, consistent with a decreased oxygen content post crack as seen in Fig. 6.2). From 3 – 5 μm , this profile then follows a sharp decline in oxygen content.

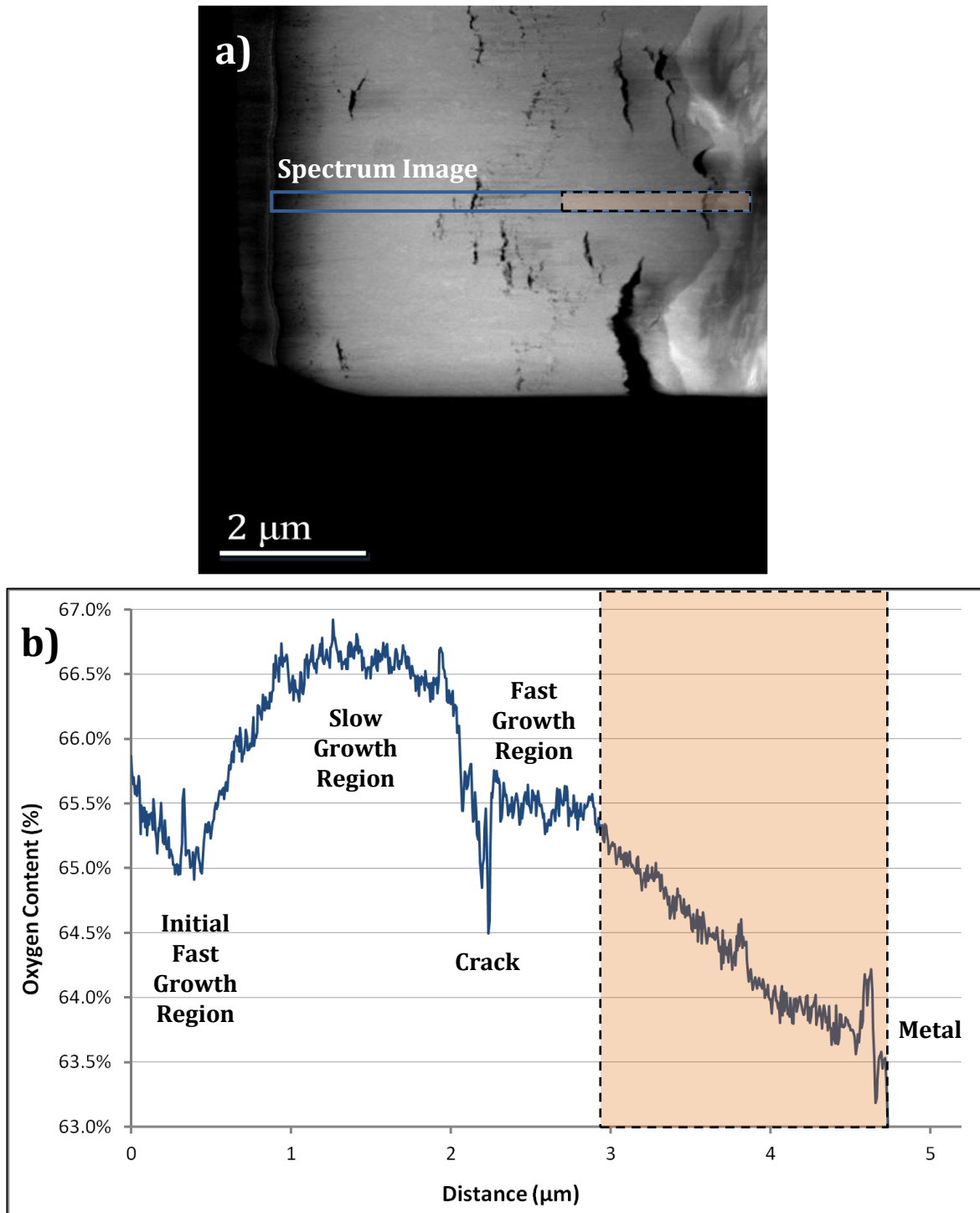


Figure 6.4: a) Spectrum imaging in a $4.7 \mu\text{m}$ oxide: a) A STEM survey image taken of a Zircaloy-4 specimen, where a spectrum image (SI) is acquired from the region inside the blue box. It can be clearly seen that the SI runs across a large crack; b) the oxygen content calculated from the SI running left to right.

6.2.3 2.78 μm specimen

A third specimen with an oxide thickness of 2.78 μm , showing a large crack under a significant undulation in the metal:oxide interface was mapped at 80 kx magnification. This time, the spectrum image (Fig. 6.5a) was acquired with the SI just picking up the edge of a large crack, as opposed to the crack completely bisecting the SI. This resulted in a line profile which can be seen in Fig. 6.5b. The oxygen percentage across the entire SI is shown in order to highlight that the expected oxygen content within the suboxide and oxygen saturated metal regions are observed. It can be seen from Fig. 6.5b that there is the usual oxygen enrichment at the beginning of the profile, which reaches a stoichiometry of 66.6 at. % in the uncracked region of the outer oxide. Oxygen content then drops to 65 % in the fast growing region of the oxide, before gradually increasing in Oxygen content around the crack region. The O percentage then proceeds to drop steeply, to a composition of ~ 50 at. % in the suboxide region, and again to a level of 35 at. % in the oxygen containing Zr metal, which gradually decreases as the line profile moves into the bulk metal. These oxygen levels are consistent with what was found both for the ZrO (suboxide), and Zr(O) (oxygen saturated metal) phases, as reported in Chapter 4 of this thesis, thus, reinforcing confidence in processing this data based on the bulk oxide having a composition of ZrO_2 .

The region shown in the orange box in Fig. 6.5b is placed underneath this in Fig. 6.5c, but at a higher magnification, in order to show undulations of this region in sufficient detail for interpretation. Here, it can be seen that the oxygen content varies between 65 at. % and 65.5 at. % in the region of the oxide void of cracks, and, when the profile passes through the crack (at $\sim 1.4 \mu\text{m}$) and beyond, the oxygen content is seen to *increase* slightly to ~ 66 at. %.

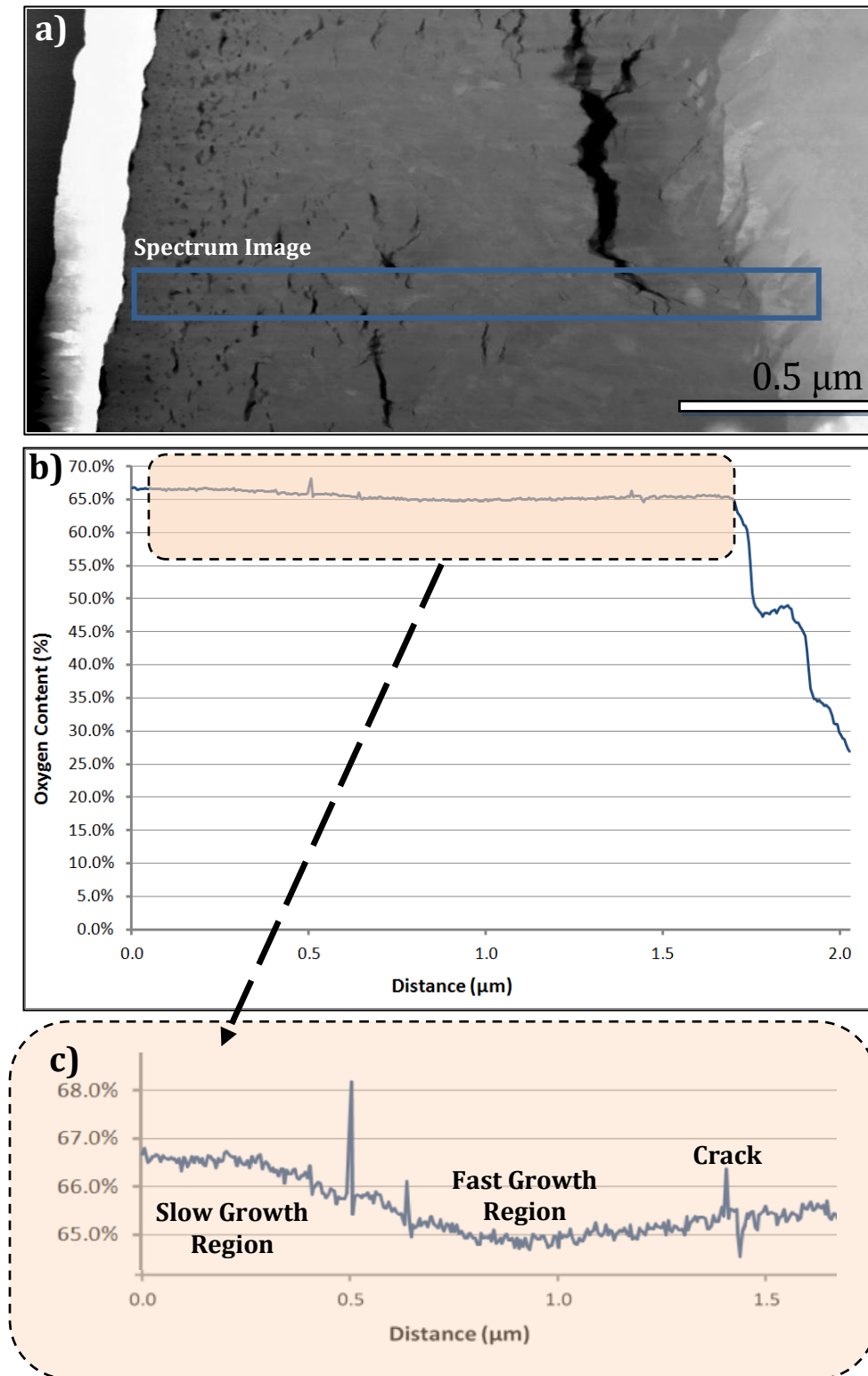


Figure 6.5: a) Spectrum imaging in a 2.78 μm oxide: a) A STEM survey image taken of a Zircaloy-4 specimen, where a spectrum image (SI) is acquired from the region inside the blue box. It can be clearly seen that the SI runs across the tip of a large lateral crack; b) the oxygen content calculated from the SI running left to right showing the 50 at. % O suboxide region and the 33.3 at. % oxygen saturated metal region; c) A further magnified section of the profile in the oxide, showing the O enriched outer oxide, the plateau region of ~ 65.5 at. % O in the region of uncracked oxide scale, and the oxygen elevated region surrounding the tip of the larger lateral crack.

6.3 Discussion

As has been discussed previously, STEM coupled with DualEELS is an optimal instrumental configuration to probe oxygen content in materials utilised for nuclear fuel containment [34, 43, 128, 160, 180]. However, to date there is little literature available which investigates quantitative oxygen content throughout the oxide scale in Zircaloy-4 specimens, particularly around crack locations within the oxide. With the application of STEM and DualEELS to this problem, it has been possible to confirm a clear and consistent trend of oxygen content variation through the oxide scale. Comparison of three separate samples shows strong evidence of a trend whereby there is: a) a stoichiometric surface which is in constant contact with water; b) a slightly oxygen deficient (about 1%) sub-surface in the fast grown oxide; c) a rise in oxygen content towards stoichiometry in the slow-grown oxide and; d) a repeat of the process if a large crack forms.

This observation can be seen initially in Figure 6.2 in a 1.6 μm grown oxide. The outer layer can be seen to achieve stoichiometry as a result of this region of the outer oxide being exposed to the high pressure, high temperature, aqueous environment continuously. Following this, a 65.8% plateau would suggest that during the rapid growth of this oxide, that this region does not quite achieve stoichiometry and is slightly oxygen deficient. A rapid drop in the first 200 nm from 66.5 to 65.8% would suggest that this is something like a typical diffusion profile through this rapidly grown first oxide – oxide that has previously been observed to be fairly dense with equiaxed grains and small pores [43, 48, 181]. In fact, this is exactly what is seen in Figure 6.2a – this outer layer has small pores but no extended cracks. After this low plateau at 65.8% oxygen out to about 380 nm, the oxygen content rises again up to about 800 nm, at which point the oxygen content returns to an approximately stoichiometric value. If this is compared to the oxygen growth curve, this is a point at which the oxide scale growth has slowed significantly. It seems as growth slows, that there is now enough time to form scale with a stoichiometric composition.

At some point, the oxide scale cracks and goes through a transition in growth rate [48] – and this is shown by the crack in this image. Once this happens, the oxygen supply rate to the metal-oxide interface must increase markedly and the oxide growth rate increases again. Unsurprisingly, the oxygen content drops significantly after the crack for at least 200 nm in the fast grown post-transition oxide to values of about

65.8%. This area below the crack also shows the microstructure of fine rounded pores, as would be typical of fast-grown equiaxed oxide. Finally, the oxygen content drops away steeply once the metal surface is reached.

In the 4.7 μm oxide specimen, a similar outer layer which achieves stoichiometry is seen, followed as seen previously by a fast growth region which is oxygen deficient, containing an oxygen content of ~ 65 at. %. Again, a slow growth region precedes the crack, after which, there is a fast growth region of oxide where oxygen content is seen to recover post crack to a value of ~ 65.5 at. % (1% less than prior to the crack, consistent with a decreased oxygen content post crack as seen in Fig. 6.2). This is all a similar story to the previous specimen, although the oxide thickness is almost three times as large as the 1.6 μm sample.

It can be seen at a distance of ~ 3 μm from the gas:oxide interface that the oxygen content falls away steeply from content of ~ 65.5 at. % to 63.5 at. % where the line profile moves across several microns of oxide and into the bulk metal. It is understood that this decline is due to the scattering of K-edges to high angles. As an O-K edge is scattered to higher angles than for instance, Zr-M edges, these events will be cut off by the differential pumping aperture. This image was acquired with a low magnification of 30 kx, with the zero loss peak aligned at the left hand side of the image. With such a significantly large field of view (~ 5 μm), it is inevitable that this map will be subject to beam misalignment issues if there is no de-scan corrector coils in place to compensate for this effect. A full discussion of the advantages of employing de-scan in the STEM for EELS analysis can be found in Chapter 2, section 2.10 of this thesis.

Owing to the fact that the JEOL ARM200F is not commercially available with inbuilt coils to correct for de-scan, and that as this particular dataset was acquired before de-scan was employed on this machine, it is likely that the right hand side of the spectrum suffers from non-perpendicular beam and sample interaction, causing there to be an underestimation of oxygen content in the far right region of the spectrum image. The data in Figs. 6.2 and 6.4 were acquired much more recently, and thus, are acquired at a much higher magnification to account for de-scan issues.

Analysis of the 2.78 μm specimen was then performed in order to probe the oxygen content around the tip of a large crack in the oxide. It can be seen that around the crack tip, the oxygen content *increases*. This is entirely consistent with previous work [45,

150, 182, 183], whereby cracks are reported as being easy pathways for oxygen transport, permitting the oxygen to travel laterally along the crack and into the metal adjacent to it.

An investigation by Yardley *et al.* [150], focussed on the oxidation behaviour of zirconium alloys using isotropic tracers and high resolution SIMS. It was noted in their work that significantly less ^{18}O was seen to have reached the metal:oxide interface beneath a large crack running parallel to the interface. Their Fig. 5 suggests that this may be due to the corroding species not being able to penetrate past this crack, and that the large lateral crack is an easy pathway for the ^{18}O to run parallel to the interface, as opposed to continuing through interconnected porosity in the nonprotective oxide.

Separate recent NanoSIMS analysis of deuterium distribution by Hu *et al.* [182] did not focus on quantitative studies of oxygen content around large lateral cracks, but did find that the more cracked and porous the sample, the easier it was for deuterium to penetrate down to the zirconium metal.

In another study, P. Tejland *et al.* [45] set out to analyse the origin and effect of lateral cracks in oxide scales formed on zirconium alloys. Transmission electron microscopy of the fine scale lateral cracks present in the oxide scale revealed that the formation of lateral cracks in the oxide scales of zirconium alloys is an important parameter influencing the oxidation process. They purport that cracks act as short circuits for the diffusion paths, increasing the diffusion rate. They also state that as oxygen diffusion occurs through the oxide scale in grain boundaries, as opposed to bulk diffusion, this results in oxygen diffusing along the periphery of the crack by surface diffusion. This is entirely consistent with what is seen in Fig. 6.4. Whereas before, the crack shown previously inhibited oxygen supply to the material directly adjacent to it, this spectrum image is taken right at the edge of a crack, showing that the crack is actually providing an elevated amount of oxygen to this area of the specimen.

This is also entirely consistent with a recent study by Guerain *et al.* [183] who investigated ^{18}O tracer distribution in thermally grown zirconia scales using micro-Raman imaging. They found from ^{18}O distribution maps that defects in the scale act as diffusion shortcuts, allowing easier access for oxygen to migrate to the metal:oxide interface. Moreover, they found that the ^{18}O concentration was significantly lower

above cracks, than elsewhere. This effect can be seen both in Fig. 6.2 and 6.4 of this work.

Although not found within this work, it is also worth mentioning that at a much lower density, vertical cracks have been identified within samples of Zr. These type of cracks provide the best paths for oxygen towards the metal-oxide interface [182] and have been seen separately by Hu *et al.* [182] and Yardley *et al.* [150] both show evidence of this cracking. As this type of cracking is observed very rarely, it is not believed that it is a general feature of FIB-prepared TEM samples [182].

In summary, this chapter elucidates quantitatively, the details of the oxygen content in the outer porous oxide, through the stoichiometric ZrO_2 , into any metastable suboxide layers present and into the oxygen diffused metal. As a consequence, it allows the linkage of the level of oxygen present, to the presence of cracks within the oxide scale. Understanding this is imperative in order to better understand the transport of incorporated oxygen ions through the oxide scale.

"I think and think for months and years. Ninety-nine times, the conclusion is false. The hundredth time I am right."

— Albert Einstein

chapter

7

Conclusions and Outlook

The evolution of the corrosion of Zircaloy-4 with time in 350 °C pressurised water conditions has been studied using FIB preparation of cross sections through the oxide scale followed by characterisation using DualEELS in the scanning transmission electron microscope. This section summarises the main results obtained in all chapters and presents the outlook, and potential for future work in this field.

7.1 Conclusions

Primary studies on the corrosion of the metal:oxide interface show that the low loss spectra provide a straightforward method for the mapping of phases in the complex interface region, and that the phases could be correlated with quantitative, thickness-

corrected measurements of the Zr and O content from the core-loss spectra. The details of the low loss spectra for the ZrO phase match well to recent calculations using density functional theory. Zr L_3 and L_2 edges in EEL spectra show clear systematic changes in both chemical shift and white line ratio from Zr, through ZrO to ZrO₂ and suggest a formal Zr oxidation state in ZrO of +2, which is consistent with work by Yoshitaka [56], although further work with standards would be needed to prove this unambiguously. O K near-edge structure in ZrO suggests similar oxygen coordination to that in oxygen-diffused Zr metal, which makes sense since the O positions in both O-saturated Zr metal and ZrO are in octahedral interstices in a distorted hexagonal zirconium structure and are thus rather similarly bonded and coordinated.

The mapping of the corrosion process shows that in the earlier stages of growth, the metal-oxide interface starts to roughen with variable widths of oxygen-diffused metal, thicker where growth is slower and thinner where growth is faster. At this stage, little or no ZrO is found. Close to the transition where growth is very slow, significant thicknesses of ZrO are found, with a very rough saw-tooth interface to the underlying oxygen-diffused metal, especially where oxygen supply has been interrupted by lateral cracking about the metal-oxide interface. After transition, all the ZrO is lost, the interface roughness is minimal, and there is very little oxygen-diffused Zr, all of which accords well with existing models of increased oxygen supply after transition through the formation of interconnected porosity in the oxide scale, resulting in the rapid growth of a dense oxide.

Moreover, coupled STEM imaging, DualEELS and scanned diffraction has been used to provide a comprehensive study of the oxidation of SPPs in Zircaloy-4 during corrosion in superheated water. Two main forms of SPP are found, the frequently observed Zr(Fe, Cr)₂ Laves-phase type, as well as some Zr₂Fe particles (isostructural with Zr₂Ni).

Zr₂Fe precipitates begin as fairly round, homogenous precipitates within the metal matrix, and oxidise in a fairly uniform manner, to a nanocrystalline, fully oxidised Fe³⁺,Zr⁴⁺ mixed oxide. There is a strong crystallographic texture developed in oxidation, but the crystalline phase was unidentified and neither matches tetragonal ZrO₂ nor any known phase of Fe₂O₃. Instead, the diffraction pattern was consistent with a <114> pattern of a cubic structure with a lattice parameter $\sim 4.7 \text{ \AA}$.

Zr(Fe, Cr)₂ precipitates begin as very faceted structures within the metal matrix, with O enrichment of the outside rim. Fe concentration is also seen to increase in specific areas within the centre of precipitates. Such SPPs develop into a more elongated shape upon oxidation, with a strongly banded elemental segregation. There are three phases found: i) a Cr rich cap which we presume to be Cr₂O₃ with some Fe substitution; ii) a Zr, Cr nanocrystalline oxide body with an approximate 3:2 ratio of Zr:Cr, and very little Fe content. The diffraction pattern reveals a ring pattern of randomly oriented nanocrystallites, with a rings consistent with some reflections of either Cr₂O₃ or monoclinic ZrO₂ or a mixture of the two; iii) veins of well-crystallised metallic α -Fe with low oxygen content, with a strong texture mostly running parallel to the metal-oxide interface.

The Zr₂Fe precipitates cause cracking in the vicinity because the expansion on oxidation is larger than for the Zr \rightarrow ZrO₂ reaction putting the ZrO₂ either side into tensile strain. On the other hand the Zr(Fe, Cr)₂ can leave small voids or cracks at the upper tip due to the incomplete oxidation of the iron which results in less expansion of the SPP than the Zr \rightarrow ZrO₂. Providing an understanding of the corrosion process of SPPs within Zircalloys such as has been presented in this work, which can provide elemental distribution, valence state and crystal structure, gives an understanding beyond that previously obtained on the complex corrosion that takes place. This may also provide some information on the possible influence of SPPs on the overall corrosion behaviour of Zircaloy-4 in simulated reactor conditions.

Finally, the details of oxygen content at several points in the oxide scale was elucidated, specifically, by relating semi-quantitative oxygen content to lateral cracking of the oxide. By studying three samples of Zircaloy-4, it has been found that lateral cracks appear as pathways for fast oxygen transport through the oxide.

In samples where there the lateral crack completely bisects the spectrum image, oxygen content directly above a crack (near the metal:oxide interface) is seen to drop by 0.5 – 1.0 at. % in comparison to oxygen content closer to the oxide:gas interface. It is deduced that in line with previous literature, the crack acts as an easy pathway for oxygen diffusion, and thus, the oxygen diffuses laterally along the crack direction.

This conclusion is substantiated due to analysis of a third specimen, whereby only very the tip of the crack is mapped in the through thickness oxide map. In this instance

it is noted that oxygen content increases around, and just after, the tip. This substantiates the theory that as lateral cracks provide a short circuit for oxygen to travel laterally along the crack direction, there will be an increased concentration of oxygen at this point.

Whilst understanding the role cracks have in the migration of oxygen to the metal interface, there is still limited available literature looking quantitatively at oxygen content surrounding large lateral cracks in the oxide scale. This work provides a realisation of oxygen content throughout the oxide scale in nanoscale detail, and gives an understanding not previously obtained on the complex corrosion process taking place.

Recent progressions in the development and implementation of new experimental techniques for the study of these metal alloys by EELS analysis in the STEM have been great. Combining EEL spectroscopy with imaging on a modern aberration-corrected STEM has not only allowed for the development of the understanding of the corrosion of this material at the sub angstrom level, but has provided the required technology with which to produce detailed maps of the interface, SPPs, and oxygen content throughout the oxide scale, in order to probe the mechanisms of corrosion of Zircaloy-4. This nanoanalytical approach allowed for an improvement in the understanding of several facets of the corrosion taking place, which together inform a more accurate prediction of the overall performance of this existing alloy.

7.2 Outlook and Future Work

Future work should be aimed at preparing STEM lamellae using the FIB lift-out technique on a newly installed Xenon Plasma Focused Ion Beam at Glasgow University. This equipment will allow for high volume milling at high beam currents for quick removal of large specimens which contain large oxide thicknesses. This would provide a broader view of the interface and internal cracking within the oxide layer, all whilst mitigating against Ga damage normally experienced by preparing samples using a Ga FIB (as used in this thesis). Moreover, 3D reconstruction at 25 nm depth resolution using slice-and-view over large volumes of 10s of microns³ would allow the visualisation of the 3D shape of the metal:oxide interface, the internal cracking, and the 3D distribution of SPPs in the metal and the oxide.

Furthermore, probing the oxidation state of Sn in this material could now be possible, as shown recently by MacLaren *et al.* [184] who have proven that performing high quality EELS up to above 10 keV energy losses is now possible through the realisation of optimised coupling optics between the sample and the spectrometer.

There is also the possibility to extend the techniques refined in this thesis coupled with those described above to other nuclear fuel containment alloys such as other zirconium grade alloys and/or Zr-Nb alloys. These techniques may also be useful when undertaking corrosion studies on other metals such as stainless steels or materials for chemical plants, oil pipelines or materials for other power generation systems.

1. Rickover, H., L. Geiger, and B. Lustman, *History of the development of zirconium alloys for use in nuclear reactors*. 1975, Energy Research and Development Administration, Washington, DC (USA). Div. of Naval Reactors.
2. Cox, B., *Some thoughts on the mechanisms of in-reactor corrosion of zirconium alloys*. Journal of Nuclear Materials, 2005. **336**(2): p. 331-368.
3. Azevedo, C.R.F., *Selection of fuel cladding material for nuclear fission reactors*. Engineering Failure Analysis, 2011. **18**(8): p. 1943-1962.
4. Cox, B., *The Oxidation and Corrosion of Zirconium and its Alloys: V. Mechanism of Oxide Film Growth and Breakdown on Zirconium and Zircaloy-2*. Journal of The Electrochemical Society, 1961. **108**(1): p. 24-30.
5. Cox, B., *Waterside Corrosion of Zirconium Alloys in Nuclear Power Plants*. IAEA TECDOC Series. 1998, Vienna: INTERNATIONAL ATOMIC ENERGY AGENCY.
6. Bowman, F. and D. Cubicciotti, *Use of zirconium in liquid-sodium systems*. AIChE Journal, 1956. **2**(2): p. 173-176.
7. Hudson, D., *Zirconium Oxidation on the Atomic Scale*, in *Thesis*. 2010, University of Oxford: England.
8. Gilbert, R.W., K. Farrell, and C.E. Coleman, *Damage structure in zirconium alloys neutron irradiated at 573 to 923 k*. Journal of Nuclear Materials, 1979. **84**(1): p. 137-148.
9. Cox, B., *Some thoughts on the mechanisms of in-reactor corrosion of zirconium alloys*. Journal of Nuclear Materials, 2005. **336**(2-3): p. 331-368.
10. Motta, A.T. and C. Lemaignan, *A ballistic mixing model for the amorphization of precipitates in Zircaloy under neutron irradiation*. Journal of Nuclear Materials, 1992. **195**(3): p. 277-285.
11. Jin, H.J. and T.K. Kim, *Neutron irradiation performance of Zircaloy-4 under research reactor operating conditions*. Annals of Nuclear Energy, 2015. **75**: p. 309-315.
12. Pêcheur, D., et al., *Effect of irradiation on the precipitate stability in Zr alloys*. Journal of Nuclear Materials, 1993. **205**: p. 445-451.
13. Cinbiz, M.N., D.A. Koss, and A.T. Motta, *The influence of stress state on the reorientation of hydrides in a zirconium alloy*. Journal of Nuclear Materials, 2016. **477**: p. 157-164.
14. Ells, C.E., *Hydride precipitates in zirconium alloys (A review)*. Journal of Nuclear Materials, 1968. **28**(2): p. 129-151.
15. Hardie, D. and M.W. Shanahan, *Stress reorientation of hydrides in zirconium-2.5% niobium*. Journal of Nuclear Materials, 1975. **55**(1): p. 1-13.
16. Desquines, J., et al., *Embrittlement of pre-hydrided Zircaloy-4 by steam oxidation under simulated LOCA transients*. Journal of Nuclear Materials, 2016. **469**: p. 20-31.
17. Suman, S., et al., *Hydrogen in Zircaloy: Mechanism and its impacts*. International Journal of Hydrogen Energy, 2015. **40**(17): p. 5976-5994.
18. McRae, G.A., C.E. Coleman, and B.W. Leitch, *The first step for delayed hydride cracking in zirconium alloys*. Journal of Nuclear Materials, 2010. **396**(1): p. 130-143.
19. Taylor, D.F., *Microstructural aspects of Zircaloy nodular corrosion in steam*. Journal of Nuclear Materials, 2000. **277**(2-3): p. 295-314.
20. Kuwae, R., et al., *Mechanism of zircaloy nodular corrosion*. J. Nucl. Mater. , 1983. **119**(2): p. 229-239.
21. Kuwae, R., et al., *Influence of Some Factors on Nodular Corrosion Behavior of Zircaloy-2*. Journal of Nuclear Science and Technology, 1986. **23**(7): p. 661-663.
22. Oskarsson, M., *Study on the Mechanisms for Corrosion and Hydriding of Zircaloy*, in *Department of Materials Science and Engineering*. 2000, Royal Institute of Technology: Stockholm, Sweden.
23. Kearns, J.J., *Terminal solubility and partitioning of hydrogen in the alpha phase of zirconium, Zircaloy-2 and Zircaloy-4*. Journal of Nuclear Materials, 1967. **22**(3): p. 292-303.
24. Weidinger, H.G. *Zr-Alloys, the Nuclear Material for Water Reactor Fuel. A Survey and Update with Focus on Fuel for Pressurized Water Reactor Systems*. in *7th International Conference on WWER Fuel Performance*. 2007. Albena, Bulgaria.
25. Anghel, C., *Modified oxygen and hydrogen transport in Zr-based oxides*. 2006, KTH.

26. Nakamura, S., Harada, H., Raman, S., Koehler, P. E., *Thermal Neutron Capture Cross Sections of Zirconium-91 and Zirconium-93 by Prompt γ -ray Spectroscopy*. Journal of Nuclear Science and Technology, 2007. **44**(1): p. 21-28.
27. Gulbransen, E.A., Andrew, K. F., *Oxidation of Niobium between 375°C and 700°C*. Journal of The Electrochemical Society, 1958. **105**(1): p. 4-9.
28. Yamato, M., F. Nagase, and M. Amaya, *Reduction in the onset time of breakaway oxidation on Zircaloy cladding ruptured under simulated LOCA conditions*. Journal of Nuclear Materials, 2014. **445**(1–3): p. 78-83.
29. El Kadiri, H., et al., *Transformations and cracks in zirconia films leading to breakaway oxidation of Zircaloy*. Acta Materialia, 2013. **61**(11): p. 3923-3935.
30. Proff, C., et al., *In situ oxidation of zirconium binary alloys by environmental SEM and analysis by AFM, FIB, and TEM*. Journal of Nuclear Materials, 2010. **404**(2): p. 97-108.
31. Yilmazbayhan, A., Breval, E., Motta, A. T., Comstock, R. J., *Transmission electron microscopy examination of oxide layers formed on Zr alloys*. Journal of Nuclear Materials, 2006. **349**(3): p. 265-281.
32. Garner, A., et al., *The microstructure and microtexture of zirconium oxide films studied by transmission electron backscatter diffraction and automated crystal orientation mapping with transmission electron microscopy*. Acta Materialia, 2014. **80**: p. 159-171.
33. Ni, N., Hudson, D., Wei, J., Wang, P., Lozano-Perez, S., Smith, G. D. W., Sykes, J. M., Yardley, S. S., Moore, K. L., Lyon, S., Cottis, R., Preuss, M., Grovenor, C. R. M., *How the crystallography and nanoscale chemistry of the metal/oxide interface develops during the aqueous oxidation of zirconium cladding alloys*. Acta Materialia, 2012. **60**(20): p. 7132-7149.
34. de Gabory, B., et al., *EELS and atom probe tomography study of the evolution of the metal/oxide interface during zirconium alloy oxidation*. Journal of Nuclear Materials, 2015. **462**: p. 304-309.
35. Yao, M.Y., et al., *A superior corrosion behavior of Zircaloy-4 in lithiated water at 360 °C/18.6 MPa by β -quenching*. Journal of Nuclear Materials, 2008. **374**(1–2): p. 197-203.
36. Polatidis, E., et al., *Residual stresses and tetragonal phase fraction characterisation of corrosion tested Zircaloy-4 using energy dispersive synchrotron X-ray diffraction*. Journal of Nuclear Materials, 2013. **432**(1–3): p. 102-112.
37. Moya, J.S., et al., *Zirconium oxide film formation on zircaloy by water corrosion*. Acta Materialia, 2000. **48**(18–19): p. 4749-4754.
38. Hutchinson, B. and B. Lehtinen, *A theory of the resistance of Zircaloy to uniform corrosion*. Journal of Nuclear Materials, 1994. **217**(3): p. 243-249.
39. Yilmazbayhan, A., et al., *Structure of zirconium alloy oxides formed in pure water studied with synchrotron radiation and optical microscopy: relation to corrosion rate*. Journal of Nuclear Materials, 2004. **324**(1): p. 6-22.
40. Motta A. T. , Y.A., Comstock R. J., Partezana J., Sabol G. P., Lai B., Cai, Z., *Microstructure and Growth of Oxide Layers Formed on Zr Alloys Studied with Micro-Beam Synchrotron Radiation*. Journal of ASTM International, 2005. **2**: p. 27.
41. Hutchinson, B. and L. Hallstadius, *Oxidation of Zircaloy-2 studied using a wedge-shaped specimen*. Journal of Nuclear Materials, 2013. **432**(1–3): p. 437-443.
42. Abolhassani, S., G. Bart, and A. Jakob, *Examination of the chemical composition of irradiated zirconium based fuel claddings at the metal/oxide interface by TEM*. Journal of Nuclear Materials, 2010. **399**(1): p. 1-12.
43. Hu, J., Garner, A., Ni, N., Gholinia, A., Nicholls, R., Lozano-Perez, S., Frankel, P., Preuss, M., Grovenor, C., *Identifying suboxide grains at the metal–oxide interface of a corroded Zr–1.0%Nb alloy using (S)TEM, transmission-EBSD and EELS*. Micron, 2014.
44. Palacio, C., J.M. Sanz, and J.M. Martinez-Duart, *Low energy electron emission and EELS of clean and oxidised zirconium*. Surface Science, 1987. **191**(3): p. 385-394.
45. Tejlund, P., Andrén, H., *Origin and effect of lateral cracks in oxide scales formed on zirconium alloys*. Journal of Nuclear Materials, 2012. **430**(1–3): p. 64-71.

46. Hillner, E., Franklin, D. G., Smee, J. D., *Long-term corrosion of Zircaloy before and after irradiation*. Journal of Nuclear Materials, 2000. **278**(2–3): p. 334-345.
47. Bouineau, V., Ambard, A., Benier, G., Pecheur, D., Godlewski, J., Fayette, L., Duverneix, T. *A new model to predict the oxidation kinetics of zirconium alloys in a pressurized water reactor*. in *Proceedings of 15th International Symposium on Zr in the Nuclear Industry*. 2009. Baltimore MD, USA,.
48. Garner, A., Gholinia, A., Frankel, P., Gass, M., MacLaren, I., Preuss, M., *The microstructure and microtexture of zirconium oxide films studied by transmission electron backscatter diffraction and automated crystal orientation mapping with transmission electron microscopy*. Acta Materialia, 2014. **80**: p. 159-171.
49. Glavicic, M.G., *Development and application of techniques for the microstructural characterization of hydrogen permeability in zirconium oxides*. 1998.
50. Puchala, B. and A. Van der Ven, *Thermodynamics of the Zr-O system from first-principles calculations*. Physical Review B, 2013. **88**(9): p. 094108.
51. Moseley, P.T. and B. Hudson, *Phases involved in the corrosion of zircaloy by hot water (350° C)*. Journal of Nuclear Materials, 1981. **99**(2–3): p. 340-344.
52. Bossis, P., Lelievre, G., Barberis, P., Iltis, X., Lefebvre, F., Thomas, L., Maguire, M., *Multi-scale characterization of the metal-oxide interface of zirconium alloys*, in *Zirconium in the Nuclear Industry: Twelfth International Symposium*, G.P. Sabol and G.D. Moan, Editors. 2000, American Society Testing and Materials: W Conshohocken. p. 918-945.
53. Frost, P., et al., *Isothermal transformation of titanium-chromium alloys*. Trans. ASM, 1954. **46**: p. 231-256.
54. Hickman, B.S., *The formation of omega phase in titanium and zirconium alloys: A review*. Journal of Materials Science, 1969. **4**(6): p. 554-563.
55. Selmi, N. and A. Sari, *Study of Oxidation Kinetics in Air of Zircaloy-4 by *In Situ* X-Ray Diffraction*. Advances in Materials Physics and Chemistry, 2013. **Vol.03No.02**: p. 6.
56. Yoshitaka, N., Krauss, A. R., Yuping, L., Gruen, D. M., *Initial oxidation of zirconium and Zircaloy-2 with oxygen and water vapor at room temperature*. Journal of Nuclear Materials, 1996. **228**(3): p. 346-353.
57. Ni, N., et al., *Quantitative EELS analysis of zirconium alloy metal/oxide interfaces*. Ultramicroscopy, 2011. **111**(2): p. 123-130.
58. Tejlund, P., Thuvander, M., Andrén, H., Ciurea, S., Andersson, T., Dahlbäck, M., Hallstadius, L., *Detailed Analysis of the Microstructure of the Metal/Oxide Interface Region in Zircaloy-2 after Autoclave Corrosion Testing*. Journal of ASTM International, 2011. **8**(6): p. 24.
59. Dong, Y., Motta, A. T., Marquis, E. A., *Atom probe tomography study of alloying element distributions in Zr alloys and their oxides*. Journal of Nuclear Materials, 2013. **442**(1–3): p. 270-281.
60. Tejlund, P., Andrén, H., Sundell, G., Thuvander, M., Josefsson, B., Hallstadius, L., Ivermark, M., Dahlbäck, M. *Oxidation Mechanism in Zircaloy- 2—The Effect of SPP Size Distribution*. in *Zirconium in the Nuclear Industry: 17TH International Symposium*. 2014. West Conshohocken, PA 2014.
61. Schonberg, N., *The structure of the metallic quaternary phase ZrTaNO*. Acta Chemica Scandinavica (Denmark), 1954. **8**(4): p. 627-9.
62. Bumps, E.S., H.D. Kessler, and M. Hansen, *The titanium-oxygen system*. Transactions of the American Society for Metals, 1953. **45**: p. 1008-1028.
63. Andersson, S., *The crystal structure of the so-called delta-titanium oxide and its structural relation to the omega-phases of some binary alloy systems of titanium*. Acta Chemica Scandinavica, 1959. **13**(3): p. 415-419.
64. Nicholls, R.J., Ni, N., Lozano-Perez, S., London, A., McComb, D. W., Nellist, P. D., Grovenor, C. R. M., Pickard, C. J., Yates, J. R., *Crystal Structure of the ZrO Phase at Zirconium/Zirconium Oxide Interfaces*. Advanced Engineering Materials, 2014.

65. Charquet, D., *Improvement of the uniform corrosion resistance of Zircaloy-4 in the absence of irradiation*. Journal of Nuclear Materials, 1988. **160**(2–3): p. 186-195.
66. Yilmazbayhan, A., et al., *Determination of the alloying content in the matrix of Zr alloys using synchrotron radiation microprobe X-ray fluorescence*. Journal of Nuclear Materials, 2003. **321**(2): p. 221-232.
67. Zhang, Z.G., et al., *Microstructure and tensile properties of novel Zr–Cr binary alloys processed by hot rolling*. Materials Science and Engineering: A, 2016. **652**: p. 77-83.
68. Ali, K., et al., *A first principles study of cohesive, elastic and electronic properties of binary Fe–Zr intermetallics*. Computational Materials Science, 2016. **112**: p. 52-66.
69. Proff, C., S. Abolhassani, and C. Lemaignan, *Oxidation behaviour of binary zirconium alloys containing intermetallic precipitates*. Journal of Nuclear Materials, 2011. **416**(1–2): p. 125-134.
70. Chemelle, P., et al., *Morphology and composition of second phase particles in zircaloy-2*. Journal of Nuclear Materials, 1983. **113**(1): p. 58-64.
71. Meng, X. and D.O. Northwood, *Second phase particles in Zircaloy-2*. Journal of Nuclear Materials, 1989. **168**(1): p. 125-136.
72. Degueldre, C., et al., *Zircaloy-2 secondary phase precipitate analysis by X-ray microspectroscopy*. Talanta, 2008. **75**(2): p. 402-406.
73. Gros, J.P. and J.F. Wadier, *Precipitate growth kinetics in Zircaloy-4*. Journal of Nuclear Materials, 1990. **172**(1): p. 85-96.
74. Pêcheur, D., et al., *Precipitate evolution in the Zircaloy-4 oxide layer*. Journal of Nuclear Materials, 1992. **189**(3): p. 318-332.
75. Hatano, Y., et al., *Influence of size distribution of Zr(Fe, Cr)₂ precipitates on hydrogen transport through oxide film of Zircaloy-4*. Journal of Nuclear Materials, 1997. **248**(0): p. 311-314.
76. Toffolon-Masclat, C., J.-C. Brachet, and G. Jago, *Studies of second phase particles in different zirconium alloys using extractive carbon replica and an electrolytic anodic dissolution procedure*. Journal of Nuclear Materials, 2002. **305**(2–3): p. 224-231.
77. de Gabory, B., A.T. Motta, and K. Wang, *Transmission electron microscopy characterization of Zircaloy-4 and ZIRLO™ oxide layers*. Journal of Nuclear Materials, 2015. **456**: p. 272-280.
78. Toffolon-Masclat, C., T. Guilbert, and J.C. Brachet, *Study of secondary intermetallic phase precipitation/dissolution in Zr alloys by high temperature–high sensitivity calorimetry*. Journal of Nuclear Materials, 2008. **372**(2): p. 367-378.
79. Fuloria, D., et al., *Tensile properties and microstructural evolution of Zircaloy-4 processed through rolling at different temperatures*. Materials & Design, 2016. **103**: p. 40-51.
80. F. Garzarolli, H.S., *Behaviour of structural materials for fuel and control elements in light water cooled power reactors*. Proc. IAEA Int, Symp. on Improvements in Water Reactor Technology and Utilization, 1986.
81. Pêcheur, D., *Oxidation of β -Nb and Zr(Fe, V)₂ precipitates in oxide films formed on advanced Zr-based alloys*. Journal of Nuclear Materials, 2000. **278**(2–3): p. 195-201.
82. Charquet, D., *Influence of precipitates on the corrosion of Zircaloy-4 in 400°C steam*. Journal of Nuclear Materials, 1994. **211**(3): p. 259-261.
83. Overwijk, M.H.F., F.C.v.d. Heuvel, and C.W.T. Bulle-Lieuwma, *Novel scheme for the preparation of transmission electron microscopy specimens with a focused ion beam*. Journal of Vacuum Science & Technology B: Microelectronics and Nanometer Structures Processing, Measurement, and Phenomena, 1993. **11**(6): p. 2021-2024.
84. Sawarn, T.K., et al., *Study of oxide and α -Zr(O) growth kinetics from high temperature steam oxidation of Zircaloy-4 cladding*. Journal of Nuclear Materials, 2015. **467**, Part 2: p. 820-831.
85. Couvant, T., *Corrosion in pressurized water reactors (PWRs)*, in *Materials Ageing and Degradation in Light Water Reactors*, K.L. Murty, Editor. 2013, Woodhead Publishing. p. 70-80.

86. Le Calvar, M. and I. De Curières, *Corrosion issues in pressurized water reactor (PWR) systems*, in *Nuclear Corrosion Science and Engineering*, D. Féron, Editor. 2012, Woodhead Publishing. p. 473-547.
87. Abbe, E., *Beiträge zur Theorie des Mikroskops und der mikroskopischen Wahrnehmung*. 1873.
88. De Broglie, L., *Recherches sur la théorie des Quanta*. 1924, Migration - université en cours d'affectation.
89. Knoll, M. and E. Ruska, *Das Elektronenmikroskop*. Zeitschrift für Physik, 1932. **78**(5): p. 318-339.
90. Thomson, G.P. and A. Reid, *Diffraction of cathode rays by a thin film*. Nature, 1927. **119**(3007): p. 890.
91. Davisson, C. and L.H. Germer, *Diffraction of Electrons by a Crystal of Nickel*. Physical Review, 1927. **30**(6): p. 705-740.
92. Williams, D.B., Carter, C. B., *Transmission Electron Microscopy: a textbook for materials science*. 2009: Springer US. 760.
93. Egerton, R., *Electron Energy-Loss Spectroscopy in the Electron Microscope*. 2011: Springer.
94. Williams, D.B. and C.B. Carter, *Transmission Electron Microscopy: a textbook for materials science*. 2009: Springer US. 760.
95. Rutherford, E., *LXXIX. The scattering of α and β particles by matter and the structure of the atom*. The London, Edinburgh, and Dublin Philosophical Magazine and Journal of Science, 1911. **21**(125): p. 669-688.
96. Asadabad, M.A. and M.J. Eskandari, *Electron Diffraction, Modern Electron Microscopy in Physical and Life Sciences*, ed. D.M. Janecek. 2016.
97. Franz, G., *Low Pressure Plasmas and Microstructuring Technology*. 1 ed. 2009: Springer-Verlag Berlin Heidelberg. 732.
98. Egerton, R.F., *Oscillator-strength parameterization of inner-shell cross sections*. Ultramicroscopy, 1993. **50**(1): p. 13-28.
99. Thomas, P.J. and R.D. Twisten, *A Simple, Model Based Approach for Robust Quantification of EELS Spectra and Spectrum-Images*. Microscopy and Microanalysis, 2012. **18**(Supplement S2): p. 968-969.
100. Shuman, H. and A.P. Somlyo, *Electron energy loss analysis of near-trace-element concentrations of calcium*. Ultramicroscopy, 1987. **21**(1): p. 23-32.
101. Leapman, R.D. and C.R. Swyt, *Separation of overlapping core edges in electron energy loss spectra by multiple-least-squares fitting*. Ultramicroscopy, 1988. **26**(4): p. 393-403.
102. Manoubi, T., et al., *Curve fitting methods for quantitative analysis in electron energy loss spectroscopy*. Microsc. Microanal. Microstruct., 1990. **1**(1): p. 23-39.
103. Verbeeck, J. and S. Van Aert, *Model based quantification of EELS spectra*. Ultramicroscopy, 2004. **101**(2-4): p. 207-224.
104. Verbeeck, J., S. Van Aert, and G. Bertonni, *Model-based quantification of EELS spectra: Including the fine structure*. Ultramicroscopy, 2006. **106**(11-12): p. 976-980.
105. Bertonni, G. and J. Verbeeck, *Accuracy and precision in model based EELS quantification*. Ultramicroscopy, 2008. **108**(8): p. 782-790.
106. Roberts, P.T.E., J.N. Chapman, and A.M. MacLeod, *A CCD-based image recording system for the CTEM*. Ultramicroscopy, 1982. **8**(4): p. 385-396.
107. Spence, J.C.H. and J.M. Zuo, *Large dynamic range, parallel detection system for electron diffraction and imaging*. Review of Scientific Instruments, 1988. **59**(9): p. 2102-2105.
108. Chapman, J.N., A.J. Craven, and C.P. Scott, *Electron detection in the analytical electron microscope*. Ultramicroscopy, 1989. **28**(1-4): p. 108-117.
109. Krivanek, O.L. and P.E. Mooney, *Applications of slow-scan CCD cameras in transmission electron microscopy*. Ultramicroscopy, 1993. **49**(1): p. 95-108.
110. Haider, M., et al., *Electron microscopy image enhanced*. Nature, 1998. **392**(6678): p. 768-769.

111. Haider, M., G. Braunschauen, and E. Schwan, *Correction of the spherical aberration of a 200 kV TEM by means of a hexapole-corrector*. *Optik*, 1995. **99**(4): p. 167-179.
112. Ahn, C. and O. Krivanek, *EELS Atlas Gatan Inc*. Warrendale, PA, 1983.
113. Jeanguillaume, C. and C. Colliex, *Spectrum-image: The next step in EELS digital acquisition and processing*. *Ultramicroscopy*, 1989. **28**(1-4): p. 252-257.
114. Scott, J., et al., *Near-simultaneous dual energy range EELS spectrum imaging*. *Ultramicroscopy*, 2008. **108**(12): p. 1586-1594.
115. Gubbens, A., et al., *The GIF Quantum, a next generation post-column imaging energy filter*. *Ultramicroscopy*, 2010. **110**(8): p. 962-970.
116. Bobynko, J., MacLaren, I., Craven, A. J., *Spectrum imaging of complex nanostructures using DualEELS: I. digital extraction replicas*. *Ultramicroscopy*, 2015. **149**(0): p. 9-20.
117. Lucas, G., et al., *Multivariate statistical analysis as a tool for the segmentation of 3D spectral data*. *Micron*, 2013. **52-53**(0): p. 49-56.
118. Bosman, M., et al., *Mapping chemical and bonding information using multivariate analysis of electron energy-loss spectrum images*. *Ultramicroscopy*, 2006. **106**(11-12): p. 1024-1032.
119. Brydson, R., *Electron energy loss spectroscopy*. 2001.
120. Verbeeck, J., Van Aert, S., *Model based quantification of EELS spectra*. *Ultramicroscopy*, 2004. **101**(2-4): p. 207-224.
121. Verbeeck, J., Van Aert, S., Bertoni, G., *Model-based quantification of EELS spectra: Including the fine structure*. *Ultramicroscopy*, 2006. **106**(11-12): p. 976-980.
122. Thomas, P. and R. Twisten, *A Simple, Model Based Approach for Robust Quantification of EELS Spectra and Spectrum-Images*. Vol. 18. 2012. 968-969.
123. Leapman, R.D., P. Rez, and D.F. Mayers, *K, L, and M shell generalized oscillator strengths and ionization cross sections for fast electron collisions*. *The Journal of Chemical Physics*, 1980. **72**(2): p. 1232-1243.
124. Egerton, R.F., *Values of K-shell partial cross-section for electron energy-loss spectrometry*. *Journal of Microscopy*, 1981. **123**(3): p. 333-337.
125. Pearson, D.H., C.C. Ahn, and B. Fultz, *White lines and d-electron occupancies for the 3d and 4d transition metals*. *Physical Review B*, 1993. **47**(14): p. 8471-8478.
126. Leapman, R.D., L.A. Grunes, and P.L. Fejes, *Study of the L_{23} edges in the 3d transition metals and their oxides by electron-energy-loss spectroscopy with comparisons to theory*. *Physical Review B*, 1982. **26**(2): p. 614-635.
127. Barth, J., F. Gerken, and C. Kunz, *Atomic nature of the L_{23} white lines in Ca, Sc, and Ti metals as revealed by resonant photoemission*. *Physical Review B*, 1983. **28**(6): p. 3608-3611.
128. Ni, N., Lozano-Perez, S., Sykes, J., Grovenor, C., *Quantitative EELS analysis of zirconium alloy metal/oxide interfaces*. *Ultramicroscopy*, 2011. **111**(2): p. 123-130.
129. Scott, J., Thomas, P. J., MacKenzie, M., McFadzean, S., Wilbrink, J., Craven, A. J., Nicholson, W. A. P., *Near-simultaneous dual energy range EELS spectrum imaging*. *Ultramicroscopy*, 2008. **108**(12): p. 1586-1594.
130. Leapman, R.D., Swyt, C. R., *Separation of overlapping core edges in electron energy loss spectra by multiple-least-squares fitting*. *Ultramicroscopy*, 1988. **26**(4): p. 393-403.
131. Manoubi, T., Tencé, M., Walls, M. G., Colliex, C., *Curve fitting methods for quantitative analysis in electron energy loss spectroscopy*. *Microsc. Microanal. Microstruct.*, 1990. **1**(1): p. 23-39.
132. Bertoni, G., Verbeeck, J., *Accuracy and precision in model based EELS quantification*. *Ultramicroscopy*, 2008. **108**(8): p. 782-790.
133. Frandon, J., Brousseau, B., Pradal, F., *Electronic Excitations in Some Transition Metals and Their Oxides. Characteristic Energy Loss Measurements up to 50 eV*. *physica status solidi (b)*, 1980. **98**(1): p. 379-385.
134. Axelsson, K.O., K.E. Keck, and B. Kasemo, *AES and EEL spectra from Zr, Zr + O₂ and ZrO₂; peak energy shifts and intensity variations at various stages of oxidation in the pressure range 10-6-103 Torr*. *Surface Science*, 1985. **164**(1): p. 109-126.

135. Prieto, P., Yubero, F., Elizalde, E., Sanz, J. M., *Dielectric properties of Zr, ZrN, Zr₃N₄, and ZrO₂ determined by quantitative analysis of electron energy loss spectra*. Journal of Vacuum Science, 1996. **14**(6): p. 3181-3188.
136. Keast, V.J., et al., *Electron energy-loss near-edge structure – a tool for the investigation of electronic structure on the nanometre scale*. Journal of Microscopy, 2001. **203**(2): p. 135-175.
137. Ostanin, S., Craven, A. J., McComb, D. W., Vlachos, D., Alavi, A., Finnis, M. W., Paxton, A., *Effect of relaxation on the oxygen K-edge electron energy-loss near-edge structure in yttria-stabilized zirconia*. Physical Review B, 2000. **62**(22): p. 14728-14735.
138. Shigeo, A., Shunsuke, M., Junya, M., Tsuyoshi, S., Yoshio, U., Kotaro, K., Hiroyasu, S., *Valence Change of Cations in Ceria-Zirconia Solid Solution Associated with Redox Reactions Studied with Electron Energy-Loss Spectroscopy*. Materials Transactions, 2004. **45**(10): p. 2951-2955.
139. Aguiar, J.A., Ramasse, Q. M., Asta, M., Browning, N. D., *Investigating the electronic structure of fluorite-structured oxide compounds: comparison of experimental EELS with first principles calculations*. Journal of Physics: Condensed Matter, 2012. **24**(29): p. 295503.
140. Wang, Z.L., Yin, J. S., Jiang, Y. D., Zhang, J., *Studies of Mn valence conversion and oxygen vacancies in La_{1-x}CaxMnO_{3-y} using electron energy-loss spectroscopy*. Applied Physics Letters, 1997. **70**(25): p. 3362-3364.
141. Van Aken, P.A., Liebscher, B., Styrsa, V. J., *Quantitative determination of iron oxidation states in minerals using Fe L_{2,3} -edge electron energy-loss near-edge structure spectroscopy*. Physics and Chemistry of Minerals, 1998. **25**(5): p. 323-327.
142. Garvie, L.A.J. and P.R. Buseck, *Ratios of ferrous to ferric iron from nanometre-sized areas in minerals*. Nature, 1998. **396**(6712): p. 667-670.
143. Wang, Z.L., Yin, J. S., Jiang, Y. D., *EELS analysis of cation valence states and oxygen vacancies in magnetic oxides*. Micron, 2000. **31**(5): p. 571-580.
144. Wang, Y.Q., Maclaren, I., Duan, X. F., *EELS analysis of manganese valence states in rare-earth manganites (La_{1-x}Yx)_{0.5}(Ca_{1-y}Sry)_{0.5}MnO₃*. Materials Science and Engineering: A, 2001. **318**(1-2): p. 259-263.
145. Gubbens, A., Barfels, M., Trevor, C., Twesten, R., Mooney, P., Thomas, P., Menon, N., Kraus, B., Mao, C., McGinn, B., *The GIF Quantum, a next generation post-column imaging energy filter*. Ultramicroscopy, 2010. **110**(8): p. 962-970.
146. Cliff, G. and G.W. Lorimer, *The quantitative analysis of thin specimens*. Journal of Microscopy, 1975. **103**(2): p. 203-207.
147. Hofer, F., *EELS quantification of M edges by using oxidic standards*. Ultramicroscopy, 1987. **21**(1): p. 63-68.
148. Crozier, P.A., et al., *On the determination of inner-shell cross-section ratios from NiO using EELS*. Journal of Microscopy, 1987. **148**(3): p. 279-284.
149. Saillard, A., Cherkaoui, M., El Kadiri, H., *Stress-induced roughness development during oxide scale growth on a metallic alloy for SOFC interconnects*. Modelling and Simulation in Materials Science and Engineering, 2011. **19**(1): p. 015009.
150. Yardley, S.S., Moore, K. L., Ni, N., Wei, J. F., Lyon, S., Preuss, M., Lozano-Perez, S., Grovenor, C. R. M., *An investigation of the oxidation behaviour of zirconium alloys using isotopic tracers and high resolution SIMS*. Journal of Nuclear Materials, 2013. **443**(1-3): p. 436-443.
151. Polatidis, E., Frankel, P., Wei, J., Klaus, M., Comstock, R. J., Ambard, A., Lyon, S., Cottis, R. A., Preuss, M., *Residual stresses and tetragonal phase fraction characterisation of corrosion tested Zircaloy-4 using energy dispersive synchrotron X-ray diffraction*. Journal of Nuclear Materials, 2013. **432**(1-3): p. 102-112.
152. Beranger, G. and P. Lacombe, *Contribution a l'etude de la cinetique de l'oxydation du zirconium α et de la diffusion de l'oxygene dans le metal sous-jacent a l'oxyde*. Journal of Nuclear Materials, 1965. **16**(2): p. 190-207.
153. McVitie, S., et al., *Aberration corrected Lorentz scanning transmission electron microscopy*. Ultramicroscopy, 2015. **152**: p. 57-62.
154. Navío, J.A., et al., *Preparation and Physicochemical Properties of ZrO₂ and Fe/ZrO₂ Prepared by a Sol-Gel Technique*. Langmuir, 2001. **17**(1): p. 202-210.

155. Chen, L., J. Hu, and R.M. Richards, *Catalytic Properties of Nanoscale Iron-Doped Zirconia Solid-Solution Aerogels*. ChemPhysChem, 2008. **9**(7): p. 1069-1078.
156. Wang, Z.L., *Valence electron excitations and plasmon oscillations in thin films, surfaces, interfaces and small particles*. Micron, 1996. **27**(3): p. 265-299.
157. Götlind, H., et al., *The Effect of Water Vapor on the Initial Stages of Oxidation of the FeCrAl Alloy Kanthal AF at 900 °C*. Oxidation of Metals, 2007. **67**(5): p. 251-266.
158. Airiskallio, E., et al., *High temperature oxidation of Fe–Al and Fe–Cr–Al alloys: The role of Cr as a chemically active element*. Corrosion Science, 2010. **52**(10): p. 3394-3404.
159. Muan, A. and S. Somiya, *Phase Equilibria in the System Iron Oxide—Cr₂O₃– SiO₂ in Air*. Journal of the American Ceramic Society, 1960. **43**(10): p. 531-541.
160. B. de Gabory, A.T.M., *Structure of Zircaloy 4 Oxides Formed during Autoclave Corrosion*, in *ANS LWR Fuel Performance Meeting, TopFuel 2013*. September 2013: Charlotte, NC.
161. Bedworth, R. and N. Pilling, *The oxidation of metals at high temperatures*. J Inst Met, 1923. **29**(3): p. 529-582.
162. Arima, T., et al., *Oxidation properties of Zr–Nb alloys at 500–600°C under low oxygen potentials*. Corrosion Science, 2005. **47**(2): p. 435-446.
163. Zhu, Z.J., et al., *Corrosion-related defects in Zircalloys: a preliminary study with slow positron beam*. Journal of Physics: Conference Series, 2014. **505**(1): p. 012008.
164. Wei, J., et al., *Autoclave study of zirconium alloys with and without hydride rim*. Corrosion Engineering, Science and Technology, 2012. **47**(7): p. 516-528.
165. Roy, C. and B. Burgess, *A study of the stresses generated in zirconia films during the oxidation of zirconium alloys*. Oxidation of Metals, 1970. **2**(3): p. 235-261.
166. Proff, C., S. Abolhassani, and C. Lemaignan, *Oxidation behaviour of zirconium alloys and their precipitates – A mechanistic study*. Journal of Nuclear Materials, 2013. **432**(1): p. 222-238.
167. Pemsler, J.P., *Diffusion of Oxygen in Zirconium and Its Relation to Oxidation and Corrosion*. Journal of The Electrochemical Society, 1958. **105**(6): p. 315-322.
168. Gertsman, V.Y., A.P. Zhilyaev, and J.A. Szpunar, *Grain boundary misorientation distributions in monoclinic zirconia*. Modelling and Simulation in Materials Science and Engineering, 1997. **5**(1): p. 35.
169. Hill, R.J. and L.M.D. Cranswick, *International-union-of-crystallography - commission-on-powder-diffraction - rietveld refinement round-robin .2. Analysis of monoclinic zro2*. Journal of Applied Crystallography, 1994. **27**: p. 802-844.
170. Goldak, J., L.T. Lloyd, and C.S. Barrett, *Lattice Parameters, Thermal Expansions, and Gruneisen Coefficients of Zirconium, 4.2 to 1130*. Physical Review, 1966. **144**(2): p. 478-484.
171. Maslen, *Acta Crystallographica*, 1994. **Section B: Structural Science**(50): p. 435-441.
172. Malakhova, T.O. and Z.M. Alekseyeva, *The Zr-Fe phase diagram in the range 20–40 at.% Fe and the crystalline structure of the intermetallic compound Zr₃Fe*. Journal of the Less Common Metals, 1981. **81**(2): p. 293-300.
173. Belokoneva, E.L., *Zhurnal Neorganicheskoi Khimii*, 2003. **48**: p. 960-968.
174. Straumanis, M.E. and D.C. Kim, *Zeitschrift fuer Metallkunde*, 1969. **60**: p. 272-277.
175. de Boer, J.H. and J.D. Fast, *Electrolysis of solid solutions of oxygen in metallic zirconium*. Recueil des Travaux Chimiques des Pays-Bas, 1940. **59**(2): p. 161-167.
176. Holmberg, B. and T. Dagerhamn, *X-ray studies on solid solutions of oxygen in α -zirconium*. Acta Chem. Scand, 1961. **15**(4): p. 14.
177. Domagala, R. and D. McPherson, *System zirconium-oxygen*. Trans. AIME, 1954. **200**(2): p. 238-246.
178. Rudling, P. and G. Wikmark, *A unified model of Zircaloy BWR corrosion and hydriding mechanisms*. Journal of Nuclear Materials, 1999. **265**(1): p. 44-59.
179. Lucas, G., Burdet, P., Cantoni, M., Hébert, C., *Multivariate statistical analysis as a tool for the segmentation of 3D spectral data*. Micron, 2013. **52–53**(0): p. 49-56.
180. Annand, K.J., I. MacLaren, and M. Gass, *Utilising DualEELS to probe the nanoscale mechanisms of the corrosion of Zircaloy-4 in 350 °C pressurised water*. Journal of Nuclear Materials, 2015. **465**: p. 390-399.

181. Garner, A., et al., *The effect of Sn concentration on oxide texture and microstructure formation in zirconium alloys*. *Acta Materialia*, 2015. **99**: p. 259-272.
182. Hu, J., et al., *High-resolution characterization of corrosion and hydrogen pickup of zr cladding alloys*.
183. Guerain, M., M. Mermoux, and C. Duriez, *The use of micro-Raman imaging to measure 18O tracer distribution in thermally grown zirconia scales*. *Corrosion Science*, 2015. **98**: p. 140-149.
184. Maclaren, I., et al., *EELS at very high energy losses*. *Microscopy and Microanalysis*, 2017.